Title
The Dynamics Of Layered And Non-Layered Oscillatory Double-Diffusive Convection

Author
Moll, Ryan

Publication Date
2016

UNIVERSITY OF CALIFORNIA
SANTA CRUZ

THE DYNAMICS OF LAYERED AND NON-LAYERED OSCILLATORY DOUBLE-DIFFUSIVE CONVECTION

A dissertation submitted in partial satisfaction of the
requirements for the degree of

DOCTOR OF PHILOSOPHY

in

APPLIED MATHEMATICS AND STATISTICS

by

Ryan D. Moll

September 2016

The Dissertation of Ryan D. Moll
is approved:

Professor Pascale Garaud, Chair

Professor Nicholas Brummell

Professor Jonathan Fortney

Tyrus Miller
Vice Provost and Dean of Graduate Studies

Table of Contents

List of Figures

List of Tables

Abstract

The dynamics of layered and non-layered oscillatory double-diffusive convection

by

Ryan D. Moll

Oscillatory double diffusive convection (ODDC) is a double diffusive instability that occurs in fluids that are unstably stratified in temperature and stably stratified in chemical composition. Regions unstable to ODDC are common in the interiors of stars and giant planets, and knowing thermal and compositional transport through these regions is important for stellar and planetary evolution models. Using 3D direct numerical simulations, Rosenblum et al. (2011) first showed that ODDC can either lead to the spontaneous formation of convective layers, or remain in a state dominated by large scale gravity waves. Subsequent studies focused on identifying the conditions for layer formation (Mirouh et al., 2012), and quantifying transport through layered systems (Wood et al., 2013). This document includes 3 works that build on the results of these earlier studies. The subject of the first is transport through non-layered ODDC and shows that in the absence of layered convection, ODDC is dominated by large scale gravity waves that grow to the size of the domain. We find that while these gravity waves induce small amounts of turbulent mixing, turbulent transport through non-layered systems is not significant for the purposes of astrophysical modeling (unlike in layered convection). The second study pertains to ODDC in the presence of Coriolis forces, and shows that rotating systems can be categorized depending on the strength of the rotation. We find that in the slowly rotating regime, the presence of rotation does not significantly affect qualitative behavior, but leads to modest reductions in thermal and compositional transport, while in the fast rotation regime qualitative behaviors are radically different, and systems are dominated by vortices that affect thermal and compositional transport in complex ways. In the final work we study simulations of ODDC at non-layered parameters that are forced into a layered configuration by initial conditions. Our results show that measurements of thermal and compositional transport deviate from values predicted by oft-cited geophysical transport laws.

This work is dedicated to all those who have loved and supported me over these years. Thanks to my friends Chris, Logan, Sam, Megan, Sam, Devon, Max, Steve, Jared and Lynna. Special thanks to my parents, Mary Jo and Doug, my brother, Tommy, and my girlfriend, Maggie. I couldn't have done it without you! This is also dedicated to the memory of my grandfather, Loren Moll. He would be proud to know that there is a new Dr. Moll in the family.

Acknowledgments

I would like to thank all those who have helped me complete my graduate studies and mentored me along the way. Thanks to Stephan Stellmach from Westfälishe Wilhelms-Universität at Münster and Erik Vold from Los Alamos National Laboratory for serving as excellent mentors and generously agreeing to write letters of reference for me. I would like to thank Professor Gary Glatzmaier for serving on my advancement committee and Professor Jonathan Fortney for serving on both my advancement and defense committees. I would like to thank both of them for teaching great classes in their respective disciplines, as well. Thanks to Professor Nic Brummell for serving on my advancement and defense committees, for writing letters of reference, and for being a great teacher of all things applied math and fluid dynamics. I would especially like to thank my advisor, Professor Pascale Garaud, who has been more supportive and conscientious than I could have hoped. She has been very patient with me, and has taught me so much. No one works harder for their students than she does.

Chapter 1

Introduction

1.1 Background

Double diffusive convection is a general term used to refer to turbulent motions that occur in fluids which are stratified in two quantities that affect density and diffuse at different rates. Furthermore, a double diffusive fluid must be unstably stratified in one of the density components, and stably stratified in the other such that the fluid is stable to regular overturning convection (but crucially, not absolutely stable to all instabilities). In geophysical and astrophysical fluids the diffusive quantities are usually temperature and chemical composition, where temperature is the component which diffuses faster.

The primary focus of this work is double diffusive convection in astrophysical fluids which have stabilizing compositional gradients (Ledoux stable) and a destabilizing thermal gradients (Schwarzschild unstable). Double diffusive convection of this kind (often referred to as “the diffusive regime" or “semi-convection") is common in a variety of astrophysical objects and was first discussed in the astrophysical context by Schwarzschild & Härm (1958) with regard to the growing convection zones of massive stars ($> 10M_{\odot}$).

They postulated the existence of a layer separating the helium-enriched, convective core of a massive star from the radiative hydrogen envelope, where there exists a destabilizing thermal gradient and a composition gradient just steep enough to prevent the region from being unstable to overturning convection. Schwarzschild & Härm (1958) referred to this zone as being “semi-convective" due to the fact that the region would be unstable to convection in the absence of the stabilizing composition gradient. However, it was still believed to be linearly stable.

It was Walin (1964) and Kato (1966) who realized that despite being stable to overturning convection such an environment could be subject to another linear instability capable of driving the turbulent transport of heat and chemical species. This type of linear instability is now commonly referred to as oscillatory double-diffusive convection (ODDC) (Spiegel, 1969) due to the resemblance the basic unstable fluid motions bear to over-stable internal gravity waves (Kato, 1966). Because of the pervasiveness of double diffusive regions in the interiors of astrophysical objects, the efficiency of thermal and compositional mixing resulting from ODDC is potentially significant to evolution models for stars (Langer et al., 1985; Merryfield, 1995) and giant planets (Stevenson, 1982; Leconte & Chabrier, 2012; Nettelmann et al., 2015).

To understand the qualitative behavior of this linear instability recall that the fast-diffusing quantity (temperature) has an unstable stratification and the slow-diffusing quantity (chemical composition) has a stable stratification. To describe the basic motions of ODDC, it is helpful first consider a system like the one depicted in Figure 1.1a, which only has a stabilizing compositional gradient. In such a system a fluid element perturbed up or down oscillates vertically about its original position at the Brunt-Väisälä frequency. Over short timescales the amplitude of this oscillation will remain fairly constant and over longer timescales the amplitude will decay due to the effects of viscosity or diffusion.

When a destabilizing temperature gradient is added, as in Figure 1.1b, a fluid parcel perturbed, say, upward will quickly looses heat to its surroundings, but its chemical composition remains nearly unchanged due to the difference in diffusivities (Kato, 1966). The fluid parcel will then be denser than its surroundings, and it will sink. When it returns to its original position, though, it will not have fully thermally equilibrated to its surroundings, and will still be denser than it was originally. As a result the parcel will continue to sink, and will, in fact, sink a greater distance below its original position than it was originally perturbed upward. The parcel continues to oscillate in this fashion with an amplitude which grows exponentially until the instability reaches non-linear saturation.

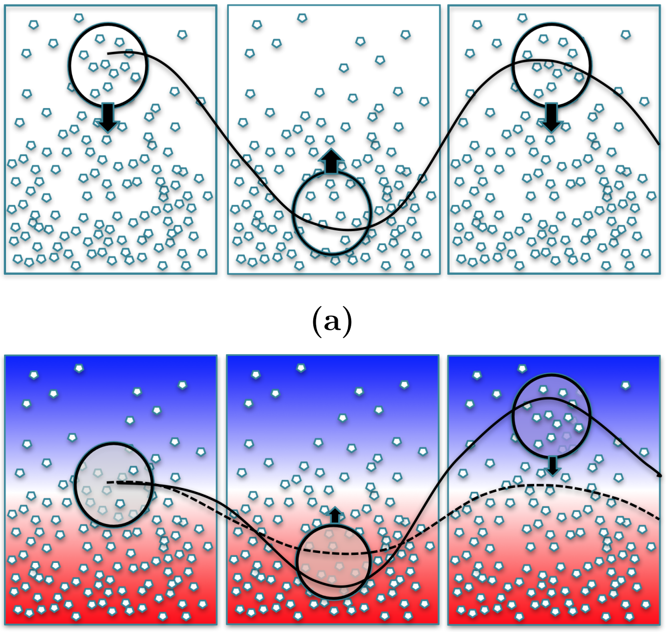

(a)

(b)

Figure 1.1: (a) Sketch depicting a fluid which has only a stable compositional gradient and (b) a fluid which has a stable compositional gradient and an unstable temperature gradient.

1.2 Mathematical model

In order to model ODDC mathematically, it is useful to consider a region that is significantly smaller than the density scale height of a typical star or planet, and where flow speeds are much smaller than the sound speed of the medium. This allows for the use the Boussinesq approximation (Spiegel & Veronis, 1960) and to ignore the spherical geometry of an actual stellar or planetary interior. For simplicity, the domain is assumed to be a Cartesian box where z is oriented in the radial direction. Furthermore, background gradients of temperature, T_{0z}, and mean molecular weight, μ_{0z}, are assumed to be constant in the domain. We use the following linearized equation of state,

$$\frac{\tilde{\rho}}{\rho_0} = -\alpha\tilde{T} + \beta\tilde{\mu}\,, \tag{1.1}$$

where $\tilde{\rho}$, $\tilde{T}$ and $\tilde{\mu}$ are dimensional perturbations to the background profiles of density, temperature and chemical composition, respectively, and where ρ_0 is the mean density of the region. The parameters α and β are the coefficient of thermal expansion and coefficient of compositional contraction, respectively, and are defined as

$$\begin{aligned} \alpha &= -\frac{1}{\rho_0}\frac{\partial\rho}{\partial T}\bigg|_{p,\mu}\,, \\ \beta &= \frac{1}{\rho_0}\frac{\partial\rho}{\partial\mu}\bigg|_{p,T}\,. \end{aligned} \tag{1.2}$$

Under these assumptions, the governing equations for ODDC are given by

$$\begin{aligned}
\nabla \cdot \tilde{\mathbf{u}} &= 0\,, \\
\frac{\partial \mathbf{u}}{\partial t} + \mathbf{u} \cdot \nabla \mathbf{u} &= -\frac{1}{\rho_0} \nabla p + \left(\alpha \tilde{T} - \beta \tilde{\mu}\right) g \mathbf{e}_z + \nu \nabla^2 \mathbf{u}\,, \\
\frac{\partial T}{\partial t} + \mathbf{u} \cdot \nabla T &= \left| T_{0z} - T_{0z}^{\mathrm{ad}} \right| w + \kappa_T \nabla^2 T\,, \\
\frac{\partial \mu}{\partial t} + \mathbf{u} \cdot \nabla \mu &= \left| \mu_{0z} \right| w + \kappa_\mu \nabla^2 \mu\,,
\end{aligned} \tag{1.3}$$

where $\tilde{\mathbf{u}}$ is the velocity field, and where $\tilde{p}$ signifies perturbations to the background pressure profile. The constant parameters κ_T, κ_μ, ν and g are the thermal diffusivity, compositional diffusivity, viscosity and gravitational acceleration, respectively, and T_{0z}^{ad} is the background adiabatic temperature gradient which is defined as

$$T_{0z}^{\mathrm{ad}} = -\frac{g}{c_p}\,. \tag{1.4}$$

where c_p is the specific heat at constant pressure. These equations are non-dimensionalized using a unit length defined in terms of the dimensional constants in (1.3),

$$[l] = d = \left(\frac{\kappa_T \nu}{\alpha g |T_{0z} - T_{0z}^{\mathrm{ad}}|} \right)^{\frac{1}{4}}\,, \tag{1.5}$$

Using these constants, the units of time, $[t]$, temperature, $\left[\tilde{T}\right]$, and mean molecular weight, $[\tilde{\mu}]$, naturally emerge as

$$\begin{aligned}
[t] &= \frac{d^2}{\kappa_T}\,, \\
\left[\tilde{T}\right] &= d|T_{0z} - T_{0z}^{\mathrm{ad}}|\,, \\
[\tilde{\mu}] &= \frac{\alpha}{\beta} d|T_{0z} - T_{0z}^{\mathrm{ad}}|\,.
\end{aligned} \tag{1.6}$$

In these units, the standard non-dimensional governing equations for ODDC

(Rosenblum et al., 2011; Mirouh et al., 2012) are

$$
\begin{aligned}
\nabla \cdot \tilde{\mathbf{u}} &= 0\,, \\
\frac{1}{\mathrm{Pr}}\left(\frac{\partial \tilde{\mathbf{u}}}{\partial t} + \tilde{\mathbf{u}} \cdot \nabla \tilde{\mathbf{u}}\right) &= -\nabla \tilde{p} + (\tilde{T} - \tilde{\mu})\mathbf{e}_z + \nabla^2 \tilde{\mathbf{u}}\,, \\
\frac{\partial \tilde{T}}{\partial t} + \tilde{\mathbf{u}} \cdot \nabla \tilde{T} - \tilde{w} &= \nabla^2 \tilde{T}\,, \\
\frac{\partial \tilde{\mu}}{\partial t} + \tilde{\mathbf{u}} \cdot \nabla \tilde{\mu} - R_0^{-1} \tilde{w} &= \tau \nabla^2 \tilde{\mu}\,,
\end{aligned}
\tag{1.7}
$$

where the non-dimensional numbers Pr, τ and R_0^{-1} are the Prandtl number, diffusivity ratio, and inverse density ratio, respectively, defined as (Baines & Gill, 1969)

$$
\begin{aligned}
\mathrm{Pr} &= \frac{\nu}{\kappa_T}\,, \\
\tau &= \frac{\kappa_\mu}{\kappa_T}\,, \\
R_0^{-1} &= \frac{\beta |\mu_{0z}|}{\alpha |T_{0z} - T_{0z}^{\mathrm{ad}}|}\,.
\end{aligned}
\tag{1.8}
$$

These parameters describe the physical properties of the fluid and the relative strengths of the thermal and compositional stratifications and determine whether or not a fluid is unstable to ODDC

In an infinite domain, ODDC occurs when R_0^{-1} is within the following range (Kato, 1966; Walin, 1964),

$$
1 < R_0^{-1} < R_{\mathrm{c}}^{-1} \equiv \frac{\mathrm{Pr} + 1}{\mathrm{Pr} + \tau}\,. \tag{1.9}
$$

When R_0^{-1} is less than one, the system is unstable to overturning convection, and when R_0^{-1} is greater than R_c^{-1} the system is stable to infinitesimal perturbations (but may still be unstable to finite amplitude ones, as we will discuss in Chapter

4). A useful proxy for the inverse density ratio is the so-called “reduced inverse density ratio" parameter (Mirouh et al., 2012), defined as,

$$r = \frac{R_0^{-1} - 1}{R_c^{-1} - 1} \,. \tag{1.10}$$

This parameter maps the natural ODDC range to the interval $[0, 1]$ where 0 marks the onset of overturning convection, and 1 marks the boundary between the ODDC parameter space and that of linear stability.

1.3 Linear stability analysis

The governing equation of ODDC in (1.7) are non-linear, and therefore have no known analytical solution. However, properties of the linear instability, such as the rate of growth and spatial structure of the fastest growing modes, can be studied analytically by assuming that all perturbations are initially small and that non-linear terms are initially negligible. The first step in the linear stability analysis is to assume that all perturbations take the following functional form:

$$\begin{aligned} q &= \hat{q} e^{i\mathbf{k}\cdot\mathbf{x}+\lambda t} \,, \\ \mathbf{k} &= \{l, m, k\} \,, \\ \mathbf{x} &= \{x, y, z\} \end{aligned} \tag{1.11}$$

where $q = \{\mathbf{u}, p, T, \mu\}$, λ is the complex growth rate, and where l, m, and k are spatial wave numbers in the x, y, and z directions. By applying these definitions for the perturbations to the governing equations in (1.7) and by ignoring the non-linear terms ($\mathbf{u} \cdot \nabla \mathbf{u}$, $\mathbf{u} \cdot \nabla T$, and $\mathbf{u} \cdot \nabla \mu$) we get the following linearized equations:

$$
\begin{aligned}
ilu + imv + ikw &= 0\,, \\
\lambda\hat{u} &= il\hat{p} - \mathrm{Pr}|\mathbf{k}|^2\hat{u}\,, \\
\lambda\hat{v} &= im\hat{p} - \mathrm{Pr}|\mathbf{k}|^2\hat{v}\,, \\
\lambda\hat{w} &= ik\hat{p} - \mathrm{Pr}\left(\hat{T} - \hat{\mu}\right) - \mathrm{Pr}|\mathbf{k}|^2\hat{w}\,, \\
\lambda\hat{T} &= \hat{w} - |\mathbf{k}|^2\hat{T}\,, \\
\lambda\hat{\mu} &= R_0^{-1}\hat{w} - |\mathbf{k}|^2\hat{\mu}\,,
\end{aligned}
\tag{1.12}
$$

From these equations we compute dispersion relation which only involves λ, Pr, τ, R_0^{-1} and the wave numbers l, m, k,

$$\left(\lambda + \mathrm{Pr}|\mathbf{k}|^2\right)\left(\lambda + |\mathbf{k}|^2\right)\left(\lambda + \tau|\mathbf{k}|^2\right) - \mathrm{Pr}\left(\frac{|\mathbf{k_H}|^2}{|\mathbf{k}|^2}\right)\left[\left(\lambda + \tau|\mathbf{k}|^2\right) - R_0^{-1}\left(\lambda + |\mathbf{k}|^2\right)\right] = 0\,, \tag{1.13}$$

where $|\mathbf{k_H}|^2 = l^2 + m^2$. Figure 1.2 shows growth rates calculated from this equation as a function of vertical and horizontal wavenumber. The figure shows that the modes which grow the fastest have $k = 0$ meaning that they oscillate up and down only in the vertical direction. The horizontal wavenumber of the fastest growing modes depends on Pr, τ, and R_0^{-1}, but generally corresponds to features which have a horizontal scale of $10 - 20d$ (in Figure 1.2 $|\mathbf{k_H}|$ of the fastest growing mode is ≈ 0.36 corresponding to a horizontal scale of $\approx 17d$). Modes unstable to ODDC have $\mathrm{Re}(\lambda) > 0$ and $\mathrm{Im}(\lambda) \neq 0$, and exist if and only if $1 < R_0^{-1} < R_c^{-1}$. In this parameter regime, there are two complex conjugate roots and one real root that is always negative.

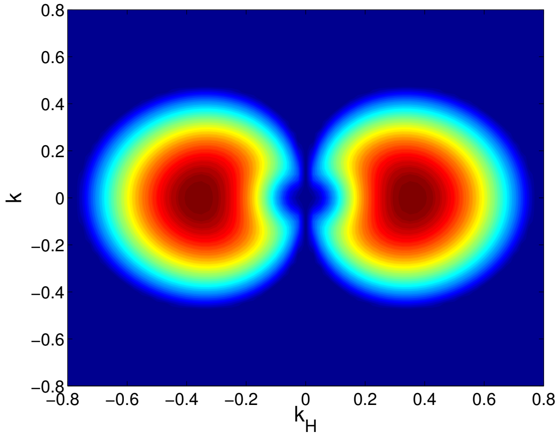

Figure 1.2: Contour plot showing growth rates of linearly unstable modes as a function of the horizontal and vertical wave numbers. The dark red areas indicate modes with the largest growth rates.

1.3.1 Numerical simulations and measured quantities

The long term behavior of fluids unstable to ODDC is of particular interest in astrophysics. Because physical characteristics of stellar and planetary interiors cannot be easily reproduced in laboratory experiments, numerical simulations are needed to gain insight about the nonlinear behavior of ODDC in these objects. All results that follow were generated by solving the equations in (1.7) using a pseudo-spectral code called PADDI (Traxler et al., 2011), where all perturbations are triply periodic in the domain. Some of the experimental data presented in subsequent chapters was generated by Rosenblum et al. (2011), Mirouh et al. (2012), and Wood et al. (2013) in simulations run using this code. All simulations are initialized with random small perturbations to the temperature and/or chemical composition fields.

The main quantities of interest extracted from these numerical simulations are the turbulent vertical fluxes of temperature and chemical species, $\langle \tilde{w}\tilde{T} \rangle$ and $\langle \tilde{w}\tilde{\mu} \rangle$, respectively, where the angle brackets represent a spatial integral over the entire computational domain. It is often useful to express these fluxes in terms of thermal and compositional Nusselt numbers ($\mathrm{Nu_T}$ and Nu_μ) which are the ratios of the total fluxes to the diffusive fluxes (of temperature and composition). The turbulent fluxes are defined as follows in terms of $\mathrm{Nu_T}$ and Nu_μ,

$$\begin{aligned} F_T^{\mathrm{turb}} &= \langle \tilde{w}\tilde{T} \rangle = \mathrm{Nu}_T - 1\,, \\ F_\mu^{\mathrm{turb}} &= \langle \tilde{w}\tilde{\mu} \rangle = \tau R_0^{-1} \left(\mathrm{Nu}_\mu - 1\right)\,. \end{aligned} \tag{1.14}$$

As shown by Wood et al. (2013), these fluxes often exhibit fast oscillations with large amplitudes due to the gravity waves, so for the purposes of analysis, it can be more useful to consider related quantities known as the thermal and compositional dissipations, $\langle |\nabla \tilde{T}|^2 \rangle$ and $\langle |\nabla \tilde{\mu}|^2 \rangle$. Indeed, as shown by Malkus (1954), taking a spatial integral of the thermal and chemical evolution equations, and then assuming that the system is in a statistically stationary state, we find that the dissipations are related to the turbulent fluxes and Nusselt numbers by

$$\begin{aligned} \overline{\mathrm{Nu}_T} - 1 = \overline{\langle \tilde{w}\tilde{T} \rangle} &= \overline{\langle |\nabla \tilde{T}|^2 \rangle}\,, \\ \overline{\mathrm{Nu}_\mu} - 1 = \frac{\overline{\langle \tilde{w}\tilde{\mu} \rangle}}{\tau R_0^{-1}} &= \frac{\overline{\langle |\nabla \tilde{\mu}|^2 \rangle}}{\left(R_0^{-1}\right)^2}\,, \end{aligned} \tag{1.15}$$

where the bars indicate temporal averages over the entire statistically stationary period. In practice, these are good approximations even when the temporal averaging is done over relatively short periods (see Wood et al. (2013) for instance), so in what follows we assume similar relations between the instantaneous Nusselt numbers and dissipations as well. This is advantageous because the dissipations are less sensitive to the oscillations of gravity waves than the fluxes, and are therefore easier to analyze.

1.3.2 Previous studies

A number of recent studies have been dedicated to describing long term behavior of ODDC through the use of direct numerical simulations of the kind described above. In a preliminary study, Rosenblum et al. (2011) first identified two general classes of behavior that occur in ODDC after the saturation of the linear instability: spontaneous layer formation and non-layered “homogeneous turbulence".

They put the greatest emphasis on explaining the phenomenon of layer formation. At smaller values of R_0^{-1}, they observed the spontaneous formation of density staircases composed of convective layers of uniform density separated by dynamic, but convectively stable interfaces. These layers emerge from the homogeneously mixed environment that exists immediately following the saturation of the linear instability, and then merge progressively until a single layer interface remains in the domain (regardless of how many layers initially form). Importantly, as illustrated by the top row of Figure 1.3, they found that the formation and mergers of layers were associated with stepwise increases in the turbulent flux of temperature and chemical composition. The final, single-interface state, shows turbulent fluxes that are smaller than fluxes from overturning convection but still orders of magnitude larger than molecular diffusion. Rosenblum et al. (2011) proposed that layers form through a mechanism known as the γ-instability (Radko, 2003).

Radko (2003) first proposed the γ-instability to describe layer formation in fingering convection. The theory describes the growth of large-scale, horizontally invariant perturbations to the background density profile. These perturbations create regions of the domain where the density gradient is locally unstable to overturning convection, leading to a configuration of stacked convective layers.

The theory is derived by taking spatial and temporal averages of the governing

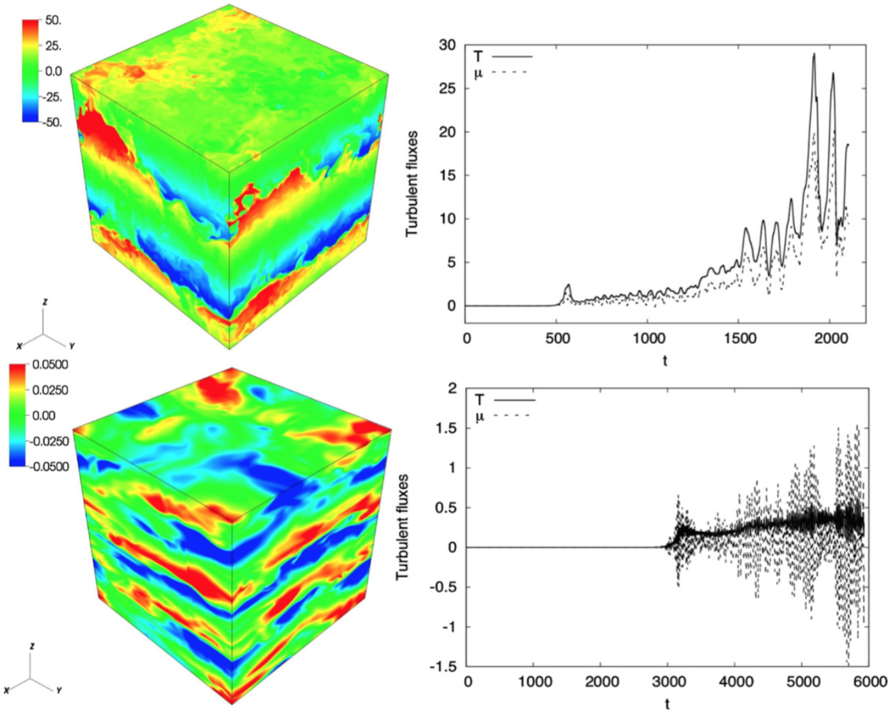

Figure 1.3: Figure 2 from Mirouh et al. (2012). The top row shows a snapshot of the chemical field and a time series of the thermal and compositional fluxes for a layered simulation with $\mathrm{Pr} = \tau = 0.03$ and $R_0^{-1} = 1.5$. The bottom row shows similar figures for a non-layered simulation with the same values of Pr and τ and $R_0^{-1} = 5$.

equations over small length scales and short time scales. There are assumed to be no mean flows, and the layering perturbations grow only in the temperature and chemical composition fields, allowing the momentum equation to be neglected altogether. Ignoring all horizontal spatial derivatives, what remains are equations for perturbations to the spatially and temporally averaged temperature, $\overline{T}$, and chemical composition, $\overline{\mu}$, fields given by

$$\begin{aligned} \frac{\partial \overline{T}}{\partial t} &= -\frac{\partial F_T^{\mathrm{tot}}}{\partial z}\,, \\ \frac{\partial \overline{\mu}}{\partial t} &= -\frac{\partial F_\mu^{\mathrm{tot}}}{\partial z}\,, \end{aligned} \tag{1.16}$$

where $F_T^{\rm tot}$ and $F_\mu^{\rm tot}$ are the total fluxes of temperature and chemical composition through the domain. In the following calculations it is useful to explicitly define the thermal Nusselt number, Nu_T, as,

$$\mathrm{Nu}_T = \frac{F_T^{\rm tot}}{1 - \frac{d\overline{T}}{dz}} \,, \tag{1.17}$$

as well as the inverse flux ratio, $\gamma_{\rm tot}^{-1}$, as,

$$\gamma_{\rm tot}^{-1} = \frac{F_\mu^{\rm tot}}{F_T^{\rm tot}} \,. \tag{1.18}$$

In terms of these parameters the equations for $\overline{T}$ and $\overline{\mu}$ become,

$$\begin{aligned} \frac{\partial \overline{T}}{\partial t} &= \frac{\partial}{\partial z}\left[\left(1 - \frac{\partial \overline{T}}{\partial z}\right)\mathrm{Nu}_T\right] \,, \\ \frac{\partial \overline{\mu}}{\partial t} &= \frac{\partial}{\partial z}\left[\gamma_{\rm tot}^{-1} F_T^{\rm tot}\right] \,. \end{aligned} \tag{1.19}$$

To solve these equations, we assume that the parameters Nu_T and $\gamma_{\rm tot}^{-1}$ only depend on Pr, τ, and the *local* inverse density ratio, R_ρ^{-1}, given by,

$$R_\rho^{-1} = \frac{R_0^{-1} - \frac{\partial \overline{\mu}}{\partial z}}{1 - \frac{\partial \overline{T}}{\partial z}} \,. \tag{1.20}$$

However, assuming $\overline{T}$ and $\overline{\mu}$ are small, R_ρ^{-1} can be approximated to first order as

$$R_\rho^{-1} \approx R_0^{-1}\left(1 - \frac{1}{R_0^{-1}}\frac{d\overline{\mu}}{dz} + \frac{d\overline{T}}{dz}\right) \tag{1.21}$$

Under these assumptions the spatially and temporally averaged thermal evolution equation becomes,

$$\frac{\partial \overline{T}}{\partial t} = -A_2 \left(\frac{1}{R_0^{-1}} \frac{\partial^2 \overline{\mu}}{\partial z^2} - \frac{\partial^2 \overline{T}}{\partial z^2} \right) + \mathrm{Nu}_0 \frac{\partial^2 \overline{T}}{\partial z^2} \tag{1.22}$$

where Nu_0 is the value of Nu_T after the primary ODDC instability saturates and the system is in a homogeneously mixed state and where,

$$A_2 = -R_0^{-1} \left. \frac{d\mathrm{Nu}_T}{dR_\rho^{-1}} \right|_{R_0^{-1}} \tag{1.23}$$

Likewise, the compositional evolution equation becomes,

$$\frac{\partial \overline{\mu}}{\partial t} = \gamma_0^{-1} \frac{\partial \overline{T}}{\partial t} - A_1 \mathrm{Nu}_0 \left(\frac{1}{R_0^{-1}} \frac{\partial^2 \overline{\mu}}{\partial z^2} - \frac{\partial^2 \overline{T}}{\partial z^2} \right) \tag{1.24}$$

where γ_0^{-1} is the value of $\gamma_{\mathrm{tot}}^{-1}$ in the homogeneously mixed state and where,

$$A_1 = -R_0^{-1} \left. \frac{d\gamma_{\mathrm{tot}}^{-1}}{dR_\rho^{-1}} \right|_{R_0^{-1}} \tag{1.25}$$

In these evolution equations, the parameters A_1 and A_2 must be estimated through empirical measurements of thermal and compositional flux from numerical simulations.

Then by assuming functional forms for $\overline{T}$ and $\overline{\mu}$ of $(\overline{T}, \overline{\mu}) = (\hat{\overline{T}}, \hat{\overline{\mu}}) e^{ikz + \Lambda t}$ the following dispersion relation can be calculated,

$$\Lambda^2 + \Lambda k^2 \left[A_2 \left(1 - \frac{\gamma_0^{-1}}{R_0^{-1}} \right) + \mathrm{Nu}_0 \left(1 - \frac{A_1}{R_0^{-1}} \right) \right] - \frac{k^4 A_1 \mathrm{Nu}_0^2}{R_0^{-1}} = 0 \, . \tag{1.26}$$

From this equation it can be shown that growing solutions of Λ only occur when $\gamma_{\mathrm{tot}}^{-1}$ is a decreasing function of R_0^{-1}. Also, growth rates can be calculated for given values of k. By taking measurements from simulations of ODDC, Rosenblum et al.

(2011) showed that for smaller values of R_0^{-1}, γ_{tot}^{-1} is decreasing function of R_0^{-1}, and for large values it is an increasing function. They confirmed that layers only spontaneously formed for simulations where γ_{tot}^{-1} was a decreasing function (see Figure 1.5). Also they confirmed that the predicted growth rates for layering modes was consistent with the growth rates observed in numerical simulations.

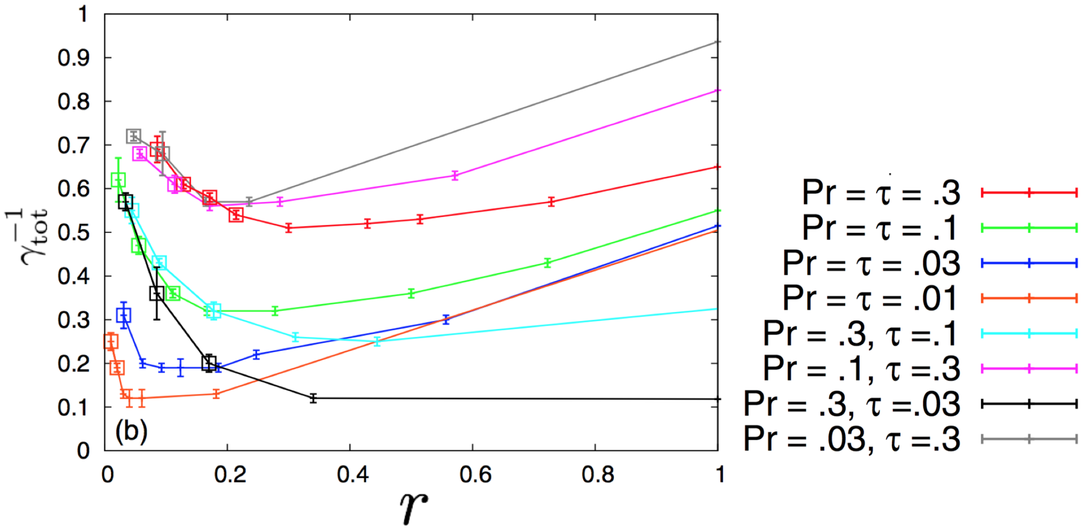

Figure 1.4: Figure 5 from Mirouh et al. (2012) showing γ_{tot}^{-1} as a function of r for stated values of Pr and τ. Points with squares represent simulations with spontaneous layer formation, and only occur when γ_{tot}^{-1} is a decreasing function of r.

Mirouh et al. (2012) built on the work of Rosenblum et al. (2011) by developing a semi-analytical rule for identifying the regions of parameter space where layers naturally form, and where they do not. They found that layers can only spontaneously form if $1 < R_0^{-1} < R_L^{-1} < R_c^{-1}$, where R_L^{-1} is typically of order $\text{Pr}^{-\frac{1}{2}}$. They also determined that non-layered regime of ODDC, which occurs when $R_L^{-1} < R_0^{-1} < R_c^{-1}$, is ultimately dominated by large-scale internal gravity waves (see the bottom row of Figure 1.3) which (surprisingly) also augment thermal and compositional transport, though not as much as in the layered case. This we be described in more detail in Chapter 2.

Wood et al. (2013) then studied the dynamics and transport properties of layered ODDC ($1 < R_0^{-1} < R_L^{-1}$). Specifically they identified how thermal on compositional fluxes scaled with the thermal Rayleigh number, Ra_T, given in terms of dimensional parameters by,

$$\mathrm{Ra}_T = \frac{\alpha g \left| T_{0z} - T_{0z}^{\mathrm{ad}} \right| (H_L d)^4}{\kappa_T \nu} = H_L^4 \tag{1.27}$$

where H_L is the non-dimensional layer height. Figure 1.5 shows their results from a simulation in a tall, thin domain that initially form 8 layers. As the layers merged and the remaining layers became taller, measurements of the fluxes were taken so that they could be plotted as a function of Ra_T. Their findings were consistent with earlier studies of transport through layered double diffusive convection, and showed that

$$\begin{aligned} \mathrm{Nu}_T - 1 &\propto (\mathrm{Pr}\mathrm{Ra}_T)^{1/3} \ , \\ \mathrm{Nu}_\mu - 1 &\propto (\mathrm{Pr}\mathrm{Ra}_T)^{1/3} \ . \end{aligned} \tag{1.28}$$

The work presented in this document further investigates ODDC and double diffusive layering through numerical simulations using the PADDI code. As a natural progression from Wood et al. (2013), Chapter 2 focuses on characterizing the behavior of non-layered ODDC when $R_L^{-1} < R_0^{-1} < R_c^{-1}$ and quantifying the associated thermo-compositional mixing it induces. In Chapter 3 we consider how global rotation influences the growth and long term behavior of ODDC, with emphasis on how rotation effects layer formation. In Chapter 4, we study how finite amplitude perturbations may be used to excite layer formation, even in the parameter regime where they do not form through the γ-instability. Finally, we

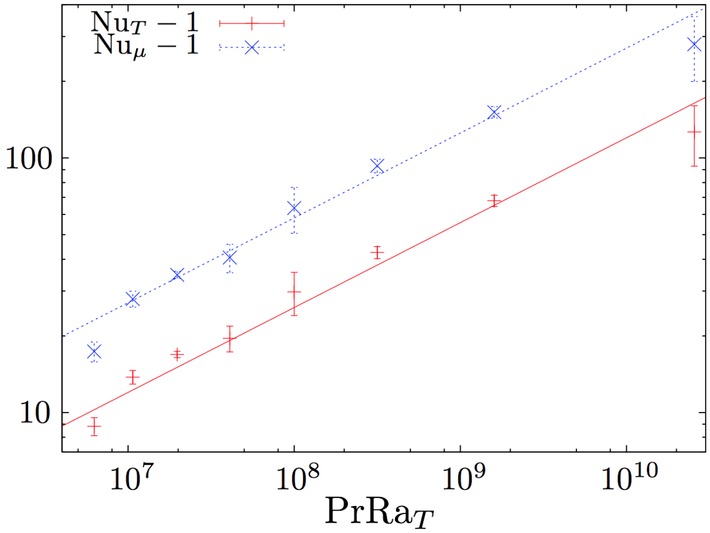

Figure 1.5: Figure 5 from Wood et al. (2013) showing measure thermal and compositional fluxes as a function of PrRa_T. The solid lines are the functions where $\mathrm{Nu}_{T,\mu} \propto (\mathrm{PrRa}_T)^{1/3}$

summarize our conclusions, and discuss future avenues of research in Chapter 5.

Chapter 2

Non-Layered ODDC

The following chapter is composed of the main text of Moll et al. (2016), published in The Astrophysical Journal in May of 2016. The co-authors of this work are Pascale Garaud, professor of applied mathematics at the University of California at Santa Cruz, and Stephan Stellmach of the Institut für Geophysik, Westfälische Wilhelms-Universität Münster.

2.1 Introduction

As discussed in Chapter 1, previous work in our group focussed on understanding the conditions for layer formation in ODDC (Mirouh et al., 2012) and the dynamics of layered convection (Wood et al., 2013). In this Chapter, we complete their study and investigate the dynamics of non-layered ODDC. To do so, we solve the model equations discussed in Chapter 1, with the PADDI code developed by S. Stellmach.

In Section 2.2, we describe the evolution of a typical non-layered simulation and discuss the difficulties of running numerical simulations in extreme parameter regimes. In Section 2.3, we discuss the effectiveness of 2D simulations for modeling

ODDC compared to the full 3D DNS. We present the results of our numerical experiments in 2D and 3D, focussing in particular on the measurements of thermal and compositional fluxes in Section 2.4. Finally, in Section 3.7, we summarize the findings of papers I, II, and III of this series, and discuss them in the context of previous work and applications to astrophysics.

2.2 Behaviors of ODDC

In what follows, we show the results of a typical ODDC simulation, which has $\mathrm{Pr} = \tau = 0.03$ and $R_0^{-1} = 7.87$, and was run at a resolution of 192^3 (the simulation domain has dimensions $(100d)^3$). Note that for these parameters, $R_L^{-1} \simeq 2.5$ (Mirouh et al., 2012) and $R_c^{-1} \approx 17.2$, so this value of R_0^{-1} is indeed in the range $R_L^{-1} < R_0^{-1} < R_c^{-1}$ which is unstable to ODDC, but where layers do not spontaneously form through the γ-instability. We first describe these results purely qualitatively, then move on to a more quantitative analysis.

2.2.1 Qualitative study

Figure 2.1 shows the vertical component of the velocity field at early times, and Figure 2.2 shows the y-component of the velocity field later on in the simulation. At very early times, we first see the development of the fastest growing modes of the basic instability of ODDC, which resemble tubes of vertically oscillating fluid (shown in Figure 2.1a). This primary growth phase ends when the basic instability saturates due to nonlinear interactions inherent to the problem (see Figures 2.1b).

As previously discussed by Mirouh et al. (2012), after the primary saturation, the small-scale fastest growing modes of the primary instability stop growing but

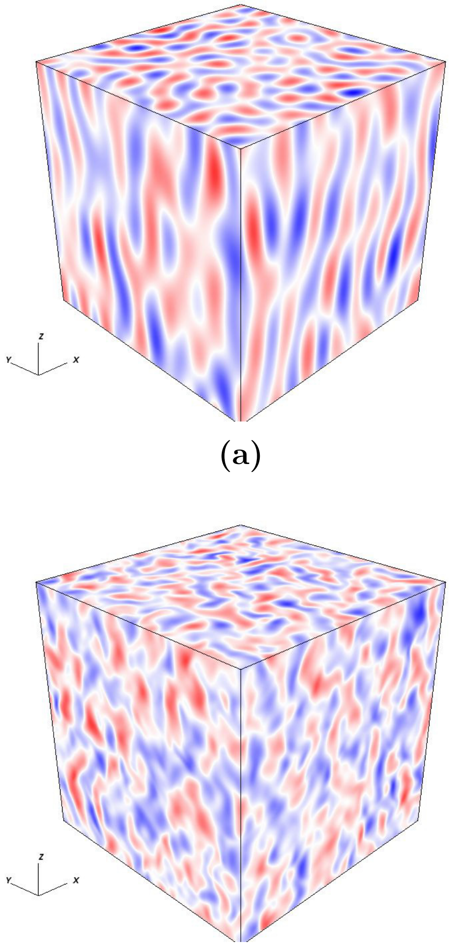

(a)

(b)

Figure 2.1: Figure 2.1a shows the vertical component of the velocity field during the basic instability growth phase (here at $t = 2508$), with red and blue signifying upward and downward motion, respectively. Figure 2.1b shows the vertical component of the velocity field at the saturation of the primary instability (here at $t = 2868$). For each figure, $R_0^{-1} = 7.87$ and $\mathrm{Pr} = \tau = 0.03$.

other larger-scale modes slowly continue to gain energy, amounting to a secondary phase of growth. From Figure 2.2a we see that the latter (which ultimately come to dominate the energetics of the system) generally have the largest possible scale in the horizontal direction. As the system evolves, energy is funneled into modes of progressively larger vertical scale until the secondary growth phase saturates and the system reaches a statistically stationary state. The dynamics of this state are characterized by gravity wave oscillations on fast timescales whose amplitudes are modulated chaotically and intermittently. This intermittency appears to be caused by nonlinear interactions between large scale gravity modes and large scale horizontal shearing modes. Indeed, we regularly observe the emergence of a strong horizontal shear layer that temporarily suppresses the wave field (Figure 2.2b). The shear then dissipates, and the system proceeds as before. Figure 2.2 shows the distinct differences in the y velocity field between a gravity-wave-dominated phase and a shear-dominated phase.

2.2.2 Quantitative study

In order to study this system in a more quantitative way we now investigate the energy contained in individual modes. We shall refer to specific spatial modes by the number of wavelengths in the x, y, and z directions. So mode (l, m, k) would refer to a mode with horizontal wave numbers $\frac{2\pi l}{L_x}$ and $\frac{2\pi m}{L_y}$ (in the x and y directions), and vertical wave number $\frac{2\pi k}{L_z}$ (in the z direction). We can quantify the transfer of energy to larger scales by considering the amount of energy in a mode “family". A family of modes consists of all the modes with equivalent spatial structures given the symmetries between the x and y directions in the domain, and negative and positive wave numbers in each spatial direction. For example, the mode family 102 contains the modes (1,0,2) , (-1,0,2) , (0,1,2) , (0,-1,2) , (1,0,-2)

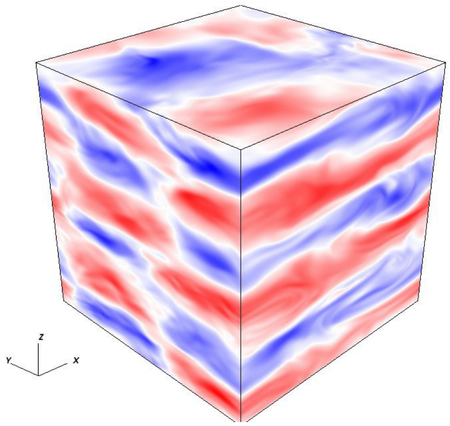

(a)

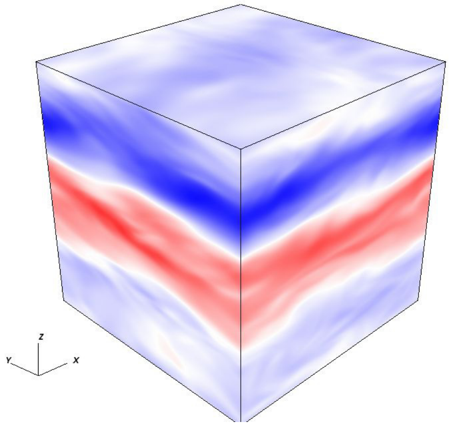

(b)

Figure 2.2: The Figures 2.2a and 2.2b show, respectively, the velocity field in the y direction at times when the system is dominated by gravity waves (here at $t = 20758$) and when the system is dominated by shear (here at $t = 24718$). Here red and blue represent motion in the positive and negative y direction. As with the snapshots in Figure 2.1, $R_0^{-1} = 7.87$ and $\mathrm{Pr} = \tau = 0.03$.

, (-1,0,-2) , (0,1,-2) , (0,-1,-2) (Traxler et al., 2011).

Consistent with the qualitative results in Figure 2.2a, Figure 2.3 shows that at early times, the dynamics of ODDC are dominated by modes that have small horizontal scales ($\sqrt{l^2 + m^2} \approx 8$), with no structure in the vertical direction (with vertical wavenumber $k = 0$). Around $t = 2500$, the primary instability saturates. Mirouh et al. (2012) demonstrated that the level at which the primary instability saturates can be used to identify regions of parameter space where layer formation is expected to occur. However, the primary saturation level is of little use for characterizing the long term transport properties of non-layered ODDC because a secondary growth phase occurs after primary saturation, further augmenting the thermal and compositional fluxes. From Figure 2.4, we see that while the fastest growing modes of the primary instability stop growing at saturation, the mode family (1,0,5) continues to grow, and for a brief time becomes the most energetic mode family in the system. As time goes on, however, the mode family (1,0,4) supplants (1,0,5) as the most energetic, which is in turn overtaken by the mode family (1,0,3). For this particular simulation, the handoff of energy to progressively larger scales stops with mode family (1,0,3); mode family (1,0,2) never becomes dominant. Crucially, Figures 2.3 and 2.4 also reveal the growth of the energy in large scale shearing modes with purely horizontal fluid motions (mode families (0,0,1) and (0,0,2)). This is unexpected because these modes are not directly excited by the primary instability of ODDC. Instead their growth must arise from nonlinear interactions between rapidly growing ODDC modes.

Around $t = 5000$, after the mode family (1,0,3) becomes dominant, the secondary growth phase appears to end, saturating into a statistically steady turbulent state. However, Figure 2.4 shows periodic bursts of growth in the shearing mode energies, suggesting intermittent (yet powerful) interactions between the

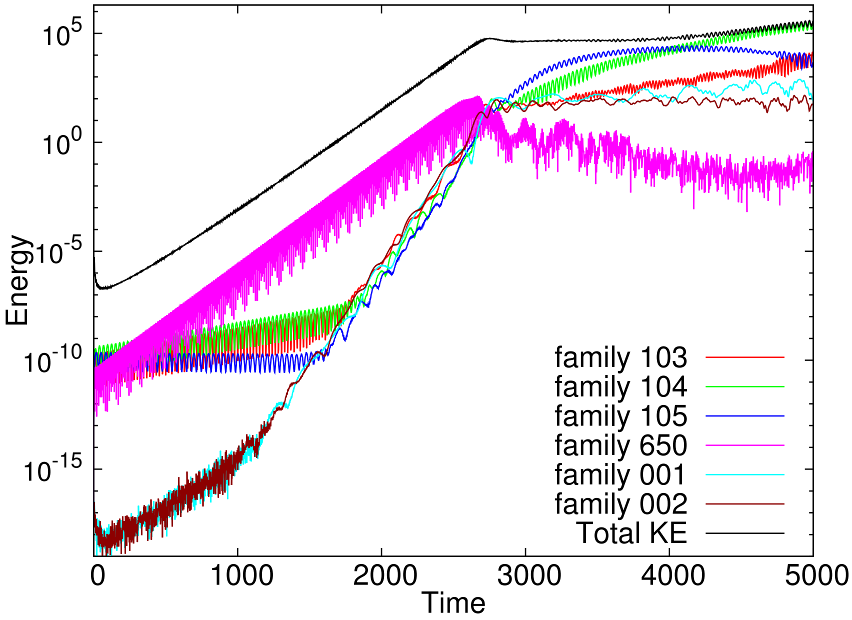

Figure 2.3: Total kinetic energy vs. time for various families of modes (see main text for detail) for a simulation with $\mathrm{Pr} = \tau = 0.03$ and $R_0^{-1} = 7.87$. Shown is the early part of a simulation where the total kinetic energy is dominated by modes that are predicted to grow the fastest according to linear theory. The mode family (6,5,0) is one of the fastest growing mode families.

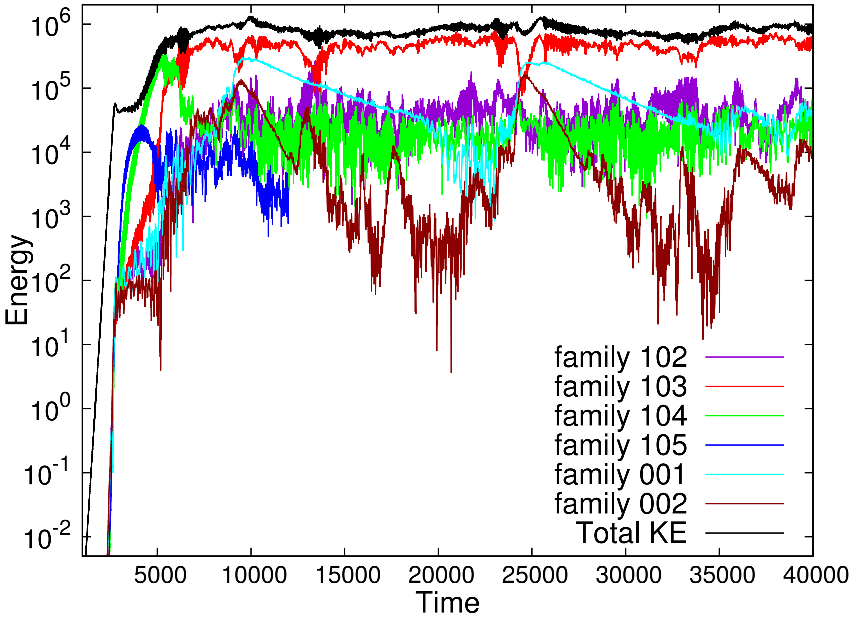

Figure 2.4: As in Figure 2.3 (same parameters), but now focusing on the long-term evolution of the system. After the saturation of the primary instability, large scale gravity waves begin to grow and energy becomes more concentrated in larger scale modes as time goes on. Large scale shearing mode families (mode families (0,0,1) and (0,0,2)) also grow to large amplitude.

shearing modes and the dominant gravity wave modes. In these interactions, illustrated in more detail in Figure 2.5, the growth of gravity waves excites the rapid growth of horizontal shearing modes, which in turn causes a decay in the amplitude of the waves. Without the wave field to amplify it, the shear then decays viscously. This finally allows the energy in the gravity waves to ramp back up again. While this interaction does not always manifest itself as such a distinct relaxation oscillation, it is still present in one form or another in all gravity-wave-dominated ODDC simulations. Figure 2.5 also shows that the interaction between the shear and gravity waves leads to intermittent modulation of the thermal and compositional fluxes, a result which may have some observational implications (see Section 2.4).

While the intermittency in the fluxes caused by the shear is interesting in its own right, for the purpose of modeling transport by ODDC in planetary or stellar evolution calculations, we are more concerned with estimating the mean fluxes over significant periods of time. These mean fluxes at secondary saturation depend on the parameters of the system (R_0^{-1}, Pr, and τ). The results shown in this section, which were obtained at moderate R_0^{-1} and moderate Pr and τ, suggest that turbulent transport in non-layered ODDC is weak. Indeed, Figure 2.5 shows that Nu_T and Nu_μ remain of order unity throughout the simulations. To determine whether this is a generic property of ODDC at $R_0^{-1} > R_L^{-1}$, we need to run numerical experiments at larger R_0^{-1} and smaller Pr and τ. Probing this region of parameter space is difficult, however, because 3D simulations at low Pr and τ can be computationally very expensive, particularly for values of R_0^{-1} that are close to marginal stability $\left(R_0^{-1} \rightarrow \frac{\mathrm{Pr}+1}{\mathrm{Pr}+\tau}\right)$. Small values of Pr and τ lead to small-scale turbulent features with steep gradients of velocity, temperature, and composition, which necessitate high spatial resolution. Furthermore, a larger

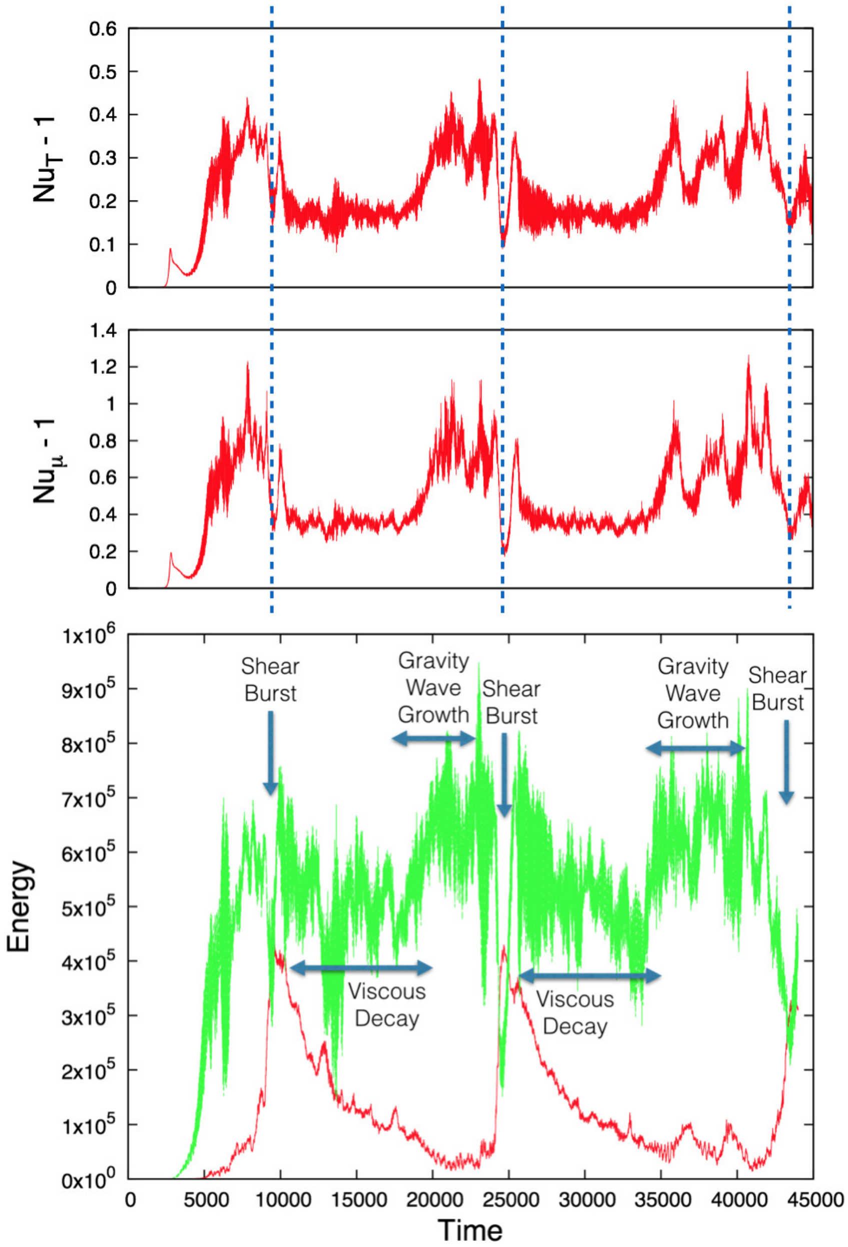

Figure 2.5: The top figures show the temperature and composition Nusselt numbers, which are related to the turbulent fluxes by the equations in (1.15). Shown in the bottom figure is the total kinetic energy in the large-scale gravity waves (modes from the families (1,0,n)) in green, and the kinetic energy in the background shear (modes from the families (0,0,m)) in red, as a function of time. The vertical lines mark times at which there are bursts of energy in the shear. The simulation parameters used here are $\mathrm{Pr} = \tau = 0.03$, and $R_0^{-1} = 7.87$.

R_0^{-1} implies a larger buoyancy frequency $\left(\text{since } N = \sqrt{\mathrm{Pr}(R_0^{-1} - 1)}\right)$, and leads to higher frequency oscillations of the basic ODDC modes, necessitating smaller time steps. Given these challenges, in the next section we discuss the possibility of using 2D ODDC simulations as a potential surrogate for full 3D simulations at these extreme regions of parameter space.

2.3 2D simulations

Simulations of 2D ODDC are computationally inexpensive and are also less intensive in terms of data storage than 3D simulations. For this reason, we have run a series of tests to compare both the qualitative behavior and quantitative estimates of the fluxes (and other system diagnostics) in 2D and 3D. Simulations in 2D and 3D often lead to very different types of dynamics, especially at low Pr (Schmalzl et al., 2004; van der Poel et al., 2013; Garaud & Brummell, 2015). Fortunately however, as we see from Figure 2.6, the secondary saturation level in the 2D simulation at $\mathrm{Pr} = \tau = 0.03$ and $R_0^{-1} = 7.87$ is very similar to that of the 3D simulation analyzed in the previous section. This is, in fact, generally the case for each parameter set (Pr,τ,R_0^{-1}) at $R_0^{-1} > R_L^{-1}$ where we have both 2D and 3D simulations.

Measurements of mode family energies show that key physical processes that dictate the behavior of 3D ODDC simulations are present in the 2D simulations as well. Figure 2.7 explores the energetics of the gravity waves and shear, and shows that the fractions of energy in each type of mode are of the same in order in both cases. This is important because together these two types of modes contain most of the energy in non-layered systems after secondary saturation.

The computational economy of 2D simulations makes other types of analysis easier as well, such as running simulations in larger domains. In the previous

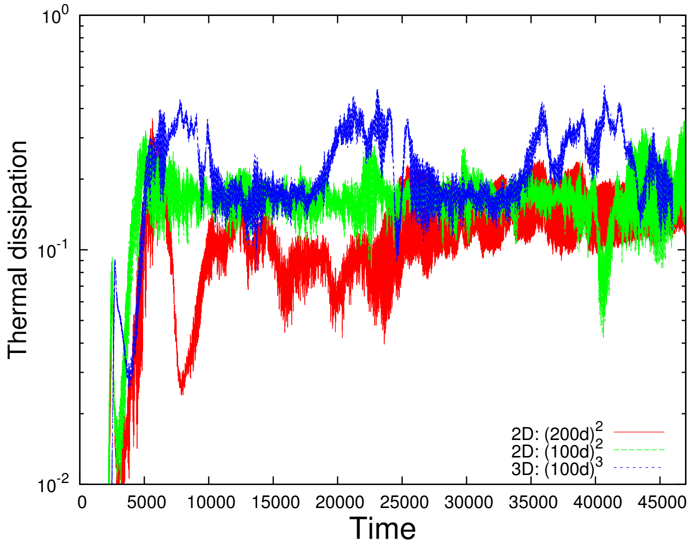

(a)

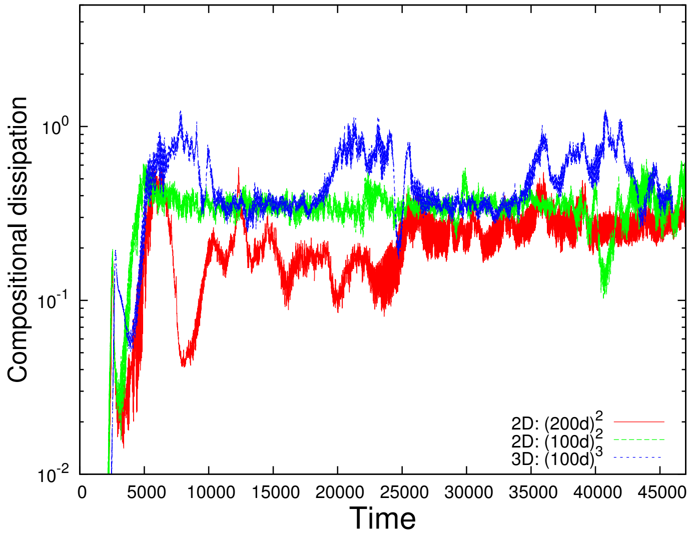

(b)

Figure 2.6: Figures 2.6a and 2.6b show the thermal and compositional dissipations vs. time for the simulation with $\mathrm{Pr} = \tau = 0.03$ and $R_0^{-1} = 7.87$. Included are data from a 3D simulation, and two 2D simulations with differing domain sizes. While the larger 2D simulation takes longer to achieve its statistically stationary state, the mean fluxes are ultimately very similar for all three runs.

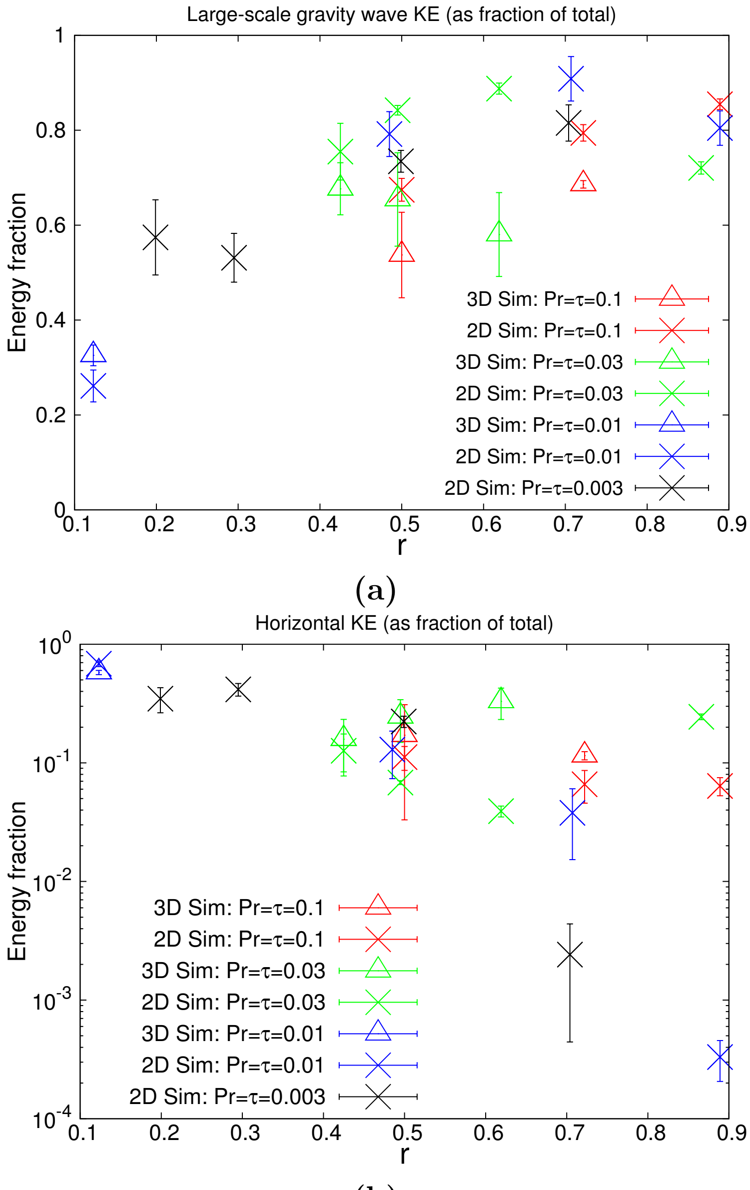

(a)

(b)

Figure 2.7: Figure 2.7a shows the energy in gravity wave families of the form (1,0,n) as a percentage of the total energy in the system. Figure 2.7b shows the energy in shearing modes families of the form (0,0,m) as a percentage of the total energy. We estimate errors according to the method described in Section 2.4.

section, we showed that after primary saturation the dominant gravity wave modes have horizontal wavelengths commensurate with the domain size. Also we showed that energy is transferred to modes with progressively larger vertical wavelengths. This raises the question of whether this energy transfer would always terminate at a vertical wavelength that depends on the domain size. For example, will the dominant mode after secondary saturation in a $(200d)^3$ domain have a vertical wavelength that is twice that of the dominant mode in a $(100d)^3$ domain? More importantly, do the fluxes depend on the domain size?

Using 2D data we find that in all but one case, doubling the domain size in each direction leaves the vertical wavelength of the dominant mode unchanged. By contrast, the horizontal wavelength of the dominant mode always grows to the largest possible scale allowed by the domain. As a consequence, the dominant modes in the larger boxes are inclined more toward the horizontal than in the smaller ones. Importantly though, Figures 2.6a and 2.6b show that despite some qualitative differences between simulations with domains of different dimensions, we find that the time-averaged fluxes of temperature and chemical composition do not depend strongly on box size (they are within $\sim 10\%$ of one another). In the next section we shall therefore rely heavily on 2D simulations to draw conclusions about turbulent fluxes through non-layered ODDC.

2.4 Results and Discussion

We now analyze the results of all numerical experiments done in 2D and 3D computational domains. We evaluate thermal and compositional fluxes in terms of the Nusselt numbers, which we calculate from thermal and compositional dissipation data, as described in (1.15). More specifically, the quantities we consider are $\mathrm{Nu}_T - 1$ and $\mathrm{Nu}_\mu - 1$ which, conveniently, are also measures of the turbulent fluxes in units of the diffusive fluxes. To find typical Nusselt numbers for a simulation we calculate time averaged values for the period after secondary saturation.[1] To estimate errors we first divide the time average domain into 10 bins. We then take the average of each bin and calculate the standard deviation of the individual bin averages from the overall average.

Figure 2.8 shows the thermal and compositional Nusselt numbers calculated in both cases, for various values of Pr and τ. From this figure we also see that the reasonable agreement between 2D and 3D simulations discussed in Section 2.3 persists in all cases studied.

The primary result of this analysis is that, while gravity waves consistently augment thermal and compositional transport in non-layered ODDC, the enhanced fluxes are only slightly larger than the transport due to thermal and molecular diffusion alone. Furthermore, this enhancement rapidly decreases with increasing R_0^{-1}. For the simulations we have run with the smallest values of R_0^{-1} (those closest to the layering threshold), the turbulent compositional flux is at most twice that of the flux due to diffusion alone and the turbulent heat flux is at most $\sim 20\%$ of the diffusive flux. However, at larger values of R_0^{-1}, closer to marginal stability, the turbulent fluxes drop down to $\sim 5-10\%$ of the diffusive fluxes. Critically, we also find that the turbulent fluxes decrease as Pr and τ decrease. The simulations run at the parameter regime most similar to actual giant planetary interiors ($\mathrm{Pr} = \tau = 0.003$) suggest that the mixing induced by non-layered ODDC at $R_0^{-1} > R_L^{-1}$ is effectively negligible in this case.

Another result of our analysis is that gravity wave dominated ODDC is responsible for the generation of large scale shear. In all the simulations we have run so far, the main effect of the shear has been to modulate the wave-induced

---

[1] We define the secondary saturation time to be the point at which the total kinetic energy of the system reaches a statistically stationary level, and we identified it by inspection.

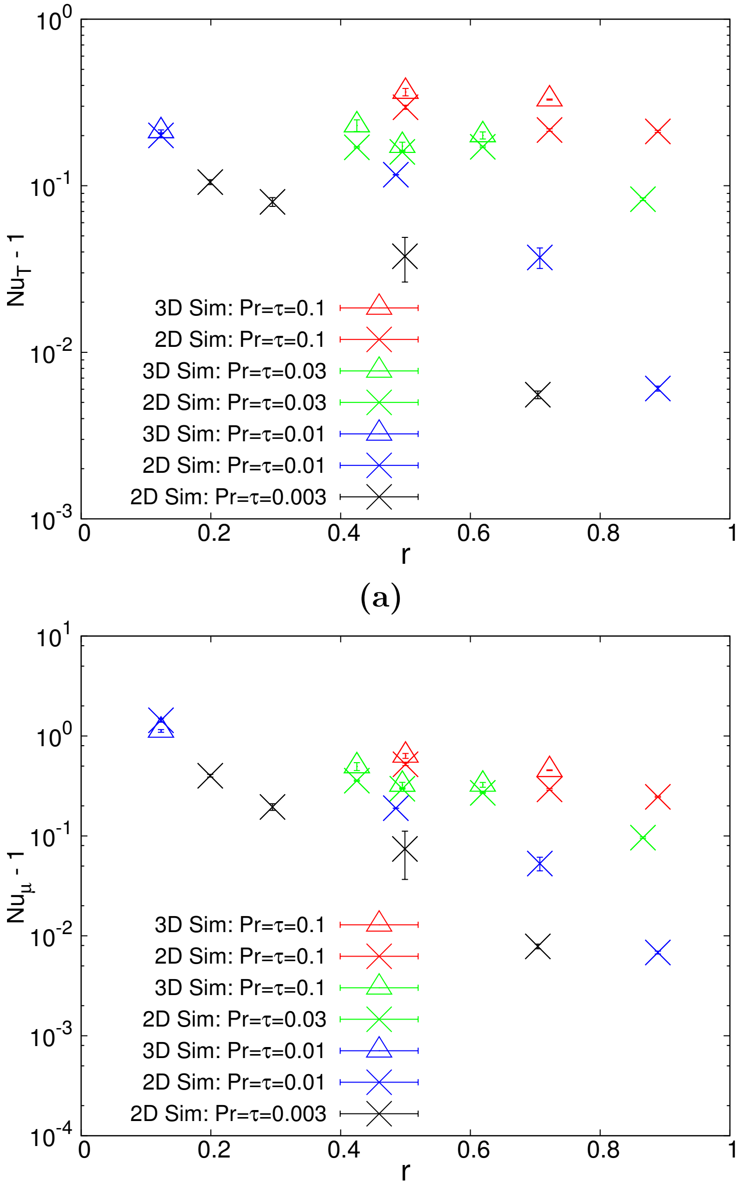

(a)

(b)

Figure 2.8: Figures 2.8a and 2.8b show the Nusselt numbers after secondary saturation for the available 3D and 2D simulations (in domains of size $100d^3$ or $100d^2$) as a function of r (which is related to R_0^{-1} by Equation 1.10). The secondary saturation level decreases as r increases and as Pr and τ decrease.

transport through strong non-linear interactions with the wave field. One might wonder, however, whether the shear could become strong enough in some parameter regimes to trigger a shear instability which would then dramatically augment turbulent transport. To evaluate the likelihood of this happening, we consider the Richardson number, Ri, which is the ratio of the potential energy needed to cause overturn to the available kinetic energy in the shear. In the units of this paper, we define the Richardson number as,

$$\mathrm{Ri}\,(z) = \frac{N^2}{|\frac{\partial \mathbf{u}}{\partial z}|^2} \simeq \mathrm{Pr}\left(\frac{R_0^{-1} - 1}{\left(\frac{d\bar{u}}{dz}\right)^2 + \left(\frac{d\bar{v}}{dz}\right)^2}\right), \tag{2.1}$$

where N is the buoyancy frequency, defined dimensionally as $N^2 = -g\frac{d\ln\rho}{dz}$ where ρ is the background density profile. The terms $\bar{u}$ and $\bar{v}$ are the horizontally averaged x and y components of velocity, respectively (for 2D simulations $v = 0$ everywhere, for all time). To calculate the typical minimum Richardson number for a simulation we find the minimum of $\mathrm{Ri}(z)$ for an individual time step, and then take a time average of $\mathrm{Ri}_{\mathrm{min}}(z)$ over the period after secondary saturation. A plot of the time-averaged minimum Richardson number of the available simulations (Figure 2.9) shows that $\mathrm{Ri}_{\mathrm{min}}$ increases as r (or equivalently, R_0^{-1}) increases. This is due to the fact that by definition systems with higher R_0^{-1} have a stronger stabilizing compositional stratification compared to their unstable thermal stratification, making them less susceptible to overturning. Also, recall from Figure 2.7 that simulations with higher values of R_0^{-1} have a lower percentage of their total kinetic energy in shearing modes. This Richardson number data therefore suggests that if any shear-induced instabilities were to present themselves, they would do so at values of R_0^{-1} that are very close to R_L^{-1}, the threshold for the layering instability.

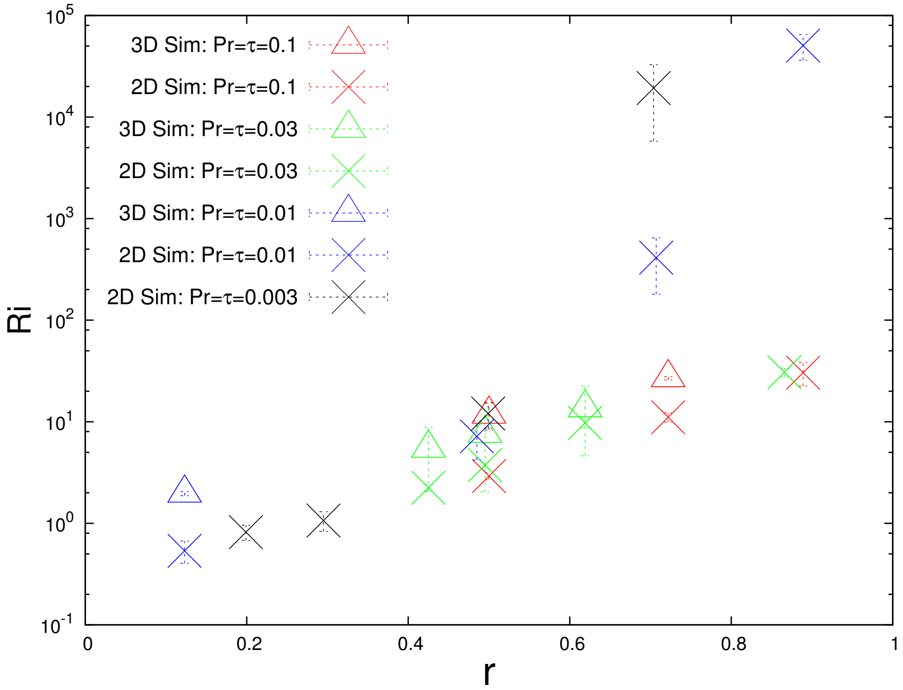

Figure 2.9: Time- and horizontally-averaged minimum Richardson number as a function of R_0^{-1}. Included are data from all available 2D and 3D simulations (in domains of size $100d^3$ or $100d^2$).

To summarize our results so far, we have found that mixing induced by non-layered ODDC at $R_0^{-1} > R_L^{-1}$ is mostly negligible with turbulent fluxes at most of the order of diffusive fluxes (usually several orders of magnitude smaller). The propensity for gravity wave dominated ODDC to drive shear could be observationally interesting, however.

2.5 Conclusion

2.5.1 Synthesis of results from papers I, II and III

This study marks the conclusion of a series of papers aimed at describing the thermal and compositional flux properties of ODDC (semi-convection), throughout the entire linearly unstable range for fluid parameters appropriate to stellar and planetary interiors. Rosenblum et al. (2011) laid the groundwork for this series by conducting a preliminary survey of the ODDC parameter space and identified that ODDC either spontaneously forms layers, or remains in a non-layered, mildly turbulent state, which Mirouh et al. (2012) later showed to be dominated by large scale gravity waves. They also showed that the critical parameter to making predictions about layer formation is the inverse total flux ratio γ_{tot}^{-1} defined as

$$\gamma_{\text{tot}}^{-1} = \tau R_0^{-1} \frac{\text{Nu}_\mu}{\text{Nu}_T} \,. \tag{2.2}$$

More precisely, Rosenblum et al. (2011) showed that through the γ-instability (which was initially developed to describe the conditions that lead to layer formation in fingering convection; Radko, 2003) layers only form when

$$\frac{d\gamma_{\text{tot}}^{-1}}{dR_0^{-1}} < 0 \,. \tag{2.3}$$

Next, Mirouh et al. (2012) (Paper I) produced a semi-analytical model for γ_{tot}^{-1} given by

$$\gamma_{\text{tot}}^{-1} = \frac{\tau R_0^{-1} + \gamma_{\text{turb}}^{-1} \left(\text{Nu}_T - 1\right)}{1 + \left(\text{Nu}_T - 1\right)} \,. \tag{2.4}$$

They used the following empirically motivated prescription for $\text{Nu}_T - 1$:

$$\text{Nu}_T - 1 = (0.75 \pm 0.05) \left(\frac{\text{Pr}}{\tau}\right)^{0.25\pm0.15} \frac{1-\tau}{R_0^{-1} - 1} \left(1 - r\right) \,,$$

where r is the quantity defined in Equation (1.10). Meanwhile, $\gamma_{\text{turb}}^{-1}$ is the inverse *turbulent* flux ratio, and is expressed only in terms of parameters that can be calculated through a linear analysis of the original governing equations in (1.7).

It is defined as

$$\gamma_{\rm turb}^{-1} = \frac{\langle \tilde{w}\tilde{\mu}\rangle}{\langle \tilde{w}\tilde{T}\rangle} = R_0^{-1}\frac{(\lambda_{\rm R}+l^2)+\lambda_{\rm I}^2}{(\lambda_{\rm R}+\tau l^2)+\lambda_{\rm I}^2}\frac{\lambda_{\rm R}+\tau l^2}{\lambda_{\rm R}+l^2}\,, \tag{2.5}$$

where $\lambda_{\rm R}$ and $\lambda_{\rm I}$ are the real and imaginary parts of the growth rate of the fastest growing mode of the primary instability of ODDC for a given parameter set (R_0^{-1}, Pr, τ) and l is the corresponding horizontal wavenumber of the fastest growing mode (see their appendix for an explanation on how l, $\lambda_{\rm R}$ and $\lambda_{\rm I}$ are calculated, as well as analytical approximations in the limit of small Pr and τ).

Using their model for $\gamma_{\rm tot}^{-1}$, Mirouh et al. (2012) were able to predict the range of R_0^{-1} where spontaneous layer formation is possible. The function $\gamma_{\rm tot}^{-1}$ is concave-up with a single minimum, so by identifying the value of R_0^{-1} at which $\gamma_{\rm tot}^{-1}$ reaches its minimum (referred to as $R_{\rm L}^{-1}$) it is possible to identify the region of parameter space where layers naturally form from infinitesimal perturbations ($R_0^{-1} < R_{\rm L}^{-1}$) and where they do not ($R_0^{-1} > R_{\rm L}^{-1}$). They found that, typically

$$r_{\rm L} = \frac{R_{\rm L}^{-1}-1}{R_{\rm c}^{-1}-1} \sim {\rm Pr}^{\frac{1}{2}} \quad \text{and} \quad R_L^{-1} \sim {\rm Pr}^{-\frac{1}{2}}. \tag{2.6}$$

Wood et al. (2013) (Paper II) then presented prescriptions for quantifying the thermal and compositional fluxes through layered systems in cases where $R_0^{-1} < R_L^{-1}$. They found that the thermal and compositional fluxes are,

$$\begin{aligned} F_T &= -\rho c_p \kappa_T \left[({\rm Nu}_T - 1)\left(T_{0z} - T_{0z}^{\rm ad}\right) + T_{0z}\right] = -\frac{\rho c_p \kappa_T T}{p}\frac{\partial p}{\partial r}\left[{\rm Nu}_T(\nabla - \nabla_{\rm ad}) + \nabla_{\rm ad}\right] \quad , \\ F_\mu &= -{\rm Nu}_\mu \kappa_\mu \mu_{0z} = -\frac{{\rm Nu}_\mu \kappa_\mu \mu}{p}\frac{\partial p}{\partial r}\nabla_\mu \,. \end{aligned} \tag{2.7}$$

Alternately, the transport of chemical species can be expressed as an effective diffusivity defined as

$$D_{\mathrm{eff},\mu} = \mathrm{Nu}_\mu \kappa_\mu \,. \tag{2.8}$$

In the above equations, the Nusselt numbers Nu_T and Nu_μ can be modeled as,

$$\begin{aligned} \mathrm{Nu}_T - 1 &= \mathrm{A}_T \mathrm{Ra}_T^a \mathrm{Pr}^b \quad , \\ \mathrm{Nu}_\mu - 1 &= \mathrm{A}_\mu \tau^{-1} \mathrm{Ra}_T^c \mathrm{Pr}^d \,, \end{aligned} \tag{2.9}$$

where $\mathrm{A}_T \simeq 0.1$ and $\mathrm{A}_\mu \simeq 0.03$, and where $a = 0.34 \pm 0.01$, $b = 0.34 \pm 0.03$, $c = 0.37 \pm 0.01$, and $d = 0.27 \pm 0.04$. The parameter Ra_T is the thermal Rayleigh number for layered convection, and is defined as a function of the layer height, H,

$$\mathrm{Ra}_T(H) = \left(\frac{H}{d}\right)^4 = \frac{\alpha g \left|T_{0z} - T_{0z}^{\mathrm{ad}}\right| H^4}{\kappa_T \nu} = \frac{\alpha g H^4}{\kappa_T \nu} \left|\frac{\partial p}{\partial r}\right| \left|\nabla - \nabla_{\mathrm{ad}}\right| . \tag{2.10}$$

As discussed by Wood et al. (2013), it is not clear *a priori* what the value of H should be because in simulations of naturally layered systems, layers always gradually merge until only a single interface remains. This suggests that some other physical mechanism outside the scope of our model of ODDC determines layer height, or that layers may always merge indefinitely, leaving the fluid fully mixed. For now, it is left as a free parameter, much like the mixing length in mixing-length theory (see also Moore & Garaud, 2015).

Finally, from the work done in this paper (Paper III), we have found that the turbulent transport of heat and composition can more-or-less be neglected in the non-layered ODDC parameter space (i.e. $R_L^{-1} < R_0^{-1} < R_c^{-1}$). We therefore model the total heat and compositional fluxes as

$$\begin{aligned} F_T &= -\rho c_p \kappa_T \frac{dT}{dr} = -\frac{\rho c_p \kappa_T T}{p}\frac{\partial p}{\partial r}\nabla \quad , \\ F_\mu &= -\kappa_\mu \frac{d\mu}{dr} = -\frac{\kappa_\mu \mu}{p}\frac{\partial p}{\partial r}\nabla_\mu \, , \end{aligned} \tag{2.11}$$

and we can write the corresponding effective compositional diffusivity simply as

$$D_{\mathrm{eff},\mu} = \kappa_\mu \, . \tag{2.12}$$

Note that, as discussed by Moore & Garaud (2015), R_0^{-1} is typically much smaller than R_L^{-1} in stellar models where the semi-convective region is adjacent to a convection zone. Our conclusions for non-layered ODDC would therefore only apply to stellar models with a semi-convection zone that is detached from the convection zone, or possibly to planetary models.

2.5.2 Possible caveats to transport prescriptions

The model presented in Section 2.5.1 derives from a combination of "first-principle" theory and numerical experiments and has been demonstrated to provide a good-to-excellent fit to the macroscopic transport properties of ODDC in all available simulations. However, there are still potential sources of uncertainty in each of the three components of the model. Here we discuss uncertainty that may arise from the prescription for the layering cut-off, R_L^{-1}, described by Mirouh et al. (2012), the prescription for mixing in the layered case ($R_0^{-1} < R_L^{-1}$) proposed by Wood et al. (2013), and the prescription for mixing in the non-layered case ($R_L^{-1} < R_0^{-1} < R_c^{-1}$) described in this work. We also mention several specific circumstances under which we do not expect our model to remain valid.

As discussed by Mirouh et al. (2012), their proposed formula for R_L^{-1} is likely to overestimate the true R_L^{-1} by $20 - 40\%$ (see their study for an in depth explanation). This is not likely to affect stellar model predictions because in the most-commonly occurring stellar semi-convection zones R_0^{-1} is typically much smaller than R_L^{-1} (Moore & Garaud, 2015) meaning that their interiors are unambiguously in the regime where ODDC leads to spontaneous layer formation. In giant planets the effect of this uncertainty is less clear because no reliable estimates of R_0^{-1} exist.

Next are caveats on the Wood et al. (2013) prescription for layered ODDC. There are four sources of uncertainty in their scalings: that in the dependence on Pr and τ, on Ra_T, and on R_0^{-1}. Due to computational constraints, a limited range of values of Pr and τ was used to construct and test the model (between $\mathrm{Pr} = \tau = 0.01$ and $\mathrm{Pr} = \tau = 0.3$). While these values may be appropriate for the interiors of ice giant planets such as Uranus and Neptune (where Pr and τ are of order unity), and approximately valid in degenerate regions of stars and giant planets, such as Jupiter and Saturn (where Pr and τ are of order $10^{-3} - 10^{-4}$), they are very far from non-degenerate stellar values, where $\mathrm{Pr} \sim \tau \sim 10^{-6}$ or less. So using these diffusivities in a stellar parameter regime requires some degree of trust in the extrapolation from experimental values of Pr and τ down to stellar values. They should be appropriate, however, for models of giant planets.

The scaling of the Nusselt numbers with Ra_T (which suggests that the fluxes scale with the temperature difference and the compositional difference across the layers to the power of $\frac{4}{3}$) is the most robust because it is derived from arguments based purely on dimensional analysis (Turner, 1968; Radko, 2003). Note however, that some layered convection simulations with tall thin aspect ratios do deviate from this $\frac{4}{3}$ rule. This is seen in particular in the early work of Rosenblum et al. (2011), where the use of a tall, thin domain artificially caused Nu_T to scale with a weaker power of H than $\frac{4}{3}$. The wider simulations of Wood et al. (2013) do not suffer from this problem at low Ra_T. However, even in these simulations there inevitably comes a point where the horizontal dynamics of the layers become increasingly constrained by their aspect ratios because the layers themselves become taller and thinner as the mergers take place. This is an artificial effect created by the necessary constraint of the chosen simulation domain, and should not be expected to occur in an actual star or planet. In other words, $\mathrm{Nu}_T \propto (\mathrm{Ra_T Pr})^{\frac{1}{3}}$ and $\mathrm{Nu}_\mu \propto \mathrm{Ra_T}^{\frac{1}{3}}$ are expected to hold at any stellar value.

The greatest source of uncertainty in the Wood et al. (2013) scalings is the Nusselt numbers' dependence on R_0^{-1}. For the layered simulations studied in that work, R_0^{-1} was typically $\sim 1-3$ (due to computational constraints). However, at stellar values of Pr, layers can occur at inverse density ratios much larger than 10. In fact, for non-degenerate regions of a typical stellar interior $R_L^{-1} \sim 1000$. This naturally leads to the question of how Nu_T and Nu_μ scale with the inverse density ratio at large R_0^{-1}. While this line of inquiry is interesting in its own right from a hydrodynamic perspective, it is probably not relevant in semi-convective zones adjacent to convection zones in actual stars, where typical values of R_0^{-1} are more likely to be much closer to one (Moore & Garaud, 2015). For parameters relevant to giant planetary interiors, the layering threshold is $R_L^{-1} \sim 1-10$, so the simulations studied by Wood et al. (2013) spanned a substantial portion of the range of R_0^{-1} where layered convection occurs. Therefore, the Nusselt numbers' dependence on R_0^{-1} is not a significant source of uncertainty in the context of giant planets.

Finally, there are also uncertainties in our flux model for ODDC in the regime $R_L^{-1} < R_0^{-1} < R_c^{-1}$. First, in Equations (2.11) and (2.12) we simply chose to ignore the turbulent contribution to the fluxes due to non-layered ODDC on the grounds that it is usually very small, although the turbulent fluxes can admittedly be nearly as large as the diffusive fluxes when R_0^{-1} is close to the layering threshold R_L^{-1} (see Figure 2.8). We did this for simplicity, but the reader interested in improving the estimates for the total fluxes in that limit should feel free to add the turbulent fluxes as needed. Second, there is a more important model uncertainty which comes from the possibility that ODDC might yet take the form of layered convection, even when $R_0^{-1} > R_L^{-1}$. Indeed, there is a well-known subcritical branch of solutions (Huppert & Moore, 1976; Proctor, 1981), where layered convection can be triggered by very carefully selected finite-amplitude perturbations, even when the system is stable to infinitesimal ones. Preliminary simulations show that if a numerical experiment is initialized in an already-layered state it will remain layered indefinitely. This is true even if the system is fully stable ($R_0^{-1} > R_c^{-1}$) or simply stable to the layering γ-instability ($R_L^{-1} < R_0^{-1} < R_c^{-1}$). Whether Equations (2.7)-(2.12) are still valid for layered convection at $R_0^{-1} > R_L^{-1}$ remains to be determined. However, as we will discuss below, no compelling mechanism so far has been proposed to explain how these very specific kinds of layered initial conditions may naturally occur in stars of planets. Until such a mechanism is found, we argue that non-layered ODDC is likely to be far more prevalent at values of R_0^{-1} greater than the layering threshold R_L^{-1}.

There are several other conditions under which our model (Equations (2.7)-(2.12)) cannot be expected to hold. For example, in the presence of strong rotation, the above prescriptions will probably not apply (Blies et al., 2014). Rotation is known to inhibit regular overturning convection, and preliminary results indicate that strong rotation suppresses transport of both temperature and composition in ODDC as well. A more in depth discussion of the effects of rotation will be the subject of a future paper. Magnetic fields could clearly also affect our results.

2.5.3 Implications for astrophysical modeling

The implication of our findings from this paper for planetary modeling is that non-layered ODDC leads to fluxes that are not significantly larger than thermal conduction or molecular diffusion. Consequently, it is not sufficient simply to know if regions in the interior of a giant planet are unstable to ODDC. The fact that layered and non-layered ODDC lead to very different transport characteristics means that special attention must be paid to calculating the threshold R_{L}^{-1}, to determine which type of behavior will manifest.

The dynamics of non-layered ODDC is not expected to be pertinent to intermediate mass main sequence stars where most semi-convective regions likely have values of R_0^{-1} that are in the layered regime (Moore & Garaud, 2015). However, it may be important in more massive stars that have standalone semiconvective zones, i.e. regions unstable to ODDC that are well-separated from convective zones, and in giant planets, where higher values of Pr (compared to stars) indicate a smaller range of R_0^{-1} that is unstable to ODDC, and a lower layering threshold, R_{L}^{-1}.

In particular, the near-zero luminosity of Uranus suggests that thermal transport through the planet's interior is inefficient (Hubbard et al., 1995). Advances in equation of state research (Redmer et al., 2011) lend credence to the idea that convection is being inhibited by steep compositional gradients. If this is the case, the inefficient gravity wave-dominated ODDC discussed in this paper may potentially play a role in Uranus's thermal evolution.

Also, though it is not yet known whether this phenomenon could produce observable signatures, the intermittent growth of shear layers discussed in this work is a potentially significant feature of non-layered ODDC in the deep interiors of giant planets. Indeed, in contrast to our simulations where there is a symmetry between the x and y directions, global rotation may provide a preferred direction for shearing motions, which could induce large scale azimuthal flows.

2.5.4 Discussion of prior studies

In this series of papers we have proposed a new prescription for transport due to ODDC in both its layered and non-layered forms based on an analysis of a comprehensive suite of numerical experiments. We now compare our complete model summarized in Section 2.5.1 with existing work in the astrophysical literature. Typically, prior studies on this topic have only addressed either the layered or non-layered form of double-diffusive convection, being unaware, perhaps, that both regimes may in fact occur. Langer et al. (1983), for example, derived an expression for the effective diffusivity of composition through stellar semi-convective regions without invoking thermo-compositional layers. They proposed that,

$$D_\mu = \frac{\alpha \kappa_T}{6} \frac{\nabla - \nabla_{\rm ad}}{\nabla_{\rm ad} + \frac{\beta}{4-3\beta}\nabla_\mu - \nabla} \, , \tag{2.13}$$

where, in this case, α is an efficiency factor. By contrast, the majority of other studies have assumed that double-diffusive regions are always layered. Stevenson (1982), who was the first to import this notion to the astrophysical context, proposed a relationship between thermal and compositional transport in double-diffusive regions in Jupiter and Saturn,

$$F_\mu \sim \tau^{\frac{1}{2}} F_T \, . \tag{2.14}$$

This kind of law naturally arises when assuming that the fluxes are limited to diffusive transport through thin, stably stratified interfaces (see Linden & Shirtcliffe, 1978, and below). Later, Spruit (1992) also developed a parametrization for transport through layers separated by stable interfaces of this kind, and proposed that the thermal Nusselt number and compositional diffusivity scale as

$$\begin{aligned} \mathrm{Nu}_T &\sim (\mathrm{Pr}\mathrm{Ra}_T)^{\frac{1}{4}} \quad , \\ D_\mu &\sim (\kappa_\mu \kappa_T)^{\frac{1}{2}} \left(\frac{4}{\beta} - 3\right) \frac{\nabla_r - \nabla_{\mathrm{ad}}}{\nabla_\mu} \, , \end{aligned} \tag{2.15}$$

where ∇_r is the radiative gradient. More recently, works by Spruit (2013) and Zaussinger & Spruit (2013) have revised this model to account for the theoretically expected, and experimentally observed, $\frac{4}{3}$ flux law that Spruit's original model did not satisfy. Also, recently Leconte & Chabrier (2012) have developed a formalism for determining the transport of heat and chemical composition in a giant planetary interior composed of convective thermo-compositional layers. With their formalism, which is similar to that of mixing length theory, they calculate the number of layers that compose a giant planetary interior, assuming, as in previous studies, that the interfaces between the layers are diffusive.

As we have shown in this paper, however, layers do not always necessarily form. The specious notion pervading recent astrophysical models that double-diffusive regions must *always* take the form of layers separated by thin, diffusive interfaces likely stems historically from earlier experimental work on double-diffusive convection in the geophysical context. In geophysical fluids, where $\mathrm{Pr} \sim 1$, the range of R_0^{-1} that is unstable to infinitesimal perturbations (see Equation 1.9) is very small ($R_c^{-1} = 1.14$ for $\mathrm{Pr} = 7$ and $\tau = 0.01$, and the layering threshold, R_L^{-1}, presumably lies between 1 and 1.14, if it even exists). Meanwhile, double-diffusive layering is observed fairly frequently in volcanic lakes and in the arctic ocean, and the mean temperature and compositional gradients through these staircases have corresponding density ratios well in excess of R_c^{-1} (ie. the linearly stable regime). While the necessary finite-amplitude mechanism by which these staircases form in this case remain to be determined even to date, such a mechanism must clearly exist in the geophysical case since the layers are observed. Laboratory experiments to study double-diffusive layers at high Pr therefore nearly always start with layers already present and merely focus on measuring the fluxes through the staircase.

Turner (1965) was the first to conduct laboratory experiments of thermo-compositional double-diffusive convection in such a layered regime. In those experiments a layer of cold, low salinity, water was deposited carefully on top of a layer of high salinity water that was then heated from below. The fluxes of temperature and salt across the sharp interface were then measured. In that study, the following prescription was proposed for the fluxes across the interface,

$$\begin{aligned} F_T &\propto (\Delta T)^{\frac{4}{3}} \quad , \\ F_S &\propto (\Delta S)^{\frac{4}{3}} \ , \end{aligned} \tag{2.16}$$

where ΔT and ΔS are the temperature and salinity differences between the two layers. As discussed earlier, these scaling laws can be derived from simple dimensional arguments (see Section 2.5.2). Later, Shirtcliffe (1973) conducted similar laboratory experiments of double-diffusive convection where the diffusive quantities were sugar and salt dissolved in water. Linden & Shirtcliffe (1978) then used Shirtcliffe's results to develop the prescription for the relationship between the thermal and compositional fluxes that Stevenson (1982) later applied to the astrophysical case (see Equation 2.14), and which is also at the heart of the models presented by Spruit (1992, 2013).

Given that geophysical and astrophysical double diffusive convection are governed by the same basic equations, and without the help of numerical simulations at low Pr, it was natural for Stevenson (1982) and Spruit (1992) to extrapolate from the results of geophysical experiments to draw conclusions about astrophysical systems. This is, in fact, what led them to assume that astrophysical double-diffusive convection takes the form of stacked convective layers separated by thin, quiescent interfaces. However, with the help of modern numerical simulations, and thanks to the work presented in this series of papers, we have now established that such an extrapolation results from geophysical double-diffusive convection to the astrophysical parameter regime is not only inadvisable, but in many cases incorrect.

It is crucial to remember that, by contrast to the geophysical case, in giant planets Pr $\sim \tau \sim 10^{-2} - 10^{-3}$, and $R_c^{-1} \simeq 10 - 100$, meaning that there is a much wider range of R_0^{-1} for which infinitesimal perturbations may trigger ODDC. In fact, R_c^{-1} is so large that in order to achieve $R_0^{-1} > R_c^{-1}$ requires, in many cases, an unphysically large compositional gradient. In other words, unlike the Earth's oceans and lakes, it is likely that the linear instability is a ubiquitous feature of double-diffusive regions in stars and planet. Far from being merely in intellectual distinction, the way in which the instability is excited has two important effects on the dynamics of double-diffusive systems in both the layered and non-layered parameter regimes.

First, in ODDC when $1 < R_0^{-1} < R_L^{-1}$, the layers that spontaneously form are fundamentally different from the layers observed in geophysics. In laboratory experiments done at geophysical parameters (where finite-amplitude perturbations are necessary to initiate layered thermo-compositional convection) (Noguchi & Niino, 2010; Carpenter et al., 2012), layers appear to persist indefinitely, and the layer interfaces are quiescent, and diffusive. By contrast, in the layered simulations presented in this series of papers, the interfaces between layers are dynamic and turbulent, and the layers tend to merge until a single one remains in the domain. More than being merely a qualitative difference, the different character of the layers in each context leads to significant quantitative differences in thermal and compositional transport. In particular, Wood et al. (2013) found that contrary to Equation (2.14) proposed by Stevenson (1982) and used by Spruit (1992, 2013), $\gamma_{\rm tot}^{-1}$ is not proportional to $\tau^{\frac{1}{2}}$ in systems where layers form spontaneously.

Second, the non-layered ODDC regime is never observed in geophysical experiments, which is not surprising as (1) the range of parameters for which it could theoretically be observed is tiny, and (2) most experiments are initialized with layers in the first place. By contrast, non-layered ODDC is found so far to be ubiquitous in astrophysical simulations initialized with infinitesimal perturbations for $R_L^{-1} < R_0^{-1} < R_c^{-1}$. While it is possible that finite-amplitude layering may naturally occur in astrophysics, no separate layering mechanism has yet been proposed to suggest that these finite amplitude instabilities would be as commonplace in astrophysics as the linear instability is likely to be. Until such a mechanism is found it is therefore preferable to focus on the dynamics of ODDC that naturally develop from random infinitesimal perturbations, rather than artificially imposed initial conditions consisting of layers of unspecified origin. Nevertheless, the behavior of high-density ratio layered ODDC at astrophysical parameters is an interesting problem that deserves further study, and will therefore be the topic of a future paper.

Chapter 3

Rotating ODDC

The following chapter is composed of the main text of work submitted to The Astrophysical Journal in August of 2016. The co-author of this work is Pascale Garaud, professor of applied mathematics at the University of California at Santa Cruz.

3.1 Introduction

In the previous Chapters, we investigated the simplest possible model of ODDC in which the only body force considered was gravity. It is natural to wonder how additional physical mechanisms may affect the long term dynamics of ODDC. Global rotation is one such mechanism that is particularly relevant to the gas giant planets in our own solar system due to their rapid rotation periods (~ 9.9 hours for Jupiter and ~ 10.7 hours for Saturn). It is also potentially important to rapidly rotating extra-solar giant planets, and massive stars. There have been some recent studies of rotating layered convection in double-diffusive fluids, but only for the geophysical parameter regime (Carpenter & Timmermans, 2014) in conditions that are not unstable to ODDC (or to the $\gamma-$instability).

In this work we study the effect of global rotation on the linear stability properties and long-term dynamics associated with ODDC. In Section 3.2 we introduce our mathematical model and in Section 3.3 we study how rotation affects its linear stability properties. We analyze the impact of Coriolis forces on the formation of thermo-compositional layers in Section 3.4 by studying a suite of simulations with parameter values selected to induce layer formation in non-rotating ODDC. In Section 3.5 we show results from two other sets of simulations at different values of the diffusivities and of the background stratification and study how rotation affects the dynamics of the non-layered phase of ODDC. In Section 3.6 we study the effect of colatitude on layer formation. Finally, in Section 3.7 we discuss our results and present preliminary conclusions.

3.2 Mathematical Model

The basic model assumptions for rotating ODDC are similar to those made in previous studies of the non-rotating systems (Rosenblum et al., 2011; Mirouh et al., 2012; Wood et al., 2013; Moll et al., 2016). As in previous work, we consider a domain that is significantly smaller than a density scale height, and where flow speeds are significantly smaller than the sound speed of the medium. This allows us to use the Boussinesq approximation (Spiegel & Veronis, 1960) and to ignore the effects of curvature. We consider a 3D Cartesian domain centered at radius $r = r_0$, and oriented in such a way that the z-axis is in the radial direction, the x-axis is aligned with the azimuthal direction, and the y-axis is aligned with the meridional direction. We also assume constant background gradients of temperature, T_{0z}, and chemical composition, μ_{0z}, over the vertical extent of the box, which are defined as follows:

$$
\begin{aligned}
T_{0z} &= \frac{\partial T}{\partial r} = \frac{T}{p}\frac{\partial p}{\partial r}\nabla \, , \\
\mu_{0z} &= \frac{\partial \mu}{\partial r} = \frac{\mu}{p}\frac{\partial p}{\partial r}\nabla_{\mu} \, ,
\end{aligned}
\tag{3.1}
$$

where all the quantities are taken at $r = r_0$. Here, p denotes pressure, T is temperature, μ is the mean molecular weight, and ∇ and ∇_μ have their usual astrophysical definitions:

$$
\nabla = \frac{d \ln T}{d \ln p} \, , \, \nabla_\mu = \frac{d \ln \mu}{d \ln p} \text{ at } r = r_0 \, . \tag{3.2}
$$

We use a linearized equation of state in which perturbations to the background density profile, $\tilde{\rho}$, are given by

$$
\frac{\tilde{\rho}}{\rho_0} = -\alpha \tilde{T} + \beta \tilde{\mu} \, , \tag{3.3}
$$

where $\tilde{T}$, and $\tilde{\mu}$ are perturbations to the background profiles of temperature and chemical composition, respectively, and ρ_0 is the mean density of the domain. The coefficient of thermal expansion, α, and of compositional contraction, β, are defined as

$$
\begin{aligned}
\alpha &= -\frac{1}{\rho_0}\left.\frac{\partial \rho}{\partial T}\right|_{p,\mu} \, , \\
\beta &= \frac{1}{\rho_0}\left.\frac{\partial \rho}{\partial \mu}\right|_{p,T} \, .
\end{aligned}
\tag{3.4}
$$

We take the effect of rotation into account by assuming that the rotation vector is given by:

$$
\mathbf{\Omega} = |\mathbf{\Omega}| \left(0, \sin\theta, \cos\theta\right) \, , \tag{3.5}
$$

where θ is the angle between the rotation axis and the $z-$axis. With this assumed rotation vector, a domain placed at the poles has a rotation axis aligned with the z-direction ($\theta = 0$), while at the equator the rotation axis is in the y-direction ($\theta = \frac{\pi}{2}$). Due the small sizes of the domains considered (compared to a stellar or planetary radius) we use an f-plane approximation where rotation is assumed to be constant throughout the domain.

In what follows we use new units for length, $[l]$, time, $[t]$, temperature, $[T]$, and chemical composition, $[\mu]$ as,

$$\begin{aligned}
[l] &= d = \left(\frac{\kappa_T \nu}{\alpha g \left| T_{0z} - T_{0z}^{\rm ad} \right|} \right)^{\frac{1}{4}} = \left(\frac{\kappa_T \nu}{\alpha g \frac{T}{p} \left| \frac{\partial p}{\partial r} \right| \left| \nabla - \nabla_{\rm ad} \right|} \right)^{\frac{1}{4}} , \\
[t] &= \frac{d^2}{\kappa_T} , \\
[T] &= d \left| T_{0z} - T_{0z}^{\rm ad} \right| , \\
[\mu] &= \frac{\alpha}{\beta} d \left| T_{0z} - T_{0z}^{\rm ad} \right| , \qquad (3.6)
\end{aligned}$$

where g is the local gravitational acceleration, ν is the local viscosity, κ_T is the local thermal diffusivity, and where $T_{0z}^{\rm ad}$ is the adiabatic temperature gradient defined as

$$T_{0z}^{\rm ad} = \frac{T}{p} \frac{dp}{dr} \nabla_{\rm ad} \text{ at } r = r_0 \, . \qquad (3.7)$$

The non-dimensional governing equations for rotating ODDC are then given by

$$\begin{aligned}
\nabla \cdot \mathbf{u} &= 0 , \\
\frac{\partial \mathbf{u}}{\partial t} + \mathbf{u} \cdot \nabla \mathbf{u} &= -{\rm Pr} \nabla \tilde{p} + {\rm Pr} \left(\tilde{T} - \tilde{\mu} \right) \hat{\mathbf{e}}_z + {\rm Pr} \nabla^2 \mathbf{u} - \sqrt{{\rm Ta}^*} \left(\frac{\boldsymbol{\Omega}}{|\boldsymbol{\Omega}|} \times \mathbf{u} \right) , \\
\frac{\partial \tilde{T}}{\partial t} + \mathbf{u} \cdot \nabla \tilde{T} - w &= \nabla^2 \tilde{T} , \\
\frac{\partial \tilde{\mu}}{\partial t} + \mathbf{u} \cdot \nabla \tilde{\mu} - R_0^{-1} w &= \tau \nabla^2 \tilde{\mu} , \qquad (3.8)
\end{aligned}$$

where $\mathbf{u} = (u, v, w)$ is the velocity field. This introduces the usual non-dimensional diffusion parameters Pr (the Prandtl number) and τ (the diffusivity ratio) as

$$\mathrm{Pr} = \frac{\nu}{\kappa_T}\,,\ \tau = \frac{\kappa_\mu}{\kappa_T}\,, \tag{3.9}$$

where κ_μ is the compositional diffusivity, and the inverse density ratio, R_0^{-1}, as

$$R_0^{-1} = \frac{\beta\,|\mu_{0z}|}{\alpha\,|T_{0z} - T_{0z}^{\mathrm{ad}}|}\,. \tag{3.10}$$

In a non-rotating model Pr, τ and R_0^{-1} are sufficient to fully describe the system. In a rotating model though, we must introduce a fourth non-dimensional parameter that controls the strength of rotation,

$$\mathrm{Ta}^* = \frac{4\,|\mathbf{\Omega}|^2\,d^4}{\kappa_T^2}\,, \tag{3.11}$$

which is related to the commonly defined Taylor number in studies of rotating Rayleigh-Bénard convection as:

$$\mathrm{Ta} = \frac{4\,|\mathbf{\Omega}|^2\,L_z^4}{\nu^2} = \mathrm{Pr}^{-2}\left(\frac{L_z}{d}\right)^4 \mathrm{Ta}^*\,. \tag{3.12}$$

Values of Ta* and d in a stellar or planetary interior are difficult to estimate due to uncertainty in the superadiabaticity of double-diffusive regions. However we can make reasonable estimates for their upper and lower bounds. As in Nettelmann et al. (2015) we define the superadiabaticity, ΔT_{0z}, as

$$\Delta T_{0z} = \frac{\nabla - \nabla_{\mathrm{ad}}}{\nabla_{\mathrm{ad}}} = \frac{T_{0z} - T_{0z}^{\mathrm{ad}}}{T_{0z}^{\mathrm{ad}}}\,. \tag{3.13}$$

In their study values of ΔT_{0z} were typically between 10^{-2} and 10^{2} (see their Figure

2). This range of values, combined with data from French et al. (2012), allows us to calculate d and Ta* as a function of depth for the interior of Jupiter. From Figure 3.1 we see that the lowest estimates for Ta* are on the order of 10^{-3} (for large ΔT_{0z}) and the upper bound is between 1 and 10 (for small ΔT_{0z}). As we will show later, this range includes values of Ta* which indicate significant rotational effects on the dynamics of ODDC. Larger values of ΔT_{0z} are expected in the case of layered ODDC, where T_{0z} is close to T_{0z}^{ad}, while smaller values are expected in the case of non-layered ODDC, where T_{0z} is closer to the radiative temperature gradient.

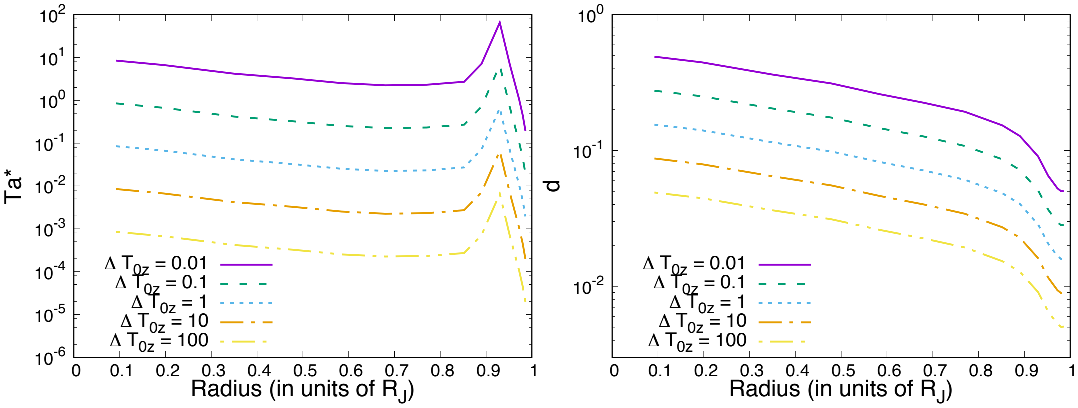

Figure 3.1: Values of Ta* (left) and d (right) estimated for the interior jupiter using data from French et al. (2012). Estimates are made for various values of ΔT_{0z} between 10^{-2} and 10^{2}.

The conditions for ODDC to occur in a non-rotating fluid are defined by Pr, τ, and, most importantly, R_0^{-1} (Baines & Gill, 1969). For a system to be unstable to infinitesimal perturbations, R_0^{-1} must be within the following range:

$$1 < R_0^{-1} < R_c^{-1} \equiv \frac{\mathrm{Pr} + 1}{\mathrm{Pr} + \tau} \, . \tag{3.14}$$

If $R_0^{-1} < 1$, the system is unstable to standard convection, and if $R_0^{-1} > R_c^{-1}$ the system is linearly stable. It should be noted that while a fluid with $R_0^{-1} > R_c^{-1}$

may be linearly stable, it is still possible for an instability to be triggered through finite amplitude perturbations (assuming that the perturbations are of the right functional form, see Huppert & Moore, 1976; Proctor, 1981). When we discuss ODDC, however, we are referring only to the linearly unstable kind of double-diffusive convection.

3.3 Linear stability analysis

We analyze the linear stability of rotating double-diffusive convection by first linearizing the governing equations in (3.8) around $\tilde{T} = \tilde{\mu} = \mathbf{u} = 0$. We then assume that the functional form of the perturbations is

$$\{\mathbf{u}, \tilde{T}, \tilde{\mu}\} = \{\hat{\mathbf{u}}, \hat{T}, \hat{\mu}\} \exp\left(ilx + imy + ikz + \lambda t\right) , \tag{3.15}$$

where the hatted quantities are the mode amplitudes, and where l, m, and k are the wave numbers for the x, y, and z directions, respectively. By assuming solutions of this form, we get the following dispersion relation:

$$\begin{aligned} &\left(\lambda + \mathrm{Pr}K^2\right)^2 \left(\lambda + \tau K^2\right)\left(\lambda + K^2\right) \\ -\frac{K_H^2}{K^2}\mathrm{Pr}&\left(\lambda + \mathrm{Pr}K^2\right)\left[\left(\lambda + \tau K^2\right) - R_0^{-1}\left(\lambda + K^2\right)\right] \\ -\mathrm{Ta}^*&\frac{\left(m\sin\theta + k\cos\theta\right)^2}{K^2}\left(\lambda + \tau K^2\right)\left(\lambda + K^2\right) \quad = 0\,, \end{aligned} \tag{3.16}$$

where $K = \sqrt{l^2 + m^2 + k^2}$ and K_H is the magnitude of the horizontal wavenumber defined as $K_H = \sqrt{l^2 + m^2}$.

As in non-rotating ODDC, it can be shown that the fastest growing linear modes in the rotating case have purely vertical fluid motions which span the height of the domain (ie. $k = 0$). In fact, in Equation (3.16) we see that when

$\theta = 0$ and $k = 0$ the rotation-dependent term drops out altogether. The fastest growing modes in rotating systems with $\theta = 0$ are therefore identical to their non-rotating counterparts both in horizontal wavenumber and growth rate.

However, when $\theta = 0$ rotation does affect the growth of other modes which have $k \neq 0$, and always acts to reduce their growth rates. This is illustrated in Figure 3.2 which shows mode growth rates as a function of k and K_H for various values of Ta*. In this "polar" configuration, the mode growth rate only depends on the total horizontal wavenumber K_H, and not on l or m individually. As rotation increases we see that modes with $k \neq 0$ grow more slowly or become stable, while only modes with very low k or $k = 0$ remain unstable.

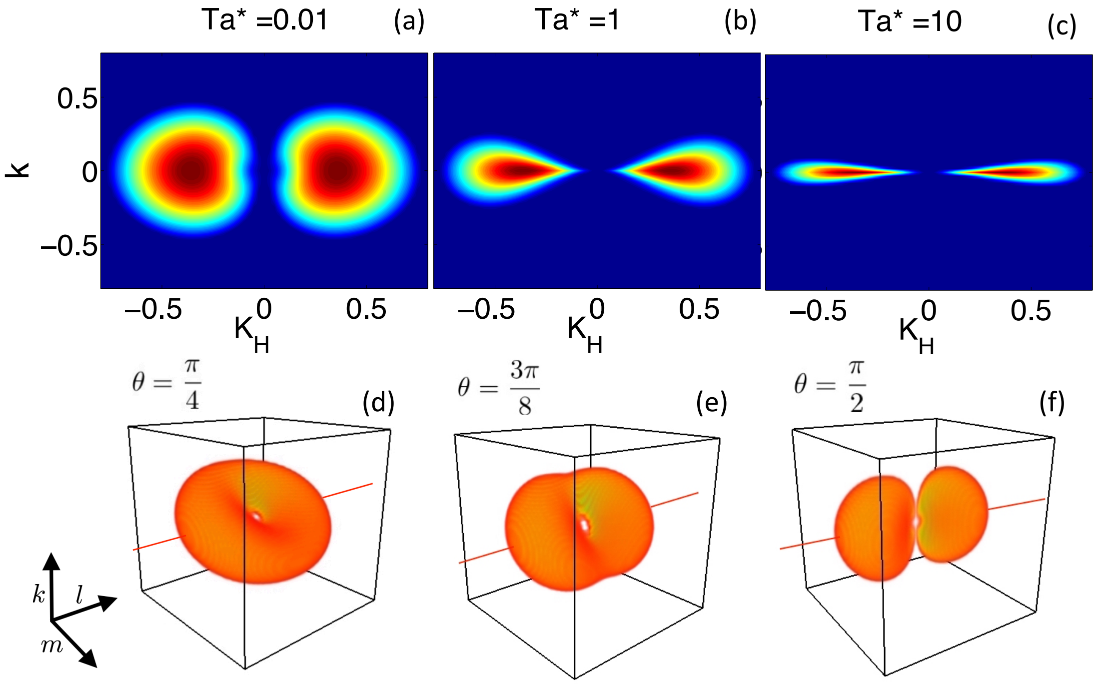

Figure 3.2: In each of the panels, Pr $= \tau = 0.1$, $R_0^{-1} = 1.25$. Panels (a-c): Growth rates versus horizontal and vertical wave numbers for stated values of Ta* with $\theta = 0$. Panels (d-f): Surface of null growth rate for Ta* $= 1$ and stated values of θ. The line shows the axis of l wavenumbers. All points on this axis are unaffected by rotation, including the fastest-growing modes.

When $\theta \neq 0$ the fastest growing modes still have $k = 0$. However, to avoid the attenuating effect of rotation on their growth rates, they must satisfy the additional constraint,

$$m \sin\theta = -k \cos\theta \,. \tag{3.17}$$

Consequently, the fastest growing modes must have both $m = 0$ and $k = 0$. Because of this extra constraint, there are fewer modes that grow at the fastest rate. This is well illustrated in Figure 3.2 where we see that in rotating ODDC there is a ring of modes that are unaffected by rotation that is inclined at an angle of θ. When $\theta \neq 0$, this ring intersects the $k = 0$ plane at only two points meaning that there are only two fastest growing modes whose growth rates are not diminished by the effects of rotation. These unaffected fastest growing modes take the form of invariant vertically oscillating planes, spanned by the direction of gravity and the rotation axis (see Section 3.6 for more details on this limit).

3.4 Simulations with $\theta = 0$

Reproducing the conditions of stellar or planetary interiors in laboratory experiments is practically impossible, so in order to understand the development of rotating ODDC beyond linear theory, we must study results from direct numerical simulations (DNS). In this section we analyze data from 3D numerical simulations run using a version of the pseudo-spectral, triply periodic, PADDI Code (Traxler et al., 2011), which has been modified to take into account the effects of rotation. Each simulation is run with $\mathrm{Pr} = \tau = 0.1$, $R_0^{-1} = 1.25$. We have chosen these values because non-rotating simulations at these parameters have been found to spontaneously form layers (as predicted by γ-instability theory, see Mirouh et al., 2012) which allows us to evaluate how global rotation affects the formation and evolution of these layers. We focus on 5 simulations with $\mathrm{Ta}^* = 0, 0.01, 0.1, 1$

and 10. Based on their qualitative behavior, we consider the simulations with Ta* = 0.01, and 0.1 to be “low Ta*" and the simulations with Ta* = 1 and 10 to be “high Ta*". Each has an effective resolution of 384^3 mesh points and the simulation domains have dimensions of $(100d)^3$. The simulations are initialized with random infinitesimal perturbations to the temperature field.

When studying the behavior of rotating ODDC using DNS, the quantities of greatest relevance to astrophysical models are the vertical fluxes of temperature and chemical composition through the domain. We express these fluxes in terms of thermal and compositional Nusselt numbers, Nu_T and Nu_μ, which are measures of total fluxes (turbulent + diffusive) in units of the diffusive flux. Using the non-dimensionalization described in Section 3.2, Nu_T and Nu_μ are expressed as

$$\begin{aligned} \mathrm{Nu}_T &= 1 + \langle \tilde{w}\tilde{T} \rangle \,, && (3.18) \\ \mathrm{Nu}_\mu &= 1 + \tfrac{\langle \tilde{w}\tilde{\mu} \rangle}{\tau R_0^{-1}} \,. && (3.19) \end{aligned}$$

In practice, we are most interested in the capacity of ODDC to induce vertical turbulent mixing. We therefore quantify transport in terms of the non-dimensional turbulent flux of temperature, $\mathrm{Nu}_T - 1$, and the non-dimensional turbulent flux of chemical species, $\mathrm{Nu}_\mu - 1$. These quantities can also be viewed as the ratio of turbulent diffusivity to the microscopic diffusivity for each transported quantity.

We also note that for astrophysical objects it is usually possible to estimate the heat flux by observing the intrinsic luminosity, but direct measurements of the compositional flux are more difficult to obtain. However, the rate of compositional transport may be inferred through observations of the heat flux if a set relationship exists between them. For this reason we also express our results in terms of the total inverse flux ratio, $\gamma_{\rm tot}^{-1}$, given (non-dimensionally) by

$$\gamma_{\rm tot}^{-1} = \tau R_0^{-1} \frac{\rm Nu_\mu}{\rm Nu_{\it T}} \,. \tag{3.20}$$

This is the the ratio of the total buoyancy flux due to compositional transport, to the total buoyancy flux due to heat transport, which was first discussed by Stevenson & Salpeter (1977). This ratio is typically smaller than one when dominated by turbulent mixing, and describes what fraction of the total energy flux can be used to mix high-μ chemical species upwards. The inverse flux ratio is also a crucial player in the $\gamma-$instability theory: indeed, as shown by Mirouh et al. (2012), a necessary and apparently sufficient condition for layer formation in ODDC is that $\gamma_{\rm tot}^{-1}$ be a decreasing function of R_0^{-1}. Furthermore, $d\gamma_{\rm tot}^{-1}/dR_0^{-1}$ controls the growth rate of layering modes.

Finally, measuring how the relative influence of rotation changes as rotating simulations evolve offers insight into how our results may scale to larger systems. We measure the influence of rotation with a Rossby number (the ratio of the inertial force to the Coriolis force), which is usually defined as a turbulent velocity divided by the product of a length scale and the rotation rate. Here, we define the Rossby number as

$$\mathrm{Ro} = \frac{u_{\rm h,rms}}{2\pi L_h \sqrt{\mathrm{Ta}^*}} \,, \tag{3.21}$$

where $u_{\rm h,rms}$ is the rms horizontal velocity, and L_h is the expectation value of the horizontal length scale of turbulent eddies over the power spectrum, defined as

$$L_h = \frac{\sum_{l,m,k} \frac{\left(|\hat{u}_{lmk}|^2 + |\hat{v}_{lmk}|^2\right)}{\sqrt{l^2+m^2}}}{\sum_{l,m,k}\left(|\hat{u}_{lmk}|^2 + |\hat{v}_{lmk}|^2\right)} \,, \tag{3.22}$$

where $\hat{u}_{lmk}$ and $\hat{v}_{lmk}$ are the amplitudes of the Fourier modes of u and v, respectively, with wavenumber (l, m, k). We define Ro this way because in systems where $\theta = 0$, only horizontal velocity components are affected by rotation.

3.4.1 Growth and saturation of the linear instability

Figure 3.3 shows the turbulent compositional flux as a function of time for each of the simulations with $\mathrm{Pr} = \tau = 0.1$, and $R_0^{-1} = 1.25$, focusing on the growth and saturation of basic instability of ODDC. It clearly shows that the growth of the linear instability in simulations of rotating ODDC (with $\theta = 0$) behaves similarly to the non-rotating case. This is not surprising since the overall growth of the linear instability is dominated by the fastest growing modes, which in this case are completely unaffected by rotation (see Section 3.3).

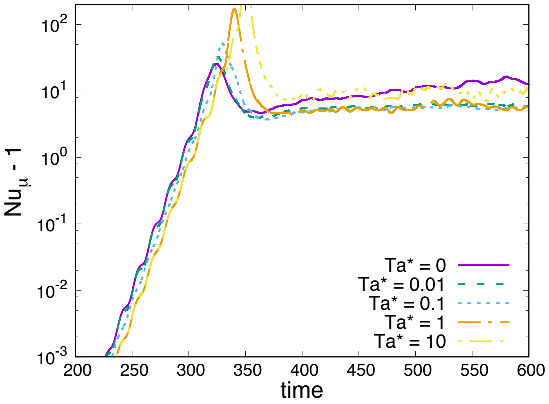

Figure 3.3: Exponential growth and early stages of the non-linear saturation of the turbulent compositional flux for simulations with $\mathrm{Pr} = \tau = 0.1$, $R_0^{-1} = 1.25$, $\theta = 0$ and stated values of Ta^*. The growth rates are independent of Ta^*. The fluxes immediately after non-linear saturation are also more-or-less independent of Ta^*, except for the case with $\mathrm{Ta}^* = 10$.

After the initial growth of the linear instability, each simulation reaches a non-linear saturation (at around $t = 300$ in each case) and becomes homogeneously turbulent. Figure 3.3 shows that the compositional flux in the homogeneously turbulent phase are roughly independent of Ta^* at low Ta^*. For $\mathrm{Ta}^* = 0.01, 0.1$

and 1 the mean fluxes during this phase are statistically similar to one another, while the most rapidly rotating simulation ($\mathrm{Ta}^* = 10$) reaches a plateau that is slightly higher than the others. Note that the composition flux in the non-rotating simulation ($\mathrm{Ta}^* = 0$) behaves differently, because in this case layers begin to form almost immediately after saturation. This causes it to continue to grow after saturation (albeit at a slower rate), never achieving a quasi-steady state as the rotating simulations do. We now look in more detail at the behavior of the low Ta* and high Ta* sets of simulations, respectively.

3.4.2 Low Ta^* simulations

Figure 3.4 shows that in low Ta^* simulations the homogeneously turbulent phase (where fluxes remain more or less statistically steady) is followed by a series of step-wise increases in the compositional (and thermal) flux, which are indicative of layers that form spontaneously through the γ-instability and then merge progressively over time. In each case, three layers initially form which then merge into two, and ultimately into a single layer with a single interface. This final configuration is statistically stationary. We therefore find the qualitative evolution of layers to be consistent with previous studies of non-rotating layered ODDC (Rosenblum et al., 2011; Wood et al., 2013). However, the progressive increase in rotation rate introduces quantitative differences between rotating and non-rotating cases, even at low Ta^*. The rotation rate clearly affects the time scales for layer formation and layer mergers, respectively, with stronger rotation leading to delays in both processes.

The formation of layers can be understood quantitatively by studying the growth of “layering modes" predicted by γ-instability theory (as in Stellmach et al., 2011; Rosenblum et al., 2011; Mirouh et al., 2012, for example). Each

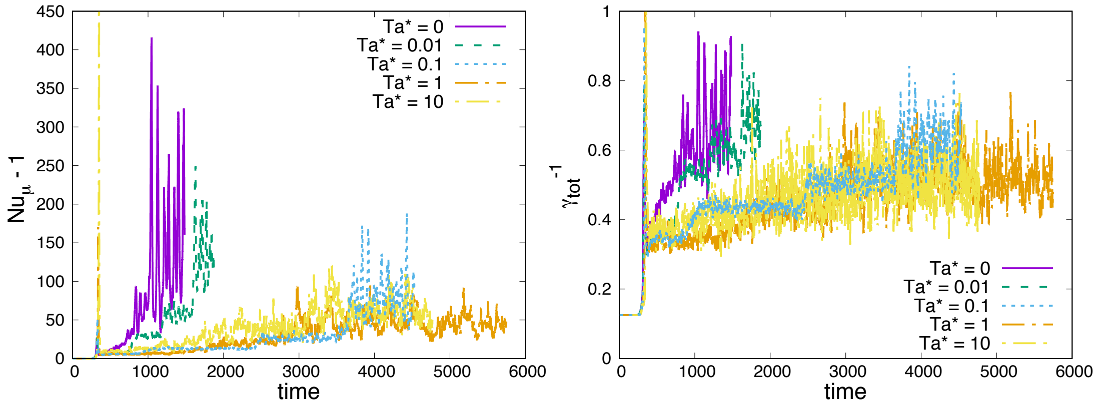

Figure 3.4: Long-term behavior of the turbulent compositional flux (left) and of γ_{tot}^{-1} (right) for stated values of Ta^*. In each simulation, $\text{Pr} = \tau = 0.1$, $R_0^{-1} = 1.25$, and $\theta = 0$. In low Ta^* simulations, the turbulent compositional flux increases in a stepwise manner indicative of layer formation, while in the high Ta^* cases there is no clear evidence for similar stepwise increases.

layering mode corresponds to a horizontally invariant, vertically sinusoidal perturbation to the background density profile. To analyze them, we therefore look at the amplitude of the Fourier modes of density perturbations with wave numbers $(0, 0, k_n)$, where $k_n = \frac{2\pi n}{L_z}$, where $L_z = 100d$ is the domain height, and n is the number of layers in the process of forming. The evolution of the $(0, 0, k_2)$ and $(0, 0, k_3)$ modes as a function of time for each of the three low Ta^* simulations is shown in Figure 3.5.

For simulations with $\text{Ta}^* = 0, 0.01$ and 0.1, $(0, 0, k_3)$ is the mode that initially grows to have the largest amplitude, which explains why the staircases first form with three layers. We see that, at low Ta^*, the $(0, 0, k_3)$ modes all initially grow at roughly the same rate. This is unsurprising, since rotation does not have a direct effect on the γ-instability because Coriolis terms only appear in the momentum equation in (3.8), which is ignored in the mean field theory upon which the γ-instability is based (Mirouh et al., 2012). Rotation could in principle have an indirect influence over layer formation by significantly affecting the turbulent

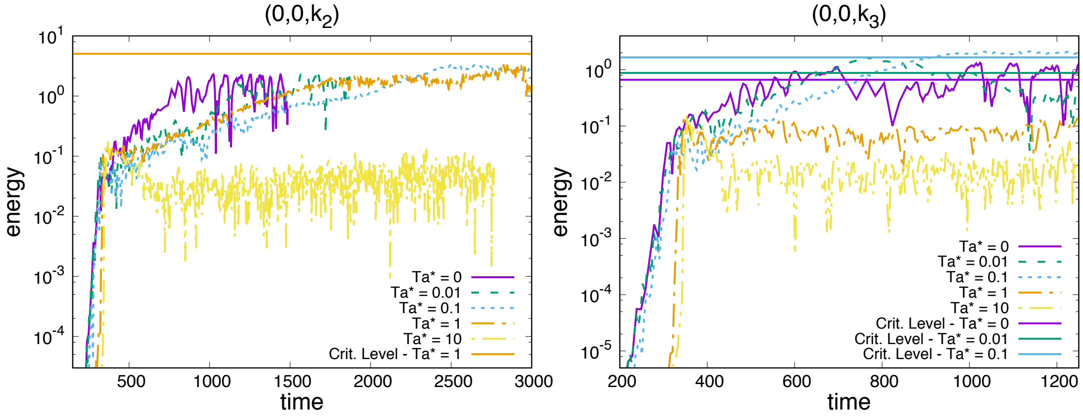

Figure 3.5: Time series of the amount of energy in layering modes $(0, 0, k_2)$ (left) and $(0, 0, k_3)$ (right) for simulations with $\mathrm{Pr} = \tau = 0.1$, $R_0^{-1} = 1.25$, and $\theta = 0$, for various values of Ta^*. Layering modes are horizontally invariant perturbations to the background profiles of temperature and chemical composition. Also shown are the theoretical amplitudes these layering modes must attain in order to trigger layered convection. Perturbation amplitudes in the low Ta^* regime attain this amplitude, but fall short in the $\mathrm{Ta}^* = 1$ simulation.

fluxes in the homogeneously turbulent phase and changing the relationship between $\gamma_{\mathrm{tot}}^{-1}$ and R_0^{-1}, but as we see in Figure 3.3 this is not the case in the low Ta^* regime.

To understand the delay in the formation of layers we must instead look at the amplitude that the density perturbations must achieve in order to trigger the onset of layered convection. Indeed, rotation is well-known to delay the onset of instability in the case of thermal convection between parallel plates (Chandrasekhar, 1961), so by analogy, we expect that the localized positive density gradients caused by the growth of layering modes must be larger to trigger convective overturning and cause the staircase to appear. In the Appendix, we estimate the critical density gradient needed to trigger convection in rotating Rayleigh-Bénard convection. Using this result, we then compute the amplitude the layering modes must achieve as a function of k_n and Ta^*, to be

$$|A_n| = \left| \frac{\frac{3\pi^4}{H_n^4}\left(\frac{H_n^4 \mathrm{Ta}^*}{2\mathrm{Pr}^2\pi^4}\right)^{\frac{2}{3}} + \frac{27\pi^4}{4H_n^4} + \left(R_0^{-1} - 1\right)}{2k_n} \right| . \tag{3.23}$$

where $H_h = L_z/n = 2\pi/k_n$ is the nondimensional layer height associated with the layering mode $(0, 0, k_n)$. This amplitude is shown in Figure 3.5 for each of the $(0, 0, k_3)$ modes in the low Ta^* simulations. Consistent with our idea, the layering modes stop growing shortly after achieving their respective critical amplitudes (except for the $\mathrm{Ta}^* = 1$ case, see Section 3.4.3). This indicates that layered convection has commenced, taking the form of turbulent convective plumes bounded by freely moving, stably stratified interfaces.

In each case the mode $(0, 0, k_3)$ is then overtaken by modes $(0, 0, k_2)$ and ultimately $(0, 0, k_1)$ (not shown here). These multi-layer phases are metastable in that they persist over many eddy-turnover times before merging. Snapshots of the 3, 2, and 1-layered phases for $\mathrm{Ta}^* = 0$ and $\mathrm{Ta}^* = 0.1$ are shown in Figure 3.6b and 3.7b.

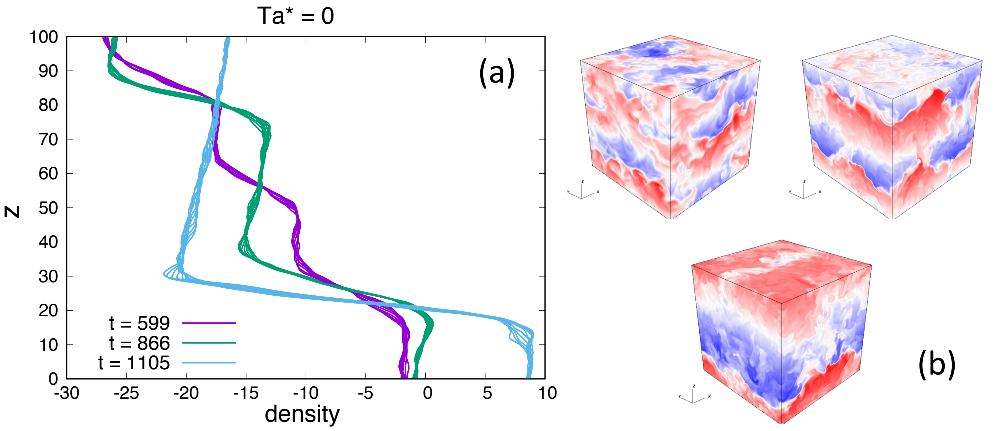

Figure 3.6: (a) Density profiles and (b) snapshots of the chemical composition field in the 3, 2, and 1 layered phases for a non-rotating simulation ($\mathrm{Ta}^* = 0$) with $\mathrm{Pr} = \tau = 0.1$ and $R_0^{-1} = 1.25$.

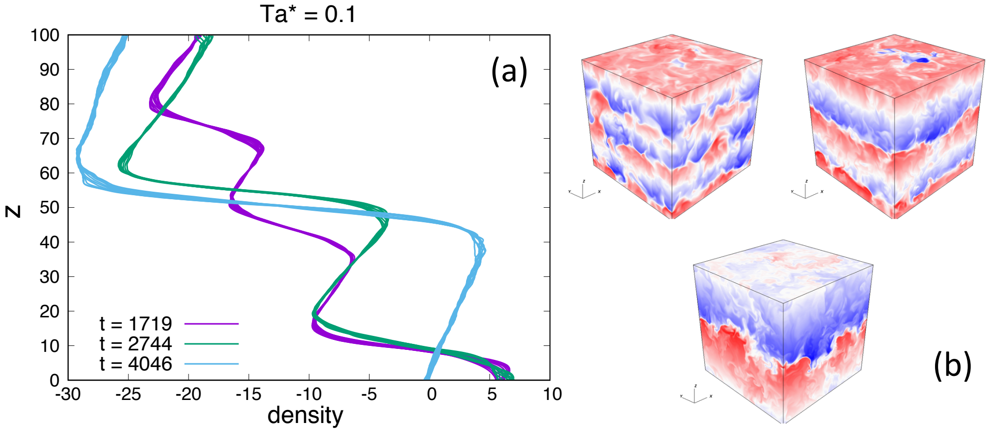

Figure 3.7: (a) Density profiles and (b) snapshots of the chemical composition field in the 3, 2, and 1 layered phases for a simulation with $\mathrm{Ta}^* = 0.1$, $\mathrm{Pr} = \tau = 0.1$, $R_0^{-1} = 1.25$ and $\theta = 0$. Noteworthy are the layer interfaces which are more stably stratified than in the non-rotating case. Also, there is a larger positive density gradient in the layers themselves.

Rotation also has a strong influence on several aspects of the dynamics of layered convection including the mean density profile within the layers, the stability of the interfaces, and, as mentioned earlier, the merger timescale. In Figures 3.6a and 3.7a, horizontally averaged density profiles show in greater detail the structure of the layers themselves in the three-, two-, and one-layered phases. Stronger rotation is correlated with larger positive density gradients in the layers themselves, which in turn necessarily leads to more stably stratified layer interfaces (at fixed R_0^{-1}).

The increase with rotation rate of the density gradients within the layers is similar to what occurs in rotating Rayleigh-Bénard convection (Julien et al., 1996). It is usually argued that turbulent buoyancy mixing by convection adjusts the mean density gradient (outside of any potential boundary layers) to a state of marginal stability. Combined with the fact that the critical density gradient for marginal stability increases with Ta^* (see Equation (3.23)), our results are not surprising. We see, however, that this effect is strongest for smaller layers and gradually decreases as the layers merge and their heights increase.

In Figure 3.4 we see that the simulation with $\mathrm{Ta}^* = 0.1$ spends a greater amount of time in the three- and two-layered phases than either of the other two simulations, and consequently takes about twice as long as the non-rotating run ($\mathrm{Ta}^* = 0$) to reach the one-layered phase. The root cause is related to the lower supercriticality of convection within the layers combined with the increased stability of the interfaces. Through inspection of the density profiles of our layered simulations, we see that the positions and shapes of the interfaces in rotating simulations have less variability with time compared with non-rotating simulations. We also see in Figure 3.4 that the fluxes in the rotating layered systems oscillate less than they do in the non-rotating ones. Wood et al. (2013) already discussed these large amplitude oscillations in non-rotating simulations and attributed them to the presence of large plumes of fluid punching through interfaces periodically causing spikes in transport. In our layered rotating simulations (particularly the $\mathrm{Ta}^* = 0.1$ case) the absence of large amplitude oscillations in the layered phase suggests that the motion of these plumes is inhibited, possibly because convection is weaker and the interfacial gradients are stronger. Since the plumes could be key players in the layer merger events, their suppression in the rotating simulations could also explain why the merger timescale is longer.

All of these effects also contribute to the reduction of mean fluxes of temperature and chemical composition through density staircases in rotating ODDC compared with the non-rotating case. To show this quantitatively, Table 1 presents measurements of $\mathrm{Nu}_T - 1$ and $\mathrm{Nu}_\mu - 1$ (with standard deviations) for each value of Ta^*. For low Ta^* simulations, which clearly form convective layers, the fluxes are measured in the one-layered phase. The simulation with $\mathrm{Ta}^* = 0.01$ shows 2% and 7% decreases in thermal and compositional fluxes, respectively, compared to

Ta^*	Ta	$\mathrm{Nu}_T - 1$	$\mathrm{Nu}_\mu - 1$	$\gamma_{\mathrm{tot}}^{-1}$
0	0	25.3 ± 10.8	149.8 ± 84.4	0.68 ± 0.12
0.01	1	24.5 ± 5.2	139.0 ± 37.5	0.68 ± 0.074
0.1	10	15.5 ± 4.0	82.9 ± 28.4	0.62 ± 0.067
1	100	10.2 ± 2.1	46.5 ± 12.4	0.52 ± 0.061
10	1000	14.4 ± 3.1	61.7 ± 14.7	0.51 ± 0.061
10 (narrow)	1000	44.0 ± 11.2	216.5 ± 58.9	0.62 ± 0.16

Table 3.1: Non-dimensional thermal and compositional fluxes through the domain in the ultimate statistically stationary state achieved by the simulation. In each case, $\mathrm{Pr} = \tau = 0.1$, $R_0^{-1} = 1.25$ and $\theta = 0$. For the cases with $\mathrm{Ta}^* = 0$, 0.01 and 0.1, these fluxes are measured in the 1-layered phase. For the cases with $\mathrm{Ta}^* = 1$ and 10, fluxes are measured once the system reaches a statistically steady state (see Figure 3.4).

the non-rotating simulation, while the $\mathrm{Ta}^* = 0.1$ simulation shows 38% and 44% reductions.

Wood et al. (2013) showed that fluxes in non-rotating layered ODDC follow a power law scaling which depends on the product of the Prandtl number and the thermal Rayleigh number based on the layer height. In our non-dimensionalization, the latter is defined as

$$\mathrm{Ra}_T = \frac{g\alpha \left| T_{0z} - T_{0z}^{\mathrm{ad}} \right| (Hd)^4}{\kappa_T \nu} = H^4 \,, \tag{3.24}$$

where H is the non-dimensional layer height. Figure 3.8 shows the mean non-dimensional turbulent compositional flux as a function of $\mathrm{Pr}\mathrm{Ra}_T$ for each of our low Ta^* simulations ($\mathrm{Ta}^* = 0$, 0.01, 0.1). To collect this data, average fluxes were computed in the 1, 2, and 3 layer phases of each simulation. We clearly see that rotation leads to reduced transport rates in layered convection. This is not entirely surprising because rotation is known to reduce the convective efficiency in Rayleigh-Bénard convection (Rossby, 1969). Bearing in mind the very limited amount of data available, we nevertheless attempt to fit it with flux laws of the

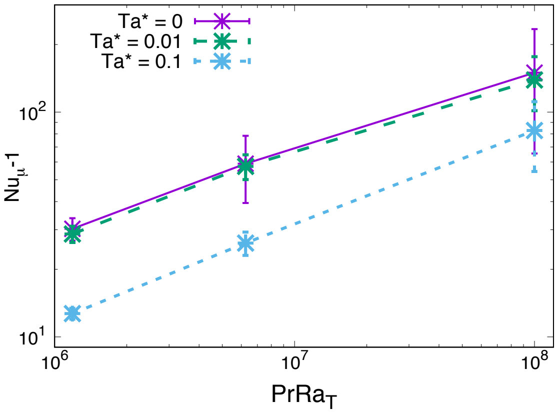

Figure 3.8: Non-dimensional compositional flux as a function of PrRa_T for low Ta^* simulations with $\mathrm{Pr} = \tau = 0.1$, $R_0^{-1} = 1.25$. In the $\mathrm{Ta}^* = 0.1$ simulations rotation acts to reduce the turbulent compositional flux in each layered phase. However roughly the same power law applies to all simulations.

form $\mathrm{Nu}_T - 1 = A(\mathrm{PrRa}_T)^a$ and $\mathrm{Nu}_\mu - 1 = B(\mathrm{PrRa}_T)^b$, using a nonlinear least square fit. The results are presented in Table 2.

We find that rotation affects the constants of proportionality (A and B), much more than it affects the exponent of PrRa_T (a and b). For $\mathrm{Ta}^* = 0.01$ rotation has a minimal effect on the fluxes in each layered phase and the relationship between flux and PrRa_T is the same as in the non-rotating case (Wood et al., 2013). For $\mathrm{Ta}^* = 0.1$ however, rotation reduces the coefficient A by almost a factor 5 and increases the exponent a by around 15%. There is evidence however that this change in the exponent may be due to the fact that the relative effect of rotation decreases for increasing values of PrRa_T. Indeed, Figure 3.9 shows an increase in Rossby number as layers merge in low Ta^* simulations (see Equation(3.21) for definition of Rossby number). This suggests that for sufficiently large layer heights rotational effects could become negligible and the flux law probably tends to the one found by Wood et al. (2013). This will need to be verified in simulations using larger computational domains.

		$\mathrm{Nu}_T - 1 = A(\mathrm{PrRa}_T)^a$		$\mathrm{Nu}_\mu - 1 = B(\mathrm{PrRa}_T)^b$	
Ta*	Ta	A	a	B	b
0	0	0.076	0.32	0.21	0.36
0.01	1	0.071	0.32	0.22	0.35
0.1	10	0.016	0.37	0.035	0.42

Table 3.2: Best fits for data presented in Figure 3.8.

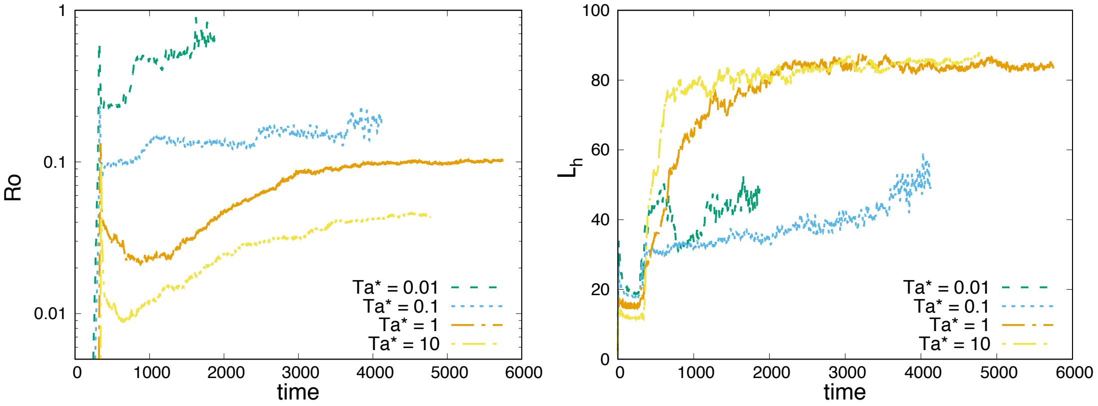

Figure 3.9: Rossby number Ro (left) and average horizontal lengthscale of turbulent eddies L_h (right) for simulations with $\mathrm{Pr} = \tau = 0.1$, $R_0^{-1} = 1.25$ and $\theta = 0$, for various values of Ta*. Noteworthy is that Ro increases as layers merge in the low Ta* regime suggesting a decreased influence of rotation. Also note how the horizontal length scale in the high Ta* simulations, which host a large-scale vortex, is constrained by the domain size.

3.4.3 High Ta^* simulations

In contrast to the low Ta^* case, the behavior of high Ta^* simulations ($\mathrm{Ta}^* = 1$ and 10) is radically different from that described in studies of non-rotating ODDC. In Figure 3.4 we see that neither of the high Ta^* simulations shows clear stepwise increases in either the compositional flux or $\gamma_{\mathrm{tot}}^{-1}$. Instead we see turbulent fluxes that grow slowly and oscillate rapidly after saturation of the linear instability until they reach a highly variable statistically stationary state.

The $\mathrm{Ta}^* = 1$ and $\mathrm{Ta}^* = 10$ simulations are themselves quite different from one another. Figure 3.10 shows that the growth of step-like density perturbations through the γ-instability occurs for the $\mathrm{Ta}^* = 1$ simulation just as they do in the low Ta^* cases. However, from Figure 3.5 we see that their amplitudes never becomes large enough to trigger the onset of convection. The absence of the standard stepwise increase in the fluxes associated with the transition to layered convection also supports the idea that the latter does not happen in this simulation (see Figure 3.4). Interestingly, the snapshot of chemical composition shown in Figure 3.10 reveals that the system is dominated by a large scale cyclonic vortex. Inspection of the vertical velocity field shows that it is (roughly) constant within the vortex, which is consistent with Taylor-Proudman balance but is inconsistent with a system composed of convective layers separated by interfaces that resist penetrative motion. In some sense, it is perhaps more appropriate to consider $\mathrm{Ta}^* = 1$ to be a transitional case rather than a high Ta^* case because it displays features of both high and low Ta^* regimes.

For significantly higher Ta^* (in this case $\mathrm{Ta}^* = 10$) we see that the growth of perturbations to the density profile is completely suppressed for the duration of the simulation. Instead, after a transitional period the system becomes dominated by a cyclonic vortex similar to that observed in the $\mathrm{Ta}^* = 1$ simulation albeit with much stronger vorticity. From the snapshots of vertical vorticity, ω_z, in Figure

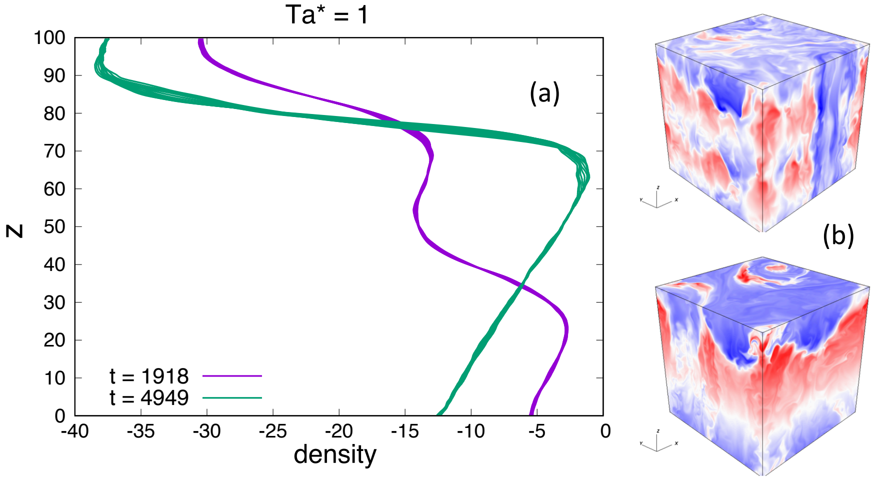

Figure 3.10: (a) Density profiles and (b) snapshots of the chemical composition field for a simulation with $\mathrm{Ta}^* = 1$, $\mathrm{Pr} = \tau = 0.1$, $R_0^{-1} = 1.25$ and $\theta = 0$. Note the presence of both a large scale vortex and layers.

3.12 we see that the simulations with $\mathrm{Ta}^* = 1$ and 10 have highly concentrated, vertically invariant vortex cores, necessarily surrounded by a more diffuse region of mostly anti-cyclonic vorticity (since $\int\int \omega_z(x, y, z)dxdy = 0$ for all z). We find that, based on all available simulations, these large-scale vortices only occur in the high Ta^* regime. By comparison, the $\mathrm{Ta}^* = 0.1$ simulation shows no large scale coherent structure in the vorticity field (which is true of the other low Ta^* simulations as well). These features are strongly reminiscent of the large scale vortices found by Guervilly et al. (2014) in rotating Rayleigh-Bénard convection using stress-free boundary conditions. In a parameter study they found that Reynolds numbers greater than 300 and Rossby numbers less than 0.15 were needed for large scale vortices to form. Using the Reynolds number from Guervilly et al. (2014) defined as

$$\mathrm{Re} = \frac{w_{\mathrm{rms}} L_z}{\mathrm{Pr}}, \tag{3.25}$$

where w_{rms} is the rms vertical velocity, we find that values of Re for our simulations

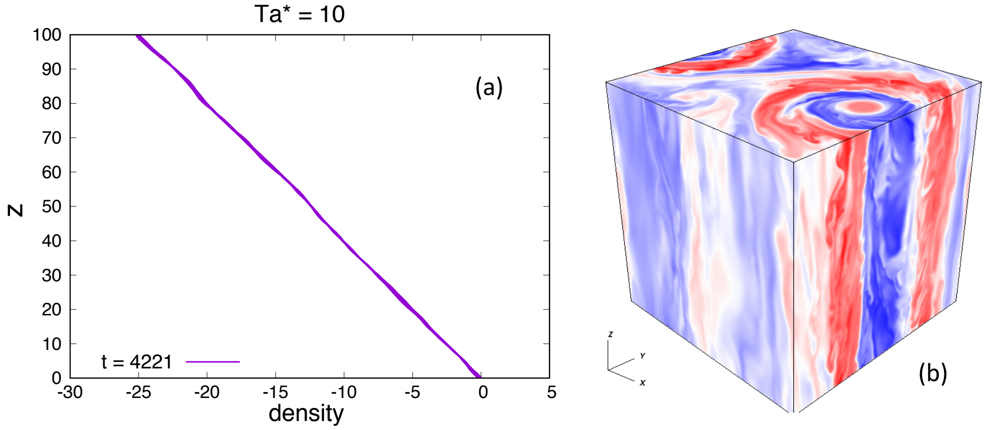

Figure 3.11: (a) Density profiles and (b) snapshots of the chemical composition field for a simulation with $\mathrm{Ta}^* = 10$, $\mathrm{Pr} = \tau = 0.1$, $R_0^{-1} = 1.25$ and $\theta = 0$. Note the complete absence of perturbations to the background density profile, indicating that layering modes do not grow.

are $\sim 10^3$. Meanwhile, the Rossby numbers are shown in Figure 3.9 and are less than 0.1 for high Ta*. This suggests that their vortex formation process may be applicable to our high Ta* simulations despite the significant differences in the systems being studied (ODDC vs. Rayleigh-Bénard convection). Also as in Guervilly et al. (2014), we find that whenever large scale vortices form they always grow to fill the horizontal extent of the domain[1]. Julien et al. (2012) proposed that this may always occur in Cartesian domains using the $f-$plane approximation regardless of box size. However they argued that this would be limited in practice by the Rossby radius of deformation in astrophysical objects. Beyond that size, convection or ODDC would likely lead to development of zonal flows in banded structures instead.

The amount of energy that can be extracted from ODDC to drive large scale vortices in the high Ta* regime is illustrated in Figure 3.13 where we see the vast majority of kinetic energy in the $\mathrm{Ta}^* = 1$ and 10 simulations goes into horizontal

---

[1] To verify this, we have run an additional simulation in a domain of horizontal scale $200d \times 200d$, and height $50d$. The large-scale vortex grew to fill the domain in this case as well.

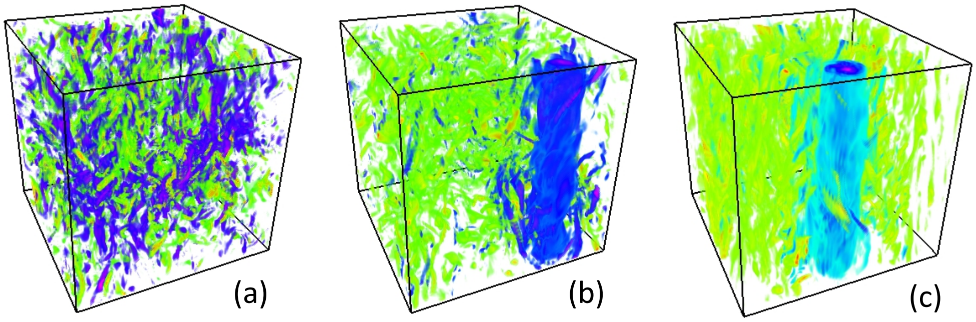

Figure 3.12: Volume-rendered plots of the component of vorticity in the z-direction, ω_z, for three simulations with $\mathrm{Pr} = \tau = 0.1$, $R_0^{-1} = 1.25$ and $\theta = 0$. (a) $\mathrm{Ta}^* = 0.1$. (b) $\mathrm{Ta}^* = 1$. (c) $\mathrm{Ta}^* = 10$. Purple/blue implies positive (cyclonic) vorticity, while red/yellow implies negative (anticyclonic) vorticity. The first simulation is in the low Ta^* regime ($\mathrm{Ta}^* = 0.1$) and the other two are in the high Ta^* regime ($\mathrm{Ta}^* = 1$ and $\mathrm{Ta}^* = 10$). Vertically coherent, large scale vortices are present in the high Ta^* simulations, but no large-scale coherent structures exist in the low Ta^* case.

fluid motions. These results showing ratios of horizontal kinetic energy to total kinetic energy are consistent with those calculated in Guervilly et al. (2014). The total amount of kinetic energy in the vertical fluid motions remains the same however in all the simulations, while it is the total kinetic energy of the system that is much larger for high Ta^* than for low Ta^* simulations.

It is worth noting that while the thermal and compositional fluxes (see Figure 3.4) and vertical velocity stop growing and reach a statistically stationary state (at around $t = 3500$ in both high Ta^* simulations) the total kinetic energy continues to grow (driven by the continued growth of the horizontal kinetic energy) and has not saturated by t =6000. This can be attributed to the fact that horizontal fluid motions are only limited by viscosity, and may only saturate on the global viscous diffusion timescale which is $\sim 10^5$ in these simulations.

Unlike in the low Ta^* regime where average fluxes are calculated through time-integration of the quasi-steady 1-layered phase, we choose ranges for time integration of fluxes from $t = 3500$ to the end of the simulations in the high Ta^*

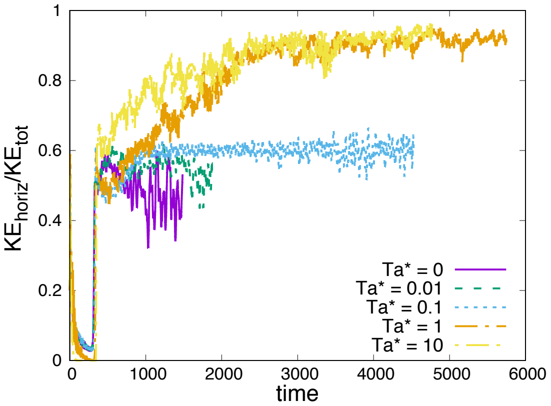

Figure 3.13: Horizontal kinetic energy as a fraction of the total for simulations with $\mathrm{Pr} = \tau = 0.1$, $R_0^{-1} = 1.25$, and $\theta = 0$, for various values of Ta^*. In the high Ta^* case this quantity is a proxy for the strength of the large-scale vortices, since they almost entirely dominate the energetics of the system.

regime. From Table 1 we see that the simulation with $\mathrm{Ta}^* = 1$ has the weakest transport in either Ta^* regime with 58.1% and 67.4% reductions to thermal and compositional transport, respectively, compared to the non-rotating case. Interestingly, the $\mathrm{Ta}^* = 10$ simulation shows a slight increases in flux over the $\mathrm{Ta}^* = 1$ case. A possible explanation for this is that the presence of a stably stratified interface separating non-convective layers in the $\mathrm{Ta}^* = 1$ simulation inhibits vertical motion through the large-scale vortex. This could also suggest that in the high Ta^* regime, increased rotation may actually serve to enhance transport rather than suppress it, through vertical motions whose coherence is strengthened by the vortex. However, by contrast with the layered regime, fluxes in the presence of a large scale vortex are highly dependent on the aspect ratio of the box. In Table 1 the narrower simulation at high $\mathrm{Ta}^* = 10$ has significantly higher fluxes than its wider counterpart. This makes it challenging to scale our results to simulations with larger domains, let alone apply them to more realistic astrophysical situations.

Also noteworthy in Table 1 is that $\gamma_{\mathrm{tot}}^{-1}$ in the ultimate statistically steady state is roughly the same across all simulations (namely $\gamma_{\mathrm{tot}}^{-1} \approx 0.5 - 0.65$) with high Ta* simulations having a $\gamma_{\mathrm{tot}}^{-1}$ that is at most 15% lower than in the low Ta* regime. This is significantly less than the variability that occurs due to the formation of large scale structures (layers or vortices): Figure 3.4b shows how $\gamma_{\mathrm{tot}}^{-1}$ increases from roughly 0.35 in the homogeneously turbulent phase to about 0.6 in the ultimate stages.

3.5 Varying Pr, τ, and R_0^{-1}

We now study the effect of varying Pr, τ, and R_0^{-1} on both the quantitative and qualitative attributes of rotating ODDC discussed in the previous section. This is not meant to be an exhaustive study, but rather to test whether the conclusions from previous section still hold.

3.5.1 Varying Pr and τ

In order to study the effect of varying Pr and τ we show a set of simulations with $\mathrm{Pr} = \tau = 0.3$, and $R_0^{-1} = 1.1$. As in Section 3.4, we have chosen parameters at which layers form in non-rotating ODDC. Figure 3.14 shows the evolution of the turbulent compositional flux as a function of time for simulations with $\mathrm{Ta}^* = 0, 0.09, 0.9, 9$, and 90 (corresponding to $\mathrm{Ta} = 0, 1, 10, 100$ and 1000). Consistent with Section 3.4 we find that at low Ta* stepwise increases in mixing rates indicate the transition to layered convection, whereas in the high Ta* case we do not. The transition between low and high Ta* is still $\mathrm{Ta}^* \approx 1$ (equivalently $\mathrm{Ta} = 10$ when $\mathrm{Pr} = 0.3$). This shows that Ta* is a more appropriate bifurcation parameter than Ta to determine when ODDC is rotationally dominated. As in Section 3.4, layer formation only occurs in the low Ta* regime. As with the $\mathrm{Ta}^* = 1$ simulation from Section 3.4 which shows characteristics of both high and low Ta^* ODDC, the $\mathrm{Ta}^* = 0.9$ simulation here develops a large scale vortex, as well as layer-like perturbations to the background density profile (without evidence of actual layered convection).

Large scale vortices are observed in simulations with $\mathrm{Ta}^* = 0.9$ and 9 and look very similar to the corresponding snapshots of the $\mathrm{Ta}^* = 1$ and 10 simulations in Figures 3.10 and 3.11 from the previous section. Interestingly, however the large scale vortex does not form in our most rapidly rotating simulation with $\mathrm{Ta}^* = 90$; instead we see multiple small scale vortices (see Figure 3.14). Analysis of Re and Ro for this simulation places it in a regime where large scale vortices should form according the criteria of Guervilly et al. (2014). This suggests that there may be additional constraints on the formation of large scale vortices in ODDC which should be determined through a more in-depth survey of parameter space in a future study. Surprisingly, the compositional fluxes for the $\mathrm{Ta}^* = 9$ and 90 runs are similar, which is likely a coincidence as we saw that the fluxes in the presence of large scale vortices depend on domain size.

3.5.2 Simulations at large R_0^{-1}

The simulations we have presented so far were runs with small values of R_0^{-1} which are conducive to layer formation in non-rotating ODDC. However, there is a range of larger values of R_0^{-1} where a system is unstable to ODDC, but where layers are not predicted to spontaneously form through the γ-instability. Previous studies have showed that, without exception, simulations in this parameter regime remain non-layered for as long as they are run. These simulations are dominated by large scale gravity waves and were studied in depth by Moll et al. (2016) in the context of non-rotating ODDC. In that work they found that the growth of

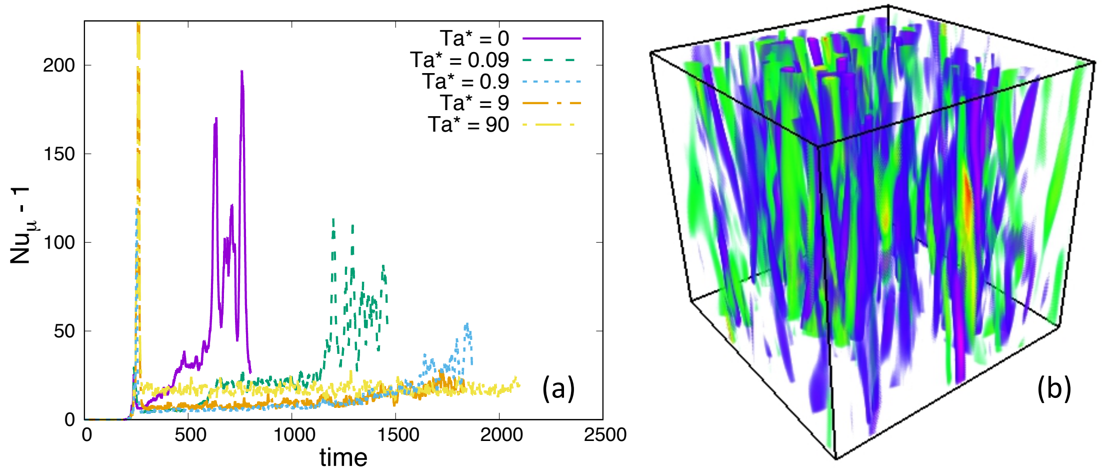

Figure 3.14: (a) Non-dimensional turbulent compositional flux for simulations with Pr $= \tau = 0.3$ and $R_0^{-1} = 1.1$. One simulation is in the low Ta* regime (Ta$^* = 0.3$) and the other three are in the high Ta* regime. (b) Snapshot of the component of vorticity in the z-direction for the most rapidly rotating simulation at Ta$^* = 90$, which appears to be dominated by small scale vortices. This may suggest that large-scale vortices only occur in a specific range of values of Ta* (with $\theta = 0$).

large scale gravity waves is associated with very moderate (but still non-zero) increases in thermal and compositional transport. However, these increases are very small compared to the increases in turbulent transport due to layers, and are likely unimportant for the purposes of stellar and planetary modeling. As a result, turbulent transport by ODDC at R_0^{-1} greater than the layering threshold R_L^{-1} can be ignored.

We now address how rotation affects non-layered ODDC (ie. ODDC at $R_0^{-1} > R_L^{-1}$). As in Section 3.4, we present five simulations with Ta$^* = 0, 0.01, 0.1, 1$ and 10, and with Pr $= \tau = 0.1$ and $\theta = 0$. However, for each of these simulations we now set $R_0^{-1} = 4.25$. For comparison, for the stated values of Pr and τ, $R_L^{-1} \simeq 1.7$ and the critical inverse density ratio for marginal stability is $R_c^{-1} = 5.5$.

As in Section 3.4 we find that high R_0^{-1} simulations can be divided into two general classes of behavior depending on Ta*. As seen in the snapshots in Figure

3.15, low Ta* simulations are qualitatively similar to non-rotating simulations in that they are dominated by large scale gravity waves. The strongest gravity wave mode in both the Ta$^* = 0$ and Ta$^* = 0.01$ simulations has three wavelengths in the vertical direction, one wavelength in the x-direction, and is invariant in the y-direction. The simulation with Ta$^* = 0.1$ by contrast is dominated by a larger scale mode with a single wavelength in each spatial direction. Despite their qualitative similarity, inspection of the compositional flux in Figure 3.16 shows large reductions compared to the non-rotating simulation (Ta$^* = 0$), even in the case where Ta$^* = 0.01$. To understand why this is the case note how Ro is small even in the lowest Ta* simulation. This is because the rms velocities are very small in this regime. Rotation therefore plays a role in the saturation of the gravity waves and acts to reduce their amplitudes, which in turn strongly reduces the mixing rates.

As seen in the snapshot in Figure 3.15e, the Ta$^* = 10$ simulation is dominated by vertically invariant vortices, while the Ta$^* = 1$ is again a transitional case which shows evidence both of gravity waves and of vortices. A significant difference with the results of Section 3.4 however, is that vortices at low R_0^{-1} are large-scale, while those at high R_0^{-1} are small-scale (for the same values of Ta*). This suggests that the formation of large-scale vortices requires a more unstable stratification (which leads to more turbulence) than is present in the high R_0^{-1} simulations shown here. This is, again, qualitatively consistent with the findings of Guervilly et al. (2014) that large scale vortices only form for sufficiently high Reynolds number.

The most rapidly rotating simulation (Ta$^* = 10$) shows a slight increase in the compositional flux compared to the non-rotating simulation but remains far less efficient than layered convection. Importantly, as with the non-rotating simulation, layers never form at any point (when $R_0^{-1} = 4.25$). Consequently, the conclusion from Moll et al. (2016), that fluxes through non-layered (high R_0^{-1}) systems are effectively diffusive, remains valid for all the simulations presented here.

3.6 Inclined simulations

So far, for simplicity, we have discussed simulations in which the rotation vector is aligned with the direction of gravity, and which only model conditions applicable to the polar regions of a star or giant planet. We now discuss the dynamics of ODDC at lower latitudes (ie. simulations with $\theta \neq 0$). In what follows, we return to the parameters studied in Section 3.4 (ie. $\mathrm{Pr} = \tau = 0.1$ and $R_0^{-1} = 1.25$). We focus on two sets of simulations with $\mathrm{Ta}^* = 0.1$ and 10, respectively, which are each comprised of runs with angles $\theta = \frac{\pi}{8}$, $\frac{\pi}{4}$, $\frac{3\pi}{8}$, and $\frac{\pi}{2}$.

Figure 3.17 shows the growth of the linear instability by way of the heat flux as a function of time for the set of simulations with $\mathrm{Ta}^* = 10$. Each simulation grows at roughly the same rate regardless of inclination, which is expected from linear theory. However there is a slight difference between the amplitudes in inclined simulations and the non-inclined simulation. This can be understood by considering that the simulations are initialized with small amplitude, random perturbations on the grid scale and many more modes are initially attenuated in the inclined case than in the case where $\theta = 0$ (see Section 3.3). As a result the amount of energy in the initial perturbations projected onto the fastest growing modes is smaller. Figure 3.18 shows snapshots of the chemical composition field during the growth of the primary instability for simulations with $\theta = 0$, $\frac{\pi}{8}$, $\frac{\pi}{4}$, $\frac{3\pi}{8}$, and $\frac{\pi}{2}$. In all inclined simulations, there are prominent modes that are invariant in the direction of rotation. In simulations with smaller (or no) inclinations ($\theta = 0$ and $\frac{\pi}{8}$) the dominant modes are those with structure both in the x and y

directions while simulations with larger inclinations (simulations that are closer to the equator) have a strong preference for modes that are invariant in the plane spanned by the rotation and gravity vectors.

While the behavior of the linearly unstable phase is qualitatively similar for both low and high Ta^* simulations regardless of θ, we find that this is not the case after the saturation of the basic instability. While inclination has only small effects on systems in the low Ta^* regime, it has a more significant influence on post-saturation dynamics in the high Ta^* regime.

Figure 3.19 shows turbulent compositional fluxes for simulations in the low Ta^* regime ($\mathrm{Ta}^* = 0.1$). The fluxes in the homogeneously turbulent phase are roughly independent of θ indicating that inclination should have a minimal effect on the growth rate of layering modes through the γ-instability. Indeed, the stepwise increases in fluxes over time show that layer formation occurs at all inclinations. Inspection of the chemical composition profiles show that the layer interfaces are perpendicular with the direction of gravity, regardless of inclination. The latter seems to affect the layer formation timescale and layer merger rate, but this may be due the inherent stochasticity of the convective layers. Finally, aside from the equatorial case, we find that inclination has a minimal impact on flux in each layered phase, so the flux laws discussed in Section 3.4.2 apply more or less at all latitudes. As a result, we expect that heat and compositional fluxes through layered convection on a sphere should be fairly isotropic.

Figure 3.19 also shows the turbulent compositional flux for simulations in the high Ta^* regime ($\mathrm{Ta}^* = 10$). The lack of clear stepwise increases indicates that layer formation is suppressed for most values of θ (as is the case in non-inclined simulations). The notable exception to this rule is the simulation at the equator ($\theta = \frac{\pi}{2}$) where layers are observed to form even in the high Ta^* case. Why they form in this case remains to be determined.

Another major difference between inclined and non-inclined simulations is that there is no evidence for the large scale vortices in simulations with $\theta \neq 0$, even though they are observed in $\theta = 0$ simulations at the same parameters (see Section 3.4). This is illustated in Figure 3.20 which shows the quantity $\omega_{yz} = \frac{\omega \cdot \mathbf{\Omega}}{|\mathbf{\Omega}|}$. There are many smaller scale vortices aligned with the rotation axis but no large scale vortex. This is even true in the simulation with the smallest inclination ($\theta = \frac{\pi}{8}$), bringing into question whether large scale vortices would be common in stars and planets except exactly at the poles. The inclination of the small scale vortices is associated with smaller vertical transport, and Figure 3.19 suggests that mixing becomes less efficient as θ gets larger (except very close to the equator).

3.7 Conclusion

3.7.1 Summary and discussion

The main result of this study is the discovery of two distinct regimes in rotating ODDC depending on whether the rotation rate Ω is high or low. We find that the most appropriate parameter for determining if a system is in one regime or the other is $\mathrm{Ta}^* = \frac{4\Omega^2 d^4}{\kappa_T^2}$, where d is given in Equation (3.6) and κ_T is the thermal diffusivity. The transition from the regime with slow rotation to the regime that is rotationally dominated occurs consistently at $\mathrm{Ta}^* \approx 1$.

In the low Ta^* regime in polar regions (with $\theta = 0$), rotating ODDC behaves in a qualitatively similar way to non-rotating ODDC. The transition to layered convection (or lack thereof) at low Ta^* is consistent with the predictions of γ-instability theory made for non-rotating ODDC (Mirouh et al., 2012): at parameters where layers form in non-rotating ODDC, we also observe layer formation in low Ta* simulations. Likewise, in the simulations we ran at non-layered parameters, we find that low Ta* simulations do not form layers, and are dominated by gravity waves like their non-rotating counterparts (Moll et al., 2016). We understand this to be true because the thermal and compositional fluxes immediately after saturation of the primary instability of ODDC are unaffected by rotation in this regime. Since the γ-instability only depends on these fluxes, it is similarly unaffected. Given the limited number of available simulations, we cannot say definitively what effect (if any) rotation has on the layering threshold R_L^{-1} (the value of the inverse density ratio, R_0^{-1}, below which layers are predicted to form through the γ-instability, and above which they are not), only that it is not significant in the low Ta* simulations presented here, which are far from that threshold. However, we believe that R_L^{-1} would be relatively unaffected by rotation for Ta$^* < 1$.

Beyond these qualitative similarities with non-rotating simulations, however, rotation in low Ta* simulations has a deleterious effect on thermal and compositional transport in both the layered and non-layered parameter regimes. For a given layer height, turbulent fluxes through a thermo-compositional staircase decrease as rotation increases (eg. by about 50% in the Ta$^* = 0.1$ simulation presented in Section 3.4.2). However, our results also suggest that this effect becomes smaller as the layer height increases (through mergers, for example). For reasonably large layer heights, we postulate that rotation has a minimal effect on ODDC, and that the flux laws originally proposed by Wood et al. (2013). actually hold. Turbulent fluxes through non-layered ODDC in the gravity-wave-dominated phase are reduced by as much as 90% compared with the non-rotating case, but this merely implies that they remain negligible as discussed by Moll et al. (2016).

Finally, low Ta* simulations at higher colatitude θ are not significantly different from their polar counterparts. Inclination has a negligible effect on the temperature and compositional fluxes, but may induce differences in the time scales of layer formation and mergers.

In the high Ta* regime, dynamics are radically different from non-rotating and low Ta* simulations. Most striking is that layer formation is inhibited at low inverse density ratios (except in the equatorial case). Instead, the dynamics are dominated by vortices aligned with the direction of rotation, which span the domain. Their horizontal scales seem to depend on R_0^{-1}, θ and Ta*. In polar regions, we observe that some simulations become dominated by a single large scale cyclonic vortex which grows to fill the domain, similar to those observed by Guervilly et al. (2014) in rotating Rayleigh-Bénard convection. Our preliminary data show that this phenomenon may be limited to low R_0^{-1}, together with Ta* between 1 and 10, but the precise conditions necessary for these large scale vortices to form remain to be determined. We find that large scale vortices do not occur in the most rapidly rotating simulation (Ta$^* = 90$) at low R_0^{-1}, in any of the high R_0^{-1} simulations or in any of the inclined simulations. In these cases the system dynamics are instead dominated by many smaller scale vortices of both polarities.

Turbulent fluxes through different types of vortices vary with parameters in a complex manner, and it is therefore difficult to make general statements about them. The fluxes in the presence of large scale vortices are significant, but appear to be highly dependent on the dimensions of the domain, which makes it difficult to predict in situ mixing in a star or planet. On the other hand, fluxes in the presence of small scale vortices are not likely to be dependent on domain size, but their dependence on Ta* and R_0^{-1} has yet to be extensively studied. The most definitive aspect of the fluxes in simulations that host small scale vortices is that they are highly dependent on the inclination θ, with higher inclinations causing less efficient transport (except at the equator). This is due to the fact that velocities are constrained to being along the axis of rotation by Taylor-Proudman effects. It is interesting to note that in the high Ta* regime, layers form in our equatorial simulation ($\theta = \frac{\pi}{2}$). In this run, turbulent fluxes through the layers are comparable to layered fluxes in the low Ta* and non-rotating regimes. All of this suggests that the poles and equator may be regions of strongly enhanced temperature and compositional transport in ODDC, while turbulent mixing at latitudes in between is quenched.

Finally, simulations where Ta$^* \approx 1$ appear to be edge cases with features of both high and low Ta*. At parameters conducive to layering, simulations with Ta$^* \approx 1$ show evidence of perturbations to the background density profiles, indicating the growth of the γ-instability. However, we also see the development of large-scale vertically invariant vortices which prevent actual layered convection from occurring. Also, when Ta$^* \approx 1$ at non-layered, gravity-wave-dominated parameters, we see evidence of gravity waves as well as small thin vortices which are nearly vertically invariant.

There are several caveats to these conclusions that should be mentioned. The dimensionality of parameter space that would need to be explored to provide a comprehensive study of rotating ODDC is high, and comprises of (L_x, L_y, L_z), θ, Pr, τ, Ta* and finally R_0^{-1}. Computational limitations force us to be highly selective on the sets of simulations explored so this study does not constitute a comprehensive sweep of parameter space. As such, there may be behaviors that occur at unexplored parameters that are not addressed here.

First of all, in the interest of reducing computational expense we have chosen to run most of our simulations in domains with dimensions $(100d)^3$. With boxes of this size layers always merge until a single interface remains (as in the non-rotating case). It would be interesting to see in a taller domain if rotation has a role in determining the layer height (ie. to see if layers stop merging before reaching the one-layered phase). Wider domain sizes may also help to answer questions about the vortices present in high Ta^* simulations. Particularly, they may reveal whether large scale vortices have a characteristic horizontal length, or whether they always grow to fill the domain. Wider boxes may also show if there are so far undetected large scale features emerging in systems dominated by small scale vortices.

Another area of uncertainty is that the chosen values of R_0^{-1}, $R_0^{-1} = 1.25$ and $R_0^{-1} = 4.25$, are fairly close to the convective and marginal stability thresholds, respectively, making them somewhat extreme cases. While we do not believe that choosing less extreme parameter values would lead to dramatic qualitative changes in the results, we cannot rule this possibility out until further work has been completed.

Finally, for computational reasons, the values of Pr and τ chosen for our simulations ($\mathrm{Pr} = \tau = 0.1$ and 0.3) are substantially larger than the values in stellar interiors (where $\mathrm{Pr} \sim \tau \sim 10^{-6}$) and the interiors of giant planets like Jupiter and Saturn (where $\mathrm{Pr} \sim \tau \sim 10^{-3}$). Consequently, there may be additional physical effects that occur at low parameter values that are not observed here. However, the values used here may be closer to actual values for ice giants such as Uranus and Neptune whose equations of state are influenced by the presence of water and methane ices in their atmospheres (Redmer et al., 2011).

3.7.2 Prospects for stellar and planetary modeling

As summarized above, our results for the low Ta^* regime show that attenuation of the fluxes due to rotational effects is not likely to be significant for astrophysical models or observations. In this regime we advocate use of the parameterizations presented in Wood et al. (2013) in layered ODDC and Moll et al. (2016) in non-layered ODDC. However, a potentially observable effect of rotating ODDC in this regime could be related to how rotation affects the structure of layers and interfaces in low Ta* simulations. We have found in our experiments that rotation leads to layer interfaces that are more stably stratified than in non-rotating simulations. It may be possible in the future that such steep density gradients could be observed in a star through asteroseismology. This line of inquiry could even be extended to Saturn where it may be possible to detect density gradients using ring seismology (Fuller, 2014).

In the high Ta* regime the results of this study have potential observational implications for thermal and compositional transport in stars and planets. The sensitivity of the turbulent heat flux to θ in our high Ta* simulations suggests that the transport in a rapidly rotating giant planet could vary substantially with latitude (with higher fluxes at the poles and equator). Indeed, the gas giants in our own solar system are found to have luminosities that are independent of latitude, despite the fact that regions close to the equator receive more solar energy. Since we would expect regions of Jupiter or Saturn's atmosphere that get more radiation from the sun to have higher luminosities (because they are reradiating more solar energy) the isotropy of the outgoing flux in luminosity suggests that more heat from the interiors of these planets is being radiated at the poles than at other latitudes. Further study is warranted to determine if rapidly rotating ODDC contributes to this effect. The large-scale vortices present in the polar regions of the high Ta* simulations present an intriguing observational potential, of regions with strong heat and compositional fluxes and strong collimated vertical flows. However, there is reasonable doubt as to whether large scale vortices represent a real physical phenomenon. We only observe them to occur in polar simulations (in a limited range of Ta*), and it is possible that even a slight misalignment between the direction of gravity and the rotating axis could prevent them from forming.

For stars, in the case of semi-convection zones adjacent to convection zones, Moore & Garaud (2015) showed that non-rotating ODDC is always in the layered regime, and that transport through the semi-convective region is so efficient that the latter gets rapidly absorbed into the convection zone. In essence, aside from a fairly short transient period, the star evolves in a similar way taking into account semi-convection, or ignoring it altogether and using the Schwarzchild criterion to determine the convective boundary. Our results suggest that this conclusion remains true for slowly rotating stars. However, if the star is in the high Ta* regime instead, layered convection is suppressed, transport through the semi-convective region is much weaker, and may possibly depend on latitude. This would in turn imply fairly different evolutionary tracks and asteroseismic predictions.

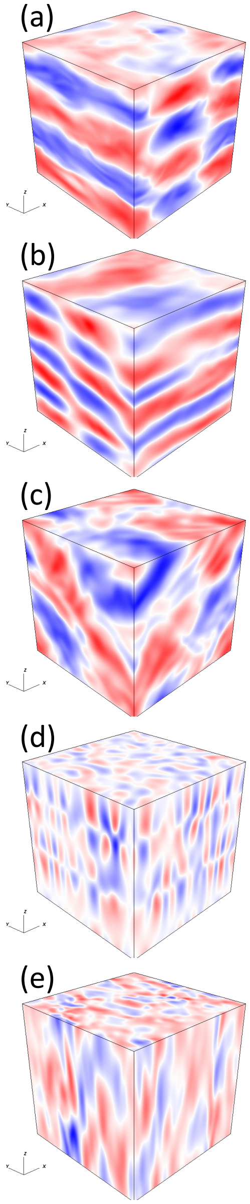

Figure 3.15: Snapshots of the horizontal velocity field (u or v) for simulations with $\mathrm{Pr} = \tau = 0.1$, $R_0^{-1} = 4.25$, and $\theta = 0$, for various values of Ta^*: (a) $\mathrm{Ta}^* = 0$, (b) $\mathrm{Ta}^* = 0.01$, (c) $\mathrm{Ta}^* = 0.1$, (d) $\mathrm{Ta}^* = 1$, and (e) $\mathrm{Ta}^* = 10$.

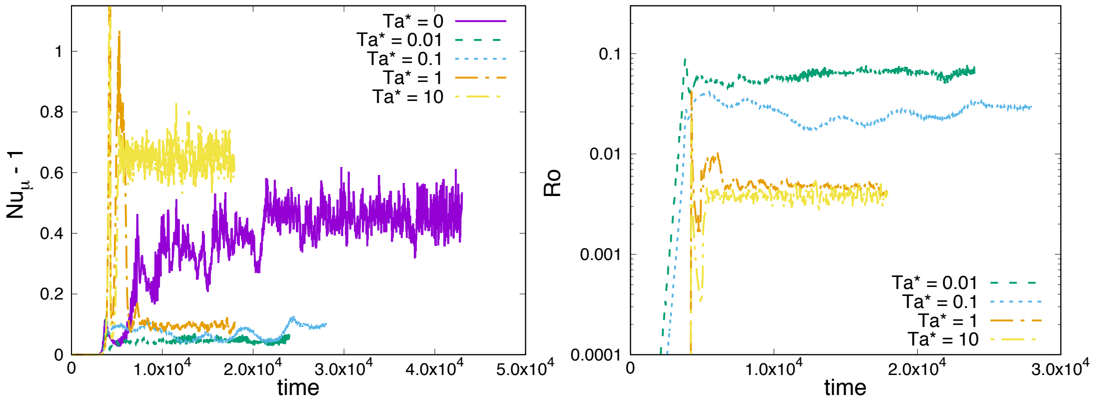

Figure 3.16: Time series of the turbulent compositional flux (left) and Rossby number (right) for simulations with $\mathrm{Pr} = \tau = 0.1$, $R_0^{-1} = 4.25$, and $\theta = 0$ for various values of Ta^*.

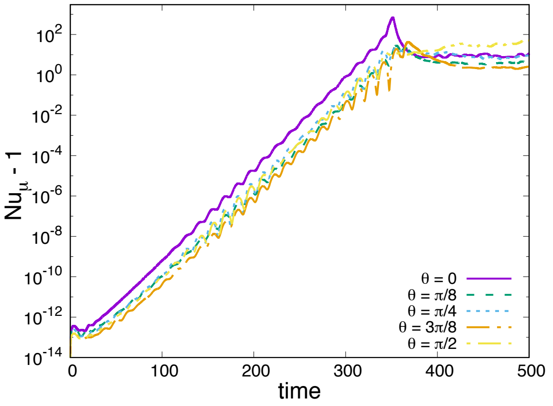

Figure 3.17: Nondimensional turbulent compositional flux during the primary instability growth phase, and immediately following non-linear saturation for simulations with $\mathrm{Pr} = \tau = 0.1$, $R_0^{-1} = 1.25$, $\mathrm{Ta}^* = 10$, and various values of θ.

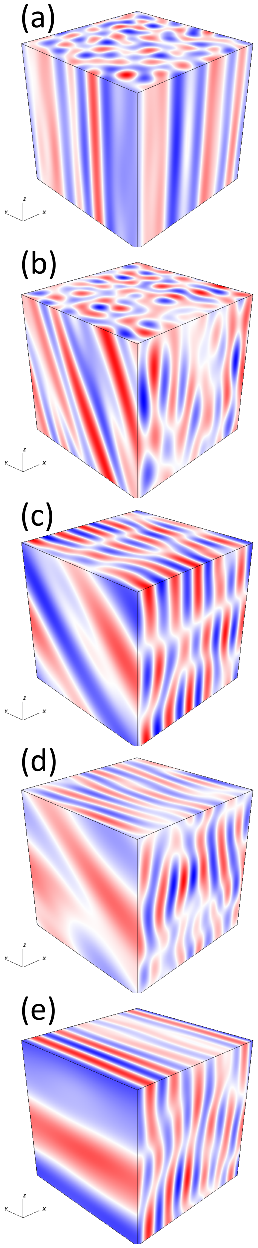

Figure 3.18: Snapshots of the vertical velocity field during the growth of the linear instability for simulations with $\mathrm{Pr} = \tau = 0.1$, $R_0^{-1} = 1.25$, $\mathrm{Ta}^* = 1$, and various values of θ: (a) $\theta = 0$, (b) $\theta = \pi/8$, (c) $\theta = \pi/4$, (d) $\theta = 3\pi/8$ and (e) $\theta = \pi/2$.

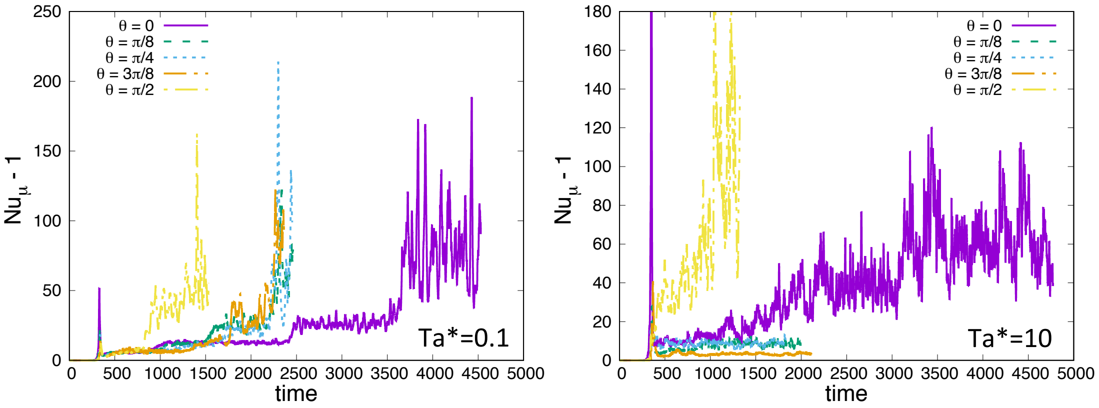

Figure 3.19: Long-term behavior of nondimensional turbulent fluxes of composition for simulations with stated values of θ and with $\mathrm{Ta}^* = 0.1$ (left) and $\mathrm{Ta}^* = 10$ (right). In both sets of simulations, $\mathrm{Pr} = \tau = 0.1$, and $R_0^{-1} = 1.25$. In the low Ta^* case the succession of layered phases is similar for polar and inclined simulations, with only small differences in layering time scales and turbulent fluxes. In the high Ta^* case, fluxes in inclined simulations are sharply attenuated compared to the polar case.

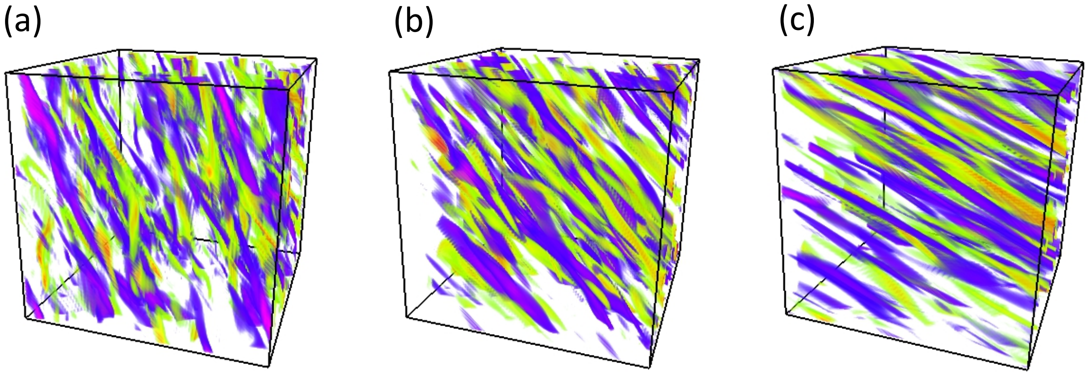

Figure 3.20: Snapshots of ω_{yz}, the component of the vorticity parallel to the rotation axis, during saturation of the linear instability. Shown are simulations with $\mathrm{Pr} = \tau = 0.1$, $R_0^{-1} = 1.25$, $\mathrm{Ta}^* = 1$, and (a) $\theta = \frac{\pi}{8}$, (b) $\theta = \frac{\pi}{4}$ and (c) $\theta = \frac{3\pi}{8}$. In each case, coherent small scale vortices are aligned with the axis of rotation.

Chapter 4

Diffusive Convection with Proto-Layered

4.1 Introduction

Up to this point, we have discussed only double-diffusive instabilities that are triggered through infinitesimal perturbations (this is indeed how we define ODDC). As discussed in Chapter 1, ODDC can be either layered or non-layered depending on the value of the inverse density ratio, R_0^{-1}. However, even in the regime where layers do not spontaneously form ($R_L^{-1} < R_0^{-1} < R_c^{-1}$, where $R_L^{-1} \sim \mathrm{Pr}^{-1/2}$ and $R_c^{-1} = \frac{\mathrm{Pr}+1}{\mathrm{Pr}+\tau}$) it is possible to force a diffusive system into a persistent layered configuration. This can be accomplished by exciting the well-known subcritical branch of double diffusive convection with finite amplitude perturbations (Huppert & Moore, 1976). In fact, the subcritical layering instability is by necessity the relevant one in geophysical systems.

Indeed, diffusive convection was first observed in terrestrial oceans and lakes (Degens et al., 1973; Perkin & Lewis, 1984). Fluids with a stable composition gradient and an unstable temperature gradient are found in the arctic ocean both in the upper layers where melting ice can cause the surface to be colder and fresher than the water below which intrudes from the North Atlantic, and on the ocean floor where geothermal heating creates weakly unstable temperature gradients in water that is stably stratified in salinity (Timmermans et al., 2003). The same process of geothermal heating may create diffusive systems in geologically active lakes as well, where dissolved volcanic gasses (such as CO_2 and methane) provide a strongly stabilizing compositional stratification. Crucially, layering is observed in all of these cases, yet none of them are in the ODDC-unstable regime. Recall that in order for a system to be linearly unstable, the inverse density ratio, R_0^{-1}, must satisfy the condition

$$1 < R_0^{-1} < R_c^{-1} = \frac{\mathrm{Pr}+1}{\mathrm{Pr}+\tau} \,. \tag{4.1}$$

In water, $\mathrm{Pr} = 7$ and $\tau \simeq 0.01$ resulting in a critical inverse density ratio of $R_c^{-1} = 1.14$. However, the geophysical examples listed above typically have $R_0^{-1} \approx 5-10$, and are therefore stable to ODDC. This strongly suggests that layering in this case must occur via a subcritical instability, which necessitates forcing layers to form with finite amplitude perturbations.

Forced layering in diffusive convection was studied first in geophysical laboratory experiments by Turner (1965). In those experiments a double diffusive fluid was initialized in a layered configuration, in which water with a low concentration of salt was carefully deposited on top of a layer with a higher salinity and then heated from below. This setup lead to rising and falling convective plumes within the layers and enhanced diffusion of temperature and salt through the convectively stable layer interface. In those experiments, the flux of temperature, F_T, through the thin interface separating the layers was found to be

$$F_T \propto (\Delta T)^{4/3} \tag{4.2}$$

where ΔT is the temperature difference across the interface. The compositional flux (in their case, salinity) was similarly found to be $F_C \propto \Delta C^{4/3}$. Both scalings can be explained in terms of dimensional analysis. Similar results were later found by Shirtcliffe (1973) using a salt-sugar double diffusive system. Later, Linden & Shirtcliffe (1978) described the steady state profiles of temperature and salinity in layered systems with diffusive interfaces similar to those studied by Turner (1965) and Shirtcliffe (1973). Assuming an equilibrium between the thickening of the interface due to diffusion and the scouring of temperature and salt from the interface due to layered convection, they concluded that the inverse flux ratio, $\gamma_{\mathrm{tot}}^{-1}$, in such a system must be

$$\gamma_{\mathrm{tot}}^{-1} = \frac{F_C}{F_T} = \tau^{1/2}\,. \tag{4.3}$$

As noted in Chapter 3, the quantity $\gamma_{\mathrm{tot}}^{-1}$ is of great significance in planetary science because in most cases, the intrinsic heat flux of a planet can be measured, but the compositional flux cannot. However, if $\gamma_{\mathrm{tot}}^{-1}$ can be constrained through theory alone, predictions can be made for the compositional flux through a planet's interior (see, for instance, Stevenson, 1982; Guillot et al., 2004).

In an equilibrated staircase, the fluxes through the system as a whole are equal to the fluxes through the interface, which are also equal to the fluxes through the convective layers. It follows naturally from the prescription for $\gamma_{\mathrm{tot}}^{-1}$ of Linden & Shirtcliffe (1978) that the ratio of the compositional and thermal gradients in the interface should be

$$\frac{\partial C/\partial z}{\partial T/\partial z} = \tau^{-1/2}\,. \tag{4.4}$$

Finally, assuming that the ratio of the background gradients for the entire system must be smaller than the ratio of the gradients in the interface, implies that

$$R_0^{-1} < \tau^{-1/2}\,. \tag{4.5}$$

This sets a theoretical upper limit on R_0^{-1} for the existence of an equilibrium staircase, at least according to Linden & Shirtcliffe (1978).

Results from these studies of geophysical diffusive convection were then ported to the astrophysical context where Stevenson (1982) applied them to the deep interiors of gas giant planets and Merryfield (1995) adapted geophysical theories to stars. Further studies of astrophysical diffusive convection also continued to assume that it always takes the form of well mixed layers separated by stationary, diffusive interfaces (Leconte & Chabrier, 2012; Spruit, 1992, 2013) leading to predictions for the temperature flux and $\gamma_{\rm tot}^{-1}$ that were, on the whole, similar to those from the geophysical literature.

However, whether or not these geophysically-derived models of transport in subcritically-formed staircases apply to astrophysical conditions (where the Prandtl number is much lower) remains an open question. In what follows we study this issue using DNS in which layers are artificially induced through initial conditions, or what we refer to here as “proto-layered". We use the same mathematical model as in Chapter 1, where the system is governed by the equations in (1.7). We also use the same numerical simulation code (PADDI) with a few important modifications to the initial conditions. The dimensions of the domain for all simulations considered here are $(100d)^3$ with a resolution of at least 384^3 meshpoints. Furthermore, we primarily consider systems that are solidly in the regime where layers do not form *spontaneously* through the γ-instability (see Chapter 1).

In Section 4.2 we describe and compare different types of finite amplitude perturbations that may be used to excite the subcritical instability. In Section 4.3, we then discuss the conditions under which proto-layers lead to persistent layered structures in our simulations. In Section 4.4 we discuss the properties of proto-layered simulations where persistent layering takes hold, and compare our results to those from the geophysical literature. Finally, in Section 4.5 we present our conclusions.

4.2 Exciting the subcritical instability

Ignoring for now the question of how finite amplitude layering might naturally be triggered in stellar or planetary interiors, there are several ways of initializing a numerical experiment to create a layered system when $R_0^{-1} > R_L^{-1}$. One way to do it is to initialize the simulation with horizontally invariant regions where density is either constant or increases with height (and are hence convectively unstable). In what follows, we explore two different possible types of initial conditions. In one, we impose a sinusoidal initial perturbations to the temperature and chemical composition (now denoted with μ) fields given by,

$$\begin{aligned} \tilde{T}(z) &= \xi_T \quad , \\ \tilde{\mu}(z) &= A\cos\left(\frac{2\pi n_L}{L_z}z\right) + \xi_\mu \, , \end{aligned} \tag{4.6}$$

where n_L is the initial number of layers in the height L_z, A is the amplitude of the perturbation, and ξ_T and ξ_μ represent random small amplitude noise. As mentioned previously, for all simulations considered here, $L_z = 100$, so a 3-layered state would have layers of height $\simeq 33$, a 2-layered state would have layers of height $\simeq 50$, and a 1-layered state would have a layer height of 100. As seen in Equation (4.6), the initial high-amplitude perturbation is applied to the composition field only. This is appropriate because any perturbation we apply to the temperature field would quickly diffuse away (and become insignificant compared to the compositional perturbations) due to the fact that $\kappa_T \gg \kappa_\mu$.

In the second type of initial condition, we use stepped profiles that are closer to a staircase configuration with fully-mixed layers separated by thin, more stable interfaces. We construct them using the following initial temperature and compositional perturbations, similar to Noguchi & Niino (2010) and Carpenter et al. (2012), for instance:

$$\begin{aligned} \tilde{T} &= \left[z - \frac{L_z}{2}\left(\tanh\left[\frac{2z - L_z}{h}\right] + 1\right)\right] + \xi_T \,, \\ \tilde{\mu} &= R_0^{-1}\left[z - \frac{L_z}{2}\left(\tanh\left[\frac{2z - L_z}{h}\right] + 1\right)\right] + \xi_\mu \,. \end{aligned} \tag{4.7}$$

In this case, initial conditions are applied to both T and μ. These are initial conditions for a 1-layered system, however similar functions can be superimposed on one another to initialize multi-layered systems. The parameter h determines the initial interface thicknesses for both T and μ.

In either case, the density profile relates to these perturbations as,

$$\rho = (1 - R_0^{-1})z - \tilde{T} + \tilde{\mu} \,. \tag{4.8}$$

Note that for the sinusoidal case, there is a minimum amplitude that the perturbations must have in order to trigger layered convection. Assuming that an instability is only triggered if $\frac{d\rho}{dz} > 0$ somewhere in the fluid, the condition for instability is

$$|A| > \frac{L_z(R_0^{-1} - 1)}{2\pi n_L} = |A|_{\min} \; . \tag{4.9}$$

It is important to stress that this is a theoretical absolute minimum value. When $|A|$ is equal to this value, $\frac{d\rho}{dz} = 0$ at precisely one point in each proto-layer, and is negative (stable) everywhere else. The regions with unstable density gradients become larger as $|A|$ increases. However, for values of $|A|$ close to the limit (where unstable regions are small) other influences not considered by this model, such as viscosity or diffusion, may prevent persistent convective layers from forming. Therefore, in practice convective layers only form if $|A|$ is substantially larger than the threshold, $|A|_{\min}$.

By way of demonstrating that proto-layered simulations indeed lead to the formation of fully-developed thermo-compositional staircases, as well as testing the influence of initial conditions on the result, we first compare the long-term evolution of proto-layered systems initiated with a stepped profile and a sinusoidal profile to one another, as well as two systems which are identical except for the initial amplitudes of their sinusoidal perturbations.

In the first set of simulations, we use the parameters $\mathrm{Pr} = \tau = 0.03$ and $R_0^{-1} = 4.0$, and start with perturbations that each have 3 layers. For the stepped profile we use $h = 5$, while for the sinusoidal profile, we use $A = 65$ ($|A|_{\min} \approx 16$ for the given parameters).

Figure 4.1a shows the evolution of the density profiles for each simulation, and Figure 4.1b shows the evolution of their respective Nusselt numbers. We see that the two methods yield identical steady states after a fairly long transient period, with similar mean density profiles and similar transport rates. In both cases, we see a well-defined thermo-compositional staircase with 3 mixed layers (regions of nearly constant density) separated by thin and apparently stable interfaces (see

Section 4.4 for more on the staircase structure). The staircases thus appears to be

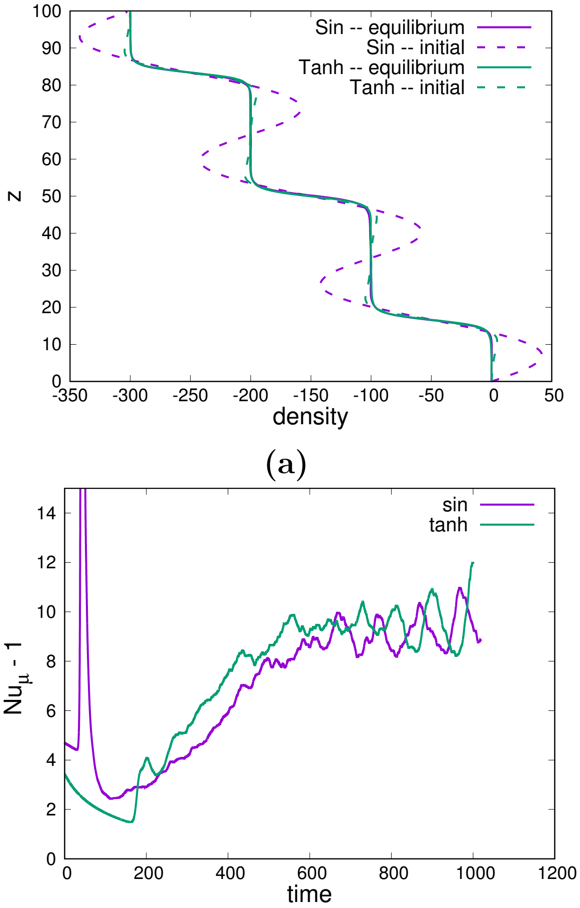

(a)

(b)

Figure 4.1: (a) Density profiles for two 3-layered simulations with different types of initial conditions (sinusoidal and stepped). Shown are initial profiles (dashed lines) and then profiles from when the simulations have reached equilibrium (solid). (b) Turbulent compositional flux for these two simulations. In their initial phase of growth, they are somewhat different, but the fluxes in the two simulations are similar when they reach equilibrium.

independent of initial proto-layered conditions, and in what follows, we continue to work only with the sinusoidal initial conditions from Equation (4.6).

In Figure 4.2 we compare two simulations at Pr $= \tau = 0.03$ and $R_0^{-1} = 7.87$, both initiated with 2 layers using the sinusoidal initial conditions, but with different initial amplitudes $A = 100$ and $A = 200$ respectively. Again, we see that the two simulations eventually converge to the same statistically steady state but it is interesting to notice that, in contrast to the previous pair of simulations, it takes a very long time to arrive at this quasi-stationary state. We believe that the adjustment occurs on a time scale comparable to the compositional diffusion time across the interface, defined as

$$t_C = \frac{H_I^2}{\tau} \tag{4.10}$$

where H_I is the initial thickness of a layer interface. In the $A = 100$ and 200 simulations, $t_C \approx 15000$ and 7000, respectively. From Figure 4.2 we see that the increases in the thermal and compositional fluxes are accompanied by commensurate changes in the layered structure of the system (layers gradually become thicker and interfaces become thinner).

This slow convergence notwithstanding, it is reassuring to see that, once the layer height is set through the scale height of the initial perturbation, there is a unique well-defined equilibrium configuration for the staircase, with a given interfacial structure and set thermal and compositional fluxes through it. We will discuss this structure more in Section 4.4.

Finally, it is worth noting that, regardless of initial conditions and initial numbers of layers, layered convection appears to remain in a configuration with the same number of layers as the initial conditions. This is in stark contrast to layers that form spontaneously through the γ-instability in ODDC, where Rosenblum et al. (2011) observed that no matter how many layers initially form, they always merge progressively until a single interface remains in the domain.

4.3 Conditions for layer formation

Aside from the obvious condition on the initial perturbation amplitude, it is interesting to ask under which other conditions proto-layers lead to the formation of an equilibrium staircase. We have found, for instance, that another limiting factor in the formation of persistent layers is the number of proto-layers with which a simulation is initialized. For example, Figure 4.3a shows the evolution of the density profiles from a simulation with $\mathrm{Pr} = \tau = 0.03$, $R_0^{-1} = 7.87$, $A = 100$ and $n_L = 3$ ($|A| > |A|_{\min}$ by a significant amount). We see that the perturbed density profile in the $n_L = 3$ simulation initially leads to the formation of 3 well-mixed layers, separated by laminar interfaces. However, over time the layers that initially form shrink and the stable interfaces thicken. Eventually, the layers disappear altogether, and what is left is weakly turbulent gravity-wave-dominated ODDC of the sort described in Chapter 2. Figure 4.3b confirms this by showing that temperature fluxes steadily decrease as the layers disappear (from about $t = 200$ to $t = 700$), and then start to grow modestly again due to the emergence of large scale gravity waves excited by ODDC. Generally, with the exception of one case with $\mathrm{Pr} = \tau = 0.03$ and $R_0^{-1} = 4$ (see Table 4.1), we find that most simulations with 3 layers are unstable, and return back to a non-layered state. By contrast, Figure 4.2 shows that $n_L = 2$ simulations with the same values of Pr, τ, and R_0^{-1} maintain their layered states. What factors decide whether a staircase can persist or diffuse away remains to be determined. However, a strong possibility is that convection within the layers has to be strong enough to prevent the diffusion of the interfaces. In 3-layered simulations, the intensity of convection within the layers is weaker, because their Rayleigh number is smaller. As a result, mixing is less efficient and the interface diffusion eventually takes over. By contrast, simulations with taller layers, or simulations that are generally more weakly stratified (i.e. for smaller R_0^{-1}), should be able to maintain their layered structure.

In fact, as noted in Section 4.1 both geophysical (Linden & Shirtcliffe, 1978) and astrophysical (Spruit, 2013) studies predict an upper limit on the inverse density ratio below which layered convection can be maintained, given by $R_0^{-1} = \tau^{-1/2}$. In order to test this law, we have run a number of proto-layered simulations that lead to staircases with 1 layers, at various values of Pr, τ, R_0^{-1}, and starting amplitudes $|A|$ (see Table 4.1 for details). Our results are reported in Figure 4.4, where circles show persistent layers while crosses show decaying layers. The theoretical upper limit given by Equation (4.5) is also plotted. This data show that R_0^{-1} can be significantly larger than $\tau^{-1/2}$ and still maintain layered convection. Similar observations of persistent layering at inverse density ratios larger than the theoretical limit have been observed in the past (Newell, 1984).

The fact that persistent layers exist for such large values of R_0^{-1} also suggests that the interfacial gradients of temperature and chemical composition, and hence $\gamma_{\mathrm{tot}}^{-1}$, may be different than the predicted values in Equations (4.3)-(4.5).

4.4 Layer properties and comparison to geophysical laws

In this section we analyze in more detail the results from a two 2-layered simulation with Pr $= \tau = 0.03$, $R_0^{-1} = 7.87$ and $|A| = 200$. As in the 3-layer cases mentioned in Section 4.3, convective layers are created that have uniform density and are separated by stably stratified interfaces. To compare our simulations to the predictions of Linden & Shirtcliffe (1978) we first must consider that the essential component of their model is the assumption that layer interfaces are composed of a diffusive core with unstable boundary layers above and below. If we detect a diffusive core in our simulations, their model may apply. To determine this, we measure the horizontally averaged, depth dependent thermal and compositional Nusselt numbers defined as

$$\mathrm{Nu}_T = 1 + \frac{\overline{wT}}{1 - \frac{d\overline{T}}{dz}} \quad , \quad \mathrm{Nu}_\mu = 1 + \frac{\overline{w\mu}}{\tau\left(R_0^{-1} - \frac{d\overline{\mu}}{dz}\right)} \, , \tag{4.11}$$

where the overbars denote horizontal averages. From Figure 4.5a, we see that Nu_T and Nu_μ are both close to 1 in the interfaces, meaning that transport of temperature and chemical composition through them is almost entirely diffusive. Interestingly, however, looking at the horizontally averaged rms velocity, $u_{\mathrm{rms}} = \overline{u}^2 + \overline{v}^2 + \overline{w}^2$, we see that the interface is not entirely quiescent, but instead has a non-zero u_{rms}. This may be due to gravity waves in the interface, which have some kinetic energy but do not induce any net transport of temperature or chemical species.

Looking at the mean temperature and compositional profiles in Figure 4.5b, we see that the region that is fully mixed in temperature is smaller than that for chemical composition, owing to the fact that temperature diffuses much more quickly. This disparity is, in fact, what drives the layered convection, because the presence of an unstable temperature gradient in regions that are fully mixed in chemical composition leads to a small but crucial inversion in the density profile (Carpenter et al., 2012). The size of this unstable boundary is determined by the gradients of temperature and chemical composition in the diffusive interfacial core. Linden & Shirtcliffe (1978) predict that the ratio of the these gradients is given by Equation (4.12). For the simulation presented here the predicted value is

$$\frac{\partial\mu/\partial z}{\partial T/\partial z} = (0.03)^{-1/2} \approx 5.8 \, . \tag{4.12}$$

However, from Figure 4.5c we find that $\frac{\partial\mu/\partial z}{\partial T/\partial z} \approx 16.5$. This discrepancy with prediction suggests that there could be a similar discrepancy in the inverse flux ratio, $\gamma_{\rm tot}^{-1}$.

To study this, we now discuss our quantitative results from measurements of $\gamma_{\rm tot}^{-1}$ in all of our proto-layered simulations. As in Section 4.3, we consider simulations which have been initialized with one layer, and have various values of Pr, τ and R_0^{-1} (detailed in Table 4.1). Figure 4.6a shows $\gamma_{\rm tot}^{-1}$ as a function of the reduced inverse density ratio, r, (see Equation 1.10) for $\mathrm{Pr} = \tau = 0.01$, 0.03, 0.1, and 0.3. Also included are data points from spontaneously formed layers in simulations of ODDC run by Mirouh et al. (2012), which we reanalyzed to measure $\gamma_{\rm tot}^{-1}$ in the 1 layered phase. Simulation data (not shown here) demonstrates that layers that form spontaneously have identical steady states to proto-layers that are imposed in the spontaneous layer formation parameter regime. For each set of Pr and τ, $\gamma_{\rm tot}^{-1}$ initially decreases sharply with r, and then asymptote to a constant for larger values of r. The shape of these curves is reminiscent of Figure 7 from Turner (1965) which shows a similar plot of (the equivalent of) $\gamma_{\rm tot}^{-1}$ as a function of R_0^{-1} for geophysically relevant values of Pr and τ ($\mathrm{Pr} = 7$ and $\tau = 0.015$). The model of Linden & Shirtcliffe (1978) discussed in Section 4.1 only applies to this high density ratio regime where $\gamma_{\rm tot}^{-1}$ is independent of r, and predicts that $\gamma_{\rm tot}^{-1} = \tau^{1/2}$. In order to test its applicability to the more astrophysically relevant low Pr regime, we now focus on the value of $\gamma_{\rm tot}^{-1}$ in the plateau region. Our results are shown in Figure 4.6b. We see that our measurements are inconsistent with the model of Linden & Shirtcliffe (1978). Our measurements fit more closely with the $\gamma_{\rm tot}^{-1} = \tau^{1/4}$ line (shown for reference). Why this is the case remains to be determined, but some preliminary ideas are discussed below.

n_L	Pr, τ	R_0^{-1}	r	A	Layers	$\mathrm{Nu}_T - 1$	$\mathrm{Nu}_\mu - 1$	$\gamma_{\mathrm{tot}}^{-1}$
3	0.03	7.87	0.42	500	no	NA	NA	NA
3	0.03	7.87	0.42	100	no	NA	NA	NA
3	0.03	7.87	0.42	80	no	NA	NA	NA
3	0.03	4.00	0.19	65	yes	2.2 ± 0.23	9.0 ± 0.75	0.39 ± 0.028
2	0.3	1.5	0.43	100	no	NA	NA	NA
2	0.3	2.0	0.86	100	no	NA	NA	NA
2	0.3	7.87	5.9	100	no	NA	NA	NA
2	0.03	3.0	0.12	100	yes	5.4 ± 0.23	32.1 ± 2.0	0.47 ± 0.029
2	0.03	7.87	0.42	100	yes	1.38 ± 0.061	3.0 ± 0.054	0.40 ± 0.018
2	0.03	7.87	0.42	200	yes	1.52 ± 0.064	3.4 ± 0.060	0.41 ± 0.024
2	0.03	10.0	0.56	100	no	NA	NA	NA
1	0.3	1.5	0.43	49	yes	7.5 ± 2.1	11.1 ± 3.2	0.73 ± 0.034
1	0.3	2.0	0.86	57	yes	2.0 ± 0.40	2.4 ± 0.32	0.69 ± 0.058
1	0.3	3.0	1.7	57	yes	0.48 ± 0.029	0.74 ± 0.039	0.83 ± 0.028
1	0.3	7.87	5.9	150	no	NA	NA	NA
1	0.1	2.25	0.28	61	yes	3.8 ± 0.74	7.5 ± 1.6	0.56 ± 0.056
1	0.1	3.25	0.5	76	yes	1.7 ± 0.099	2.4 ± 0.11	0.51 ± 0.042
1	0.1	4.25	0.72	92	yes	1.0 ± 0.19	1.39 ± 0.075	0.51 ± 0.076
1	0.03	2.0	0.56	73	yes	6.8 ± 0.94	51.7 ± 14.1	0.61 ± 0.037
1	0.03	3.0	0.56	73	yes	2.8 ± 0.2	9.6 ± 1.0	0.42 ± 0.059
1	0.03	7.87	0.56	150	yes	0.77 ± 0.054	1.2 ± 0.045	0.37 ± 0.033
1	0.03	10.0	0.56	184	yes	0.57 ± 0.019	0.88 ± 0.01	0.38 ± 0.012
1	0.01	3.0	0.56	73	yes	2.9 ± 0.30	26.7 ± 4.3	0.44 ± 0.042
1	0.01	7.87	0.56	150	yes	0.81 ± 0.029	2.0 ± 0.12	0.28 ± 0.021
1	0.01	10.0	0.56	184	yes	0.63 ± 0.028	1.3 ± 0.081	0.26 ± 0.024

Table 4.1: A summary of the characteristics of each of our proto-layered simulations

4.5 Discussion & conclusion

Here we have analyzed the subcritical branch of solutions for layered diffusive convection in the astrophysical parameter regime. The results presented here are pertinent for any astrophysical systems where parameters are not conducive to spontaneous layer formation in ODDC, namely when $R_0^{-1} > R_L^{-1}$. For example, subcritical layering may be important near the cores of giant planets where large compositional gradients are likely to exist. They could also be pertinent to semi-convective regions in intermediate-mass stars that are far from the convective core.

Past studies of double diffusive layering in astrophysics have assumed that subcritical layers are always excited, and their associated flux laws are the same as those developed for double diffusive layering in geophysical fluids. To test these assumptions, we have run numerical simulations to determine the conditions under which finite amplitude perturbations excite the subcritical instability at astrophysical parameters. While we do not have enough data to test the flux law in Equation 4.2 from Turner (1965), we have run a suite of simulations to test the predictions of Linden & Shirtcliffe (1978), namely Equations (4.3)-(4.5). The primary result of this work is that our data do not fit the prediction that $\gamma_{\text{tot}}^{-1} = \tau^{1/2}$. Instead our results seem to suggest that $\gamma_{\text{tot}}^{-1} \propto \tau^{1/4}$. Why this is the case is not certain, but there are a few interesting possibilities.

One possible explanation is that, at astrophysical parameters, the simulations studied here are still unstable to non-layered ODDC (of the kind described in Chapter 2) meaning that their inverse density ratios satisfy the conditions

$$R_L^{-1} < R_0^{-1} < R_c^{-1} \,. \tag{4.13}$$

From the ratio of the interfacial gradients of temperature and chemical composition shown in Figure 4.5c we estimate the inverse density ratio in the interface to be $R_I^{-1} \approx 13$. For $\mathrm{Pr} = \tau = 0.03$ however, $R_c^{-1} \approx 17.2$ meaning that even the interface is theoretically unstable to ODDC (though it is unclear if the interface is thick enough for the primary instability to actually grow).

This is in contrast to the geophysical systems studied by Linden & Shirtcliffe (1978) where $R_0^{-1} > R_c^{-1}$ (as mentioned earlier $R_c^{-1} \approx 1.14$ for systems with $\mathrm{Pr} = 7$ and $\tau = 0.01$). The fact that we are taking measurements in regions of parameter space with different dynamics, could be the cause $\gamma_{\mathrm{tot}}^{-1}$ to have a different relationship with τ. However, we believe that for astrophysically relevant systems, $R_L^{-1} < R_0^{-1} < R_c^{1}$ is the correct parameter regime to investigate, since cases with $R_0^{-1} > R_c^{-1}$ would require an unphysically large stabilizing compositional gradient to exist.

Another explanation is that because Pr is so low there could be turbulent mixing of chemical composition in the boundary layer between the diffusive interfacial core and the mixed layer. Consequently, the relevant diffusivity to consider when calculating $\gamma_{\mathrm{tot}}^{-1} = \left(\frac{\kappa_\mu}{\kappa_T}\right)^{1/2}$ may in fact be a turbulent diffusivity of chemical composition rather than the molecular one. This possibility deserves further investigations that will be the subject of future work.

An important observational implication of this work is that the relation, $\gamma_{\mathrm{tot}}^{-1} \propto \tau^{1/4}$, results in a higher compositional flux (relative to the temperature flux) than predicted by Linden & Shirtcliffe (1978). This could mean that, for example, the cores of giant planets may erode faster than originally thought. Indeed, as shown by Guillot et al. (2004) one can use $\gamma_{\mathrm{tot}}^{-1}$ (which they call χ) to estimate the evolution of the core mass as a function of time for Jupiter and Saturn. They use the $\gamma_{\mathrm{tot}}^{-1} = \tau^{1/2}$ model with $\tau = 0.01$ to estimate $\chi = 0.1$, and show that about 20

$M_\oplus$ of Jupiter's core can be eroded this way. However, if instead the $\gamma_{\mathrm{tot}}^{-1} = \tau^{1/4}$ model is used, that would mean $\chi \approx 0.3$. Since the erosion rate is proportional to χ that means the amount of material removed from the core could be 3 times higher than previously thought. Consequently, at present day Jupiter may not have a core at all unless the original core mass was greater than $\simeq 60 M_\oplus$.

An important caveat to consider in this discussion is that in order to fully understand this type of layering we must also identify possible excitation mechanisms for the subcritical instability. Possible triggers could be the presence of shear flows (Radko, 2016) or a bottom heating mechanism similar to that studied in lakes and oceans on earth. Given that we observe subcritical layering on earth through a number of mechanisms, suggests that the formation of layers in astrophysics when $R_0^{-1} > R_L^{-1}$ is likely to occur in at least *some* circumstances. However, as we have shown here, fairly specific conditions must be satisfied for a finite amplitude perturbation to be able to excite persistent layers, and it would therefore be hasty to assume that subcritical layering is *always* excited.

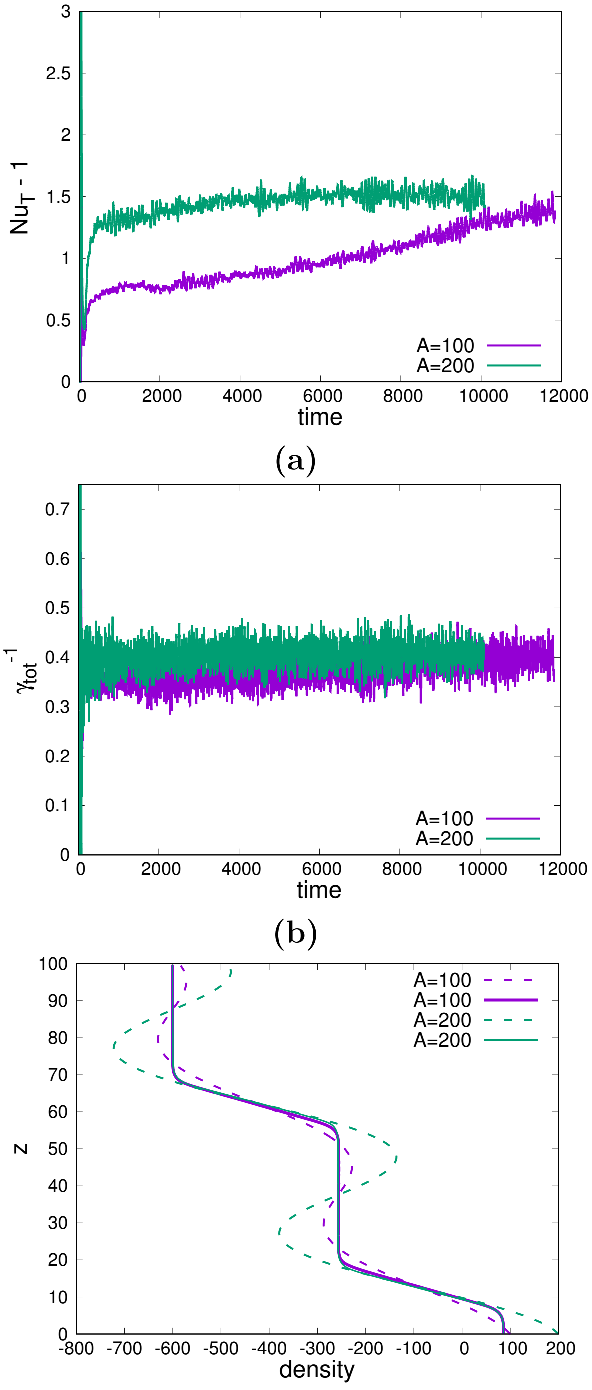

(a)

(b)

(c)

Figure 4.2: Time series of (a) turbulent temperature flux and (b) γ_{tot}^{-1} for proto-layerd simulations with $A = 100$ and $A = 200$. In both cases $\text{Pr} = \tau = 0.03$ and $R_0^{-1} = 7.87$. Both simulations were initialized with 2 proto-layers. (c) Initial and equilibrium density profiles for both simulations.

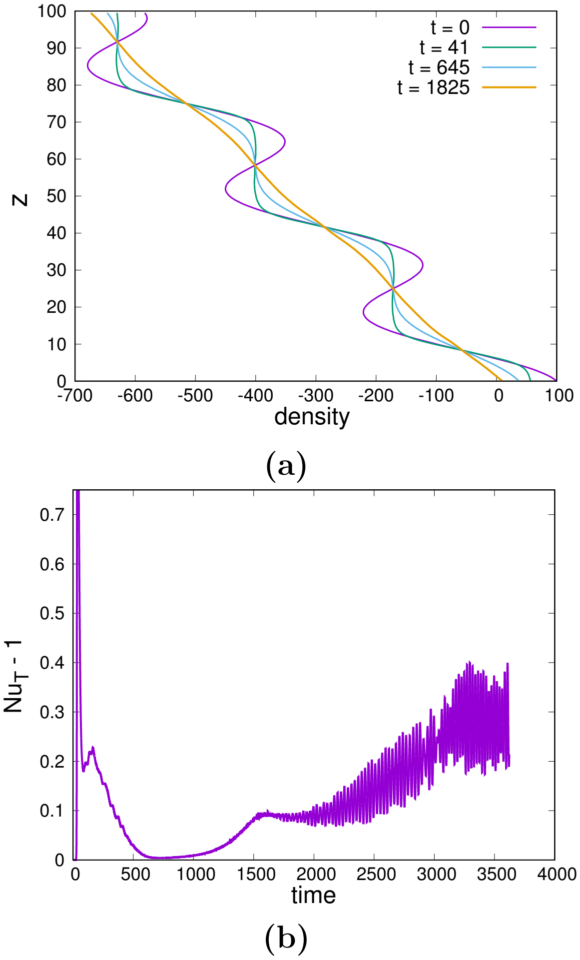

Figure 4.3: (a) Density profiles at various times and (b) time series of turbulent temperature flux for proto-layered simulation with $\mathrm{Pr} = \tau = 0.03$ and $R_0^{-1} = 7.87$. The simulation was initialized with three layers, and with $A = 100$.

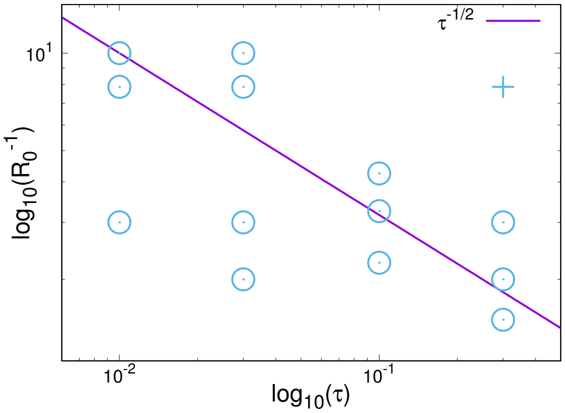

Figure 4.4: The locations of various 1 layered simulations in the parameter space of R_0^{-1} and τ. Circles indicate simulations that maintain a layered configuration for the duration of the simulation, while the cross marker indicates a simulation where a convective layer was not maintained. The line $R_0 = \tau^{-1/2}$ is plotted as well. Theoretically, layers should not be able to persist above this line, however some of ours do.

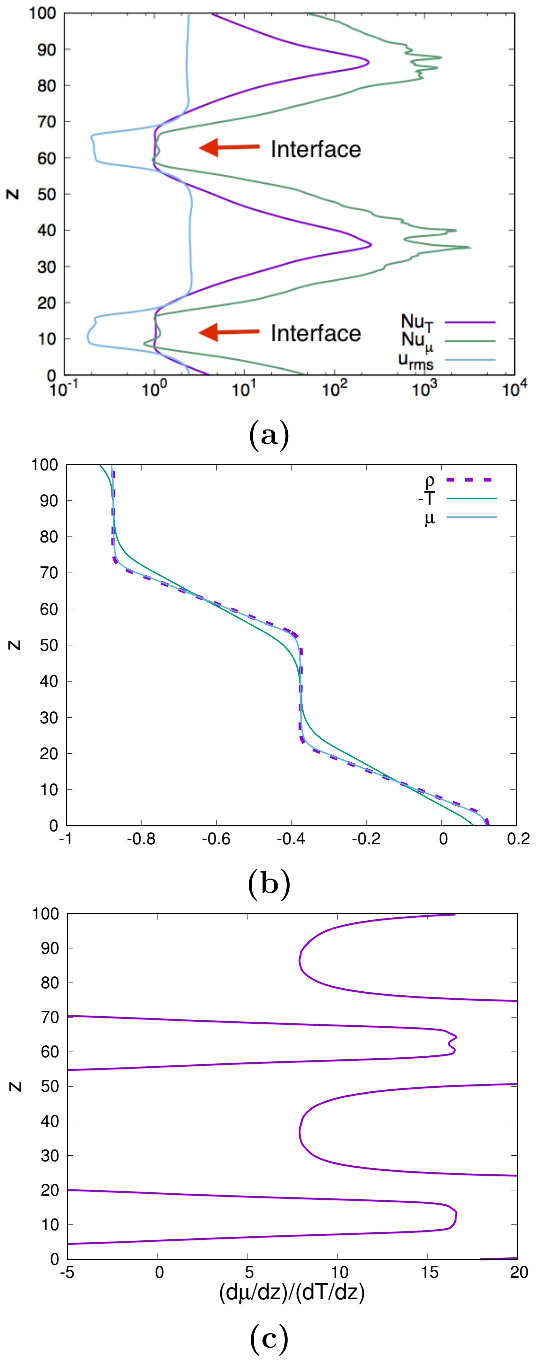

Figure 4.5: (a) the horizontally averaged vertical profiles of Nu_T, Nu_μ, and u_{rms} (rms velocity). Arrows indicate the locations of the interfaces. Both Nu_T and Nu_μ are close to 1 in the interfaces indicating that they are almost completely diffusive. (b) Vertical profiles of temperature, chemical composition and density. Temperature is normalized by L_z, chemical composition by $R_0^{-1}L_z$, and density by $(1 - R_0^{-1})L_z$. (c) Horizontally averaged ratio $\frac{\partial\mu/\partial z}{\partial T/\partial z} \approx 16.5$ as a function of deption.

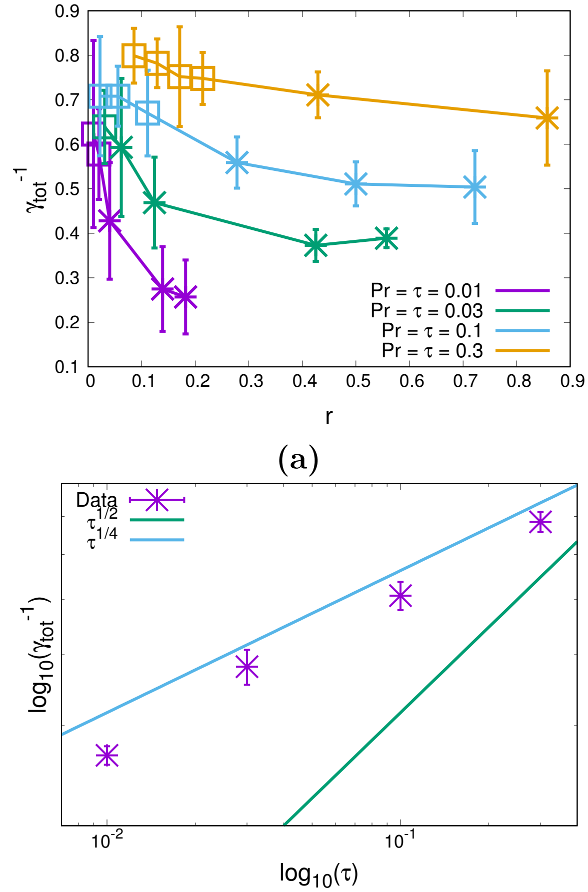

(a)

(b)

Figure 4.6: (a) γ_{tot}^{-1} as a function of r for various astrophysically relevant values of Pr and τ. Stars indicate proto-layered simulations and squares represent data taken from spontaneously formed layers in simulations of ODDC. (b) γ_{tot}^{-1} as a function of τ. Also shown is the line $\gamma_{\text{tot}}^{-1} = \tau^{1/2}$ (predicted value for geophysical systems from Linden & Shirtcliffe (1978)), and the line $\gamma_{\text{tot}}^{-1} = \tau^{1/4}$ (for reference).

Chapter 5

Conclusion

The work presented here comprises a broad study of the dynamics of both layered and non-layered double diffusive convection in the astrophysical parameter regime. Chapters 2 and 3 both focused on numerical simulations started from random noise to study the dynamics that evolve naturally from the linear instability that is ODDC. This method has revealed a myriad of different behaviors and a complex multi-dimensional parameter space (a sample of which is shown in Figure 5.1).

The in-depth study of non-layered oscillatory double diffusive convection (ODDC) from Chapter 2 completes a comprehensive study of the parameter space of ODDC begun by Rosenblum et al. (2011), Mirouh et al. (2012) and Wood et al. (2013). In the non-layered parameter regime there is far less regularity in long term behavior than in the layered regime. The interplay of large scale gravity wave modes is highly non-linear, and the large scale dynamics are more difficult to predict. In one simulation intermittent large scale shear was generated, but this phenomenon could not be reproduced in simulations at different parameters. Also, it remains to be determined whether one can create a theory from first principles describing quasi-steady levels of thermal and compositional flux. Studying non-layered sys-

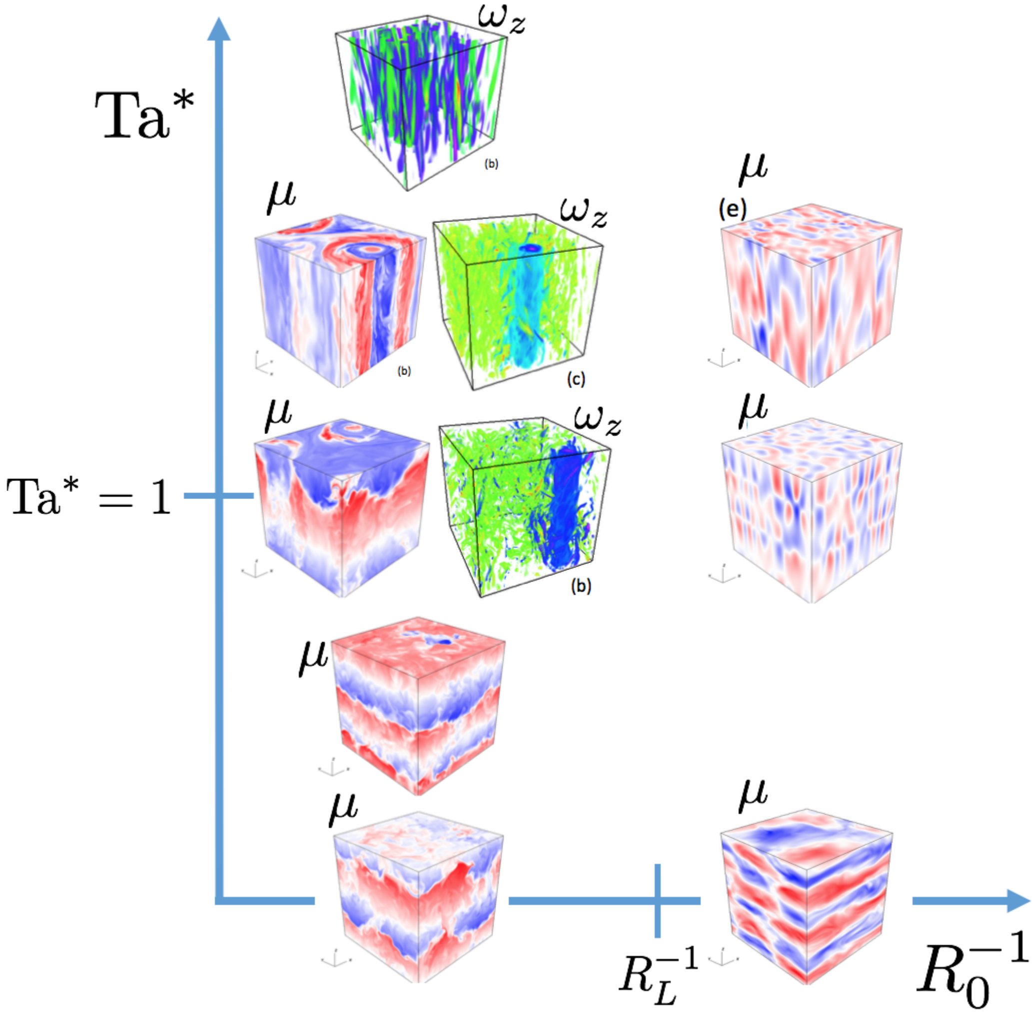

Figure 5.1: Snapshots of the chemical composition and vertical vorticity fields (labeled μ and ω, respectively) for simulations with various values of R_0^{-1} and Ta^*. For each, $\mathrm{Pr} = \tau = 0.1$ and $\theta = 0$.

tems is further complicated by the fact that it is a numerically difficult parameter space to explore, due to the wide range of time scales present: for instance, at high R_0^{-1} the gravity wave oscillation time scale is very fast while the growth of the primary instability is very slow. This problem surfaces in the rotating systems studied in Chapter 3 as well, particularly in rapidly rotating simulations.

Chapter 3 is a first step into more complex models of ODDC that include more sophisticated physical effects (in this case global rotation).With rotating

ODDC we have had success determining analytically when convective overturn is expected to occur in layers. We also established a criterion to indicate when ODDC is rotationally dominated ($\mathrm{Ta}^* > 1$). This was a broad survey of the rotating parameter space both in rotation rate and in the inclination of the direction of rotation with respect to the direction of gravity. Consequently, we observed a wide range of behaviors including both small and large scale vortices. These features deserve further study, as their presence in simulations is usually associated with the suppression of layer formation (at parameters conducive to layer formation in non-rotating ODDC).

The approach of Chapters 2 and 3 is somewhat different from the way double diffusive convection has historically been studied in the astrophysical regime. Indeed, double diffusive systems have typically been assumed to exist in a layered configuration, so studying properties of both layered and non-layered systems implicitly challenges this assumption. In that same spirit, Chapter 4 also challenges widely held notions about the applicability of geophysically derived flux laws to astrophysical systems.

As mentioned in Chapters 2 and 4, flux laws commonly quoted in the astrophysical literature are originally derived from geophysical studies. This was initially a reasonable thing to do because in situ measurements and laboratory experiments of the dynamical properties of double diffusive fluids at astrophysical parameters is functionally impossible. As we have discussed previously, however, this comparison is imperfect, and may lead to incorrect results. The work presented here (along with prior work by Rosenblum et al., 2011; Mirouh et al., 2012; Wood et al., 2013) is an attempt to develop an astrophysical numerical equivalent to the earlier laboratory experiments in the geophysical regime by the likes of Turner (1965) and Shirtcliffe (1973). In that sense, an underlying purpose of each of the studies presented here is to demonstrate the versatility and usefulness of direct numerical simulations for studying the dynamics of double diffusive convection.

The worked presented here reveals several possible avenues of future research. First of all, the study of rotating ODDC in Chapter 3 was a preliminary survey of parameter space, and issues such as the precise conditions for the formation of large scale vortices and the effects of inclination in the high Ta^* regime deserve further study. It would also be interesting to apply proto-layered initial conditions to a rotating system to determine what impact rotation has on the persistence of subcritical layering. Also, one question left unanswered in Chapter 4 with regard to subcritical layering is whether or not the temperature (and chemical composition) flux predictions from Turner (1965) still hold in the astrophysical parameter regime (namely $T \propto (\Delta T)^{4/3}$). Finally, studying the effects of other physical mechanisms such as large scale shear and magnetic fields on the dynamics of double diffusive convection is fertile ground for future research.

Appendix: Minimum mode amplitudes for layered convection

In rotating systems density perturbations must grow to a higher amplitude in order for layered convection to occur, compared to non-rotating ones. This can be understood better by considering how convective plumes form at the edges of the diffusive boundaries in layered convection. In order for a hot plume at the bottom of a layer to rise it must displace the fluid above it. Because the interfaces act as flexible but more-or-less impenetrable boundaries, fluid that is moving upward because of the rising plume must be deflected by the top boundary and displaced horizontally. Rotation resists motion involving gradients of velocity in the direction of the rotation axis. In order to overcome this resistance, and therefore for convection to take place in the layer, a more strongly positive density gradient must be present between the interfaces.

We make quantitative estimates of this effect on layered convection in ODDC through adaptation of a theory related to rotating Rayleigh-Bénard convection (Chandrasekhar, 1961). Assuming free boundary conditions, the critical Rayleigh number, Ra_c, for rotating Rayleigh-Bénard convection is the following function of Ta^*:

$$\mathrm{Ra}_c(\mathrm{Ta}^*) = 3\pi^4 \left(\frac{H^4 \mathrm{Ta}^*}{2\mathrm{Pr}^2 \pi^4} \right)^{\frac{2}{3}} + \frac{27\pi^4}{4} \,, \tag{.1}$$

where H is the layer height. In our non-dimensionalization the critical density gradient for a convective layer, $\left|\frac{\partial \rho}{\partial z}\right|_c$, can be written in terms of Ra_c as

$$\left|\frac{\partial \rho}{\partial z}\right|_c = \frac{\mathrm{Ra}_c}{H^4} \,. \tag{.2}$$

Then by considering a density profile defined as

$$\rho = (1 - R_0^{-1})z + 2A_n \sin\left(k_n z\right) , \tag{.3}$$

where A_n is the amplitude of the perturbation from a single layering mode with vertical wavenumber k_n, we provide a second definition for the critical density gradient

$$\left|\frac{\partial \rho}{\partial z}\right|_c = \max\left(\frac{\partial \rho}{\partial z}\right) = 1 - R_0^{-1} + 2A_n k_n \,. \tag{.4}$$

From equations (.1) through (.4) we can then generate an expression for $|A_n|$ in terms of Ta^*, R_0^{-1}, H, and k_n, and thus an estimate for the critical layering mode amplitude for the onset of layered convection,

$$|A_n| = \left| \frac{\frac{\mathrm{Ra}_c}{H^4} + \left(R_0^{-1} - 1\right)}{2k_n} \right| = \left| \frac{\frac{3\pi^4}{H^4}\left(\frac{H^4 \mathrm{Ta}^*}{2\mathrm{Pr}^2\pi^4}\right)^{\frac{2}{3}} + \frac{27\pi^4}{4H^4} + \left(R_0^{-1} - 1\right)}{2k_n} \right| . \qquad (.5)$$

This formula recovers Equation (29) of Rosenblum et al. (2011) in the non-rotating limit, as long as the term $27\pi^4/4H^4$ can be neglected (which is always true for physically realizable layer heights, that typically have $H > 30$).

Bibliography

Baines, P., & Gill, A. 1969, J. Fluid Mech., 37

Blies, P., Kupka, F., Zaussinger, F., & Hollerbach, R. 2014, ArXiv e-prints

Carpenter, J. R., Sommer, T., & WÃijest, A. 2012, Journal of Fluid Mechanics, 711, 411

Carpenter, J. R., & Timmermans, M.-L. 2014, Journal of Physical Oceanography, 44, 289

Chandrasekhar, S. 1961, Hydrodynamic and hydromagnetic stability (International Series of Monographs on Physics, Oxford: Clarendon)

Degens, E. T., von Herzen, R. P., Wong, H.-K., Deuser, W. G., & Jannasch, H. W. 1973, Geologische Rundschau, 62, 245

French, M., Becker, A., Lorenzen, W., Nettelmann, N., Bethkenhagen, M., Wicht, J., & Redmer, R. 2012, ApJS, 202, 5

Fuller, J. 2014, Icarus, 242, 283

Garaud, P., & Brummell, N. 2015, ArXiv e-prints

Guervilly, C., Hughes, D. W., & Jones, C. A. 2014, Journal of Fluid Mechanics, 758, 407

Guillot, T., Stevenson, D. J., Hubbard, W. B., & Saumon, D. 2004, The interior of Jupiter, 35–57

Hubbard, W. B., Podolak, M., & Stevenson, D. J. 1995, in Neptune and Triton, ed. D. P. Cruikshank, M. S. Matthews, & A. M. Schumann, 109–138

Huppert, H. E., & Moore, D. R. 1976, Journal of Fluid Mechanics, 78, 821

Julien, K., Legg, S., McWilliams, J., & Werne, J. 1996, Journal of Fluid Mechanics, 322, 243

Julien, K., Rubio, A. M., Grooms, I., & Knobloch, E. 2012, Geophysical and Astrophysical Fluid Dynamics, 106, 392

Kato, S. 1966, PASJ, 18, 374

Langer, N., El Eid, M. F., & Fricke, K. J. 1985, A&A, 145, 179

Langer, N., Fricke, K. J., & Sugimoto, D. 1983, A&A, 126, 207

Leconte, J., & Chabrier, G. 2012, A&A, 540, A20

Linden, P. F., & Shirtcliffe, T. G. L. 1978, Journal of Fluid Mechanics, 87, 417

Malkus, W. V. R. 1954, Proceedings of the Royal Society of London Series A, 225, 196

Merryfield, W. J. 1995, ApJ, 444, 318

Mirouh, G. M., Garaud, P., Stellmach, S., Traxler, A. L., & Wood, T. S. 2012, ApJ, 750, 61

Moll, R., Garaud, P., & Stellmach, S. 2016, ApJ, 823, 33

Moore, K., & Garaud, P. 2015, ArXiv e-prints

Nettelmann, N., Fortney, J. J., Moore, K., & Mankovich, C. 2015, MNRAS, 447, 3422

Newell, T. A. 1984, Journal of Fluid Mechanics, 149, 385

Newman, F. C. 1976, Journal of Physical Oceanography, 6, 157

Noguchi, T., & Niino, H. 2010, Journal of Fluid Mechanics, 651, 443

Perkin, R. G., & Lewis, E. L. 1984, Journal of Physical Oceanography, 14, 1315

Proctor, M. R. E. 1981, Journal of Fluid Mechanics, 105, 507

Radko, T. 2003, J. Fluid Mech., 497, 365

Redmer, R., Mattsson, T. R., Nettelmann, N., & French, M. 2011, Icarus, 211, 798

Rosenblum, E., Garaud, P., Traxler, A., & Stellmach, S. 2011, ApJ, 731, 66

Rossby, H. T. 1969, Journal of Fluid Mechanics, 36, 309

Schmalzl, J., Breuer, M., & Hansen, U. 2004, EPL (Europhysics Letters), 67, 390

Schwarzschild, M., & Härm, R. 1958, ApJ, 128, 348

Shirtcliffe, T. G. L. 1973, Journal of Fluid Mechanics, 57, 27

Spiegel, E. A. 1969, Comments on Astrophysics and Space Physics, 1, 57

Spiegel, E. A., & Veronis, G. 1960, ApJ, 131, 442

Spruit, H. C. 1992, A&A, 253, 131

—. 2013, A&A, 552, A76

Stellmach, S., Traxler, A., Garaud, P., Brummell, N., & Radko, T. 2011, ArXiv e-prints

Stevenson, D. J. 1982, Planet. Space Sci., 30, 755

Stevenson, D. J., & Salpeter, E. E. 1977, ApJS, 35, 239

Timmermans, M.-L., Garrett, C., & Carmack, E. 2003, Deep Sea Research Part I: Oceanographic Research, 50, 1305

Toole, J., et al. 2006, EOS Transactions, 87, 434

Traxler, A., Stellmach, S., Garaud, P., Radko, T., & Brummell, N. 2011, ArXiv e-prints

Turner, J. 1965, International Journal of Heat and Mass Transfer, 8, 759

Turner, J. S. 1968, Journal of Fluid Mechanics, 33, 183

van der Poel, E. P., Stevens, R. J. A. M., & Lohse, D. 2013, Journal of Fluid Mechanics, 736, 177

Walin, G. 1964, Tellus, 16, 389

Wood, T. S., Garaud, P., & Stellmach, S. 2013, ApJ, 768, 157

Zaussinger, F., & Spruit, H. C. 2013, A&A, 554, A119